

広島大学学位請求論文

**Study on the nonradiative decay and *trans*
→ *cis* photoisomerization of cinnamates by
supersonic jet / laser spectroscopy and
quantum chemical calculation**

超音速ジェットレーザー分光と量子化学
計算による桂皮酸誘導体の無輻射緩和と
trans → *cis* 光異性化の研究

2021年

広島大学大学院理学研究科
化学専攻

木下 真之介

目 次

1. 主論文

Study on the nonradiative decay and *trans* → *cis* photoisomerization of cinnamates by supersonic jet / laser spectroscopy and quantum chemical calculation

(超音速ジェットレーザー分光と量子化学計算による桂皮酸誘導体の無輻射緩和と *trans* → *cis* 光異性化の研究)

木下 真之介

2. 公表論文

(1) Substitution effect on the nonradiative decay and *trans* → *cis* photoisomerization route: a guideline to develop efficient cinnamate based sunscreens

Shin-nosuke Kinoshita, Yu Harabuchi, Yoshiya Inokuchi, Satoshi Maeda, Masahiro Ehara, Kaoru Yamazaki and Takayuki Ebata

Phys. Chem. Chem. Phys., 2021, **23**, 834-845.

Front cover picture, 2021 PCCP HOT Articles

(2) The direct observation of the doorway $^1n\pi^*$ state of methylcinnamate and hydrogen-bonding effects on the photochemistry of cinnamate-based sunscreens

Shin-nosuke Kinoshita, Yoshiya Inokuchi, Yuuki Onitsuka, Hiroshi Kohguchi, Nobuyuki Akai, Takafumi Shiraogawa, Masahiro Ehara, Kaoru Yamazaki, Yu Harabuchi, Satoshi Maeda and Takayuki Ebata

Phys. Chem. Chem. Phys., 2019, **21**, 19755-19763.

Back cover picture, 2019 PCCP HOT Articles

(3) Different photoisomerization routes found in the structural isomers of hydroxy methylcinnamate

Shin-nosuke Kinoshita, Yasunori Miyazaki, Masataka Sumida, Yuuki Onitsuka, Hiroshi Kohguchi, Yoshiya Inokuchi, Nobuyuki Akai, Takafumi Shiraogawa, Masahiro Ehara, Kaoru Yamazaki, Yu Harabuchi, Satoshi Maeda, Tetsuya

Taketsugu and Takayuki Ebata

Phys. Chem. Chem. Phys., 2018, **20**, 17583-17598.

Back cover picture

3. 参考論文

(1) **Electronic States and Nonradiative Decay of Cold Gas-Phase Cinnamic Acid Derivatives Studied by Laser Spectroscopy with Laser Ablation Technique**

Yuji Iida, Shin-nosuke Kinoshita, Seiya Kenjo, Satoru Muramatsu, Yoshiya Inokuchi, Chaoyuan Zhu, and Takayuki Ebata

J. Phys. Chem. A **2020**, *124*, 5580-5589.

(2) **Electronic State and Photophysics of 2-Ethylhexyl-4-methoxy cinnamate as UV-B Sunscreen under Jet-Cooled Condition**

Satoru Muramatsu, Shingo Nakayama, Shin-nosuke Kinoshita, Yuuki Onitsuka, Hiroshi Kohguchi, Yoshiya Inokuchi, Chaoyuan Zhu, and Takayuki Ebata

J. Phys. Chem. A **2020**, *124*, 1272-1278.

(3) **Laser spectroscopic study on sinapic acid and its hydrated complex in a cold gas phase molecular beam**

Seiya Kenjo, Yuji Iida, Nobumasa Chaki, Shin-nosuke Kinoshita, Yoshiya Inokuchi, Kaoru Yamazaki, Takayuki Ebata

Chemical Physics 515 (2018) 381-386.

(4) **Multistep Intersystem Crossing Pathways in Cinnamate-Based UV-B Sunscreens**

Kaoru Yamazaki, Yasunori Miyazaki, Yu Harabuchi, Tetsuya Taketsugu, Satoshi Maeda, Yoshiya Inokuchi, Shin-nosuke Kinoshita, Masataka Sumida, Yuuki Onitsuka, Hiroshi Kohguchi, Masahiro Ehara, and Takayuki Ebata

J. Phys. Chem. Lett. **2016**, *7*, 4001-4007.

主論文

Acknowledgements

I would like to express my thanks to all the people who supported my research and daily life. Especially, through discussions with my supervisors, Prof. Takayuki Ebata and Prof. Yoshiya Inokuchi, I was able to learn experimental techniques and how to deal with issues, and gain important advises, interesting ideas and a motivation for my research.

I would also like to thank co-workers who are listed below. Their experimental and theoretical support made my research more valuable. Especially, Dr. Kaoru Yamazaki politely taught me how to analyze the results of quantum chemical calculation.

Finally, I would like to thank my parents for financially supporting my daily life.

- Cold matrix-isolation FTIR spectroscopy
(Tokyo Univ. of A & T) Dr. Nobuyuki Akai
- UV-DUV pump-probe spectroscopy
(Hiroshima Univ.) Dr. Hiroshi Kohguchi
- Symmetry Adapted Cluster/Configuration Interaction calculation
(IMS) Prof. Masahiro Ehara
- Artificial Force Induced Reaction method/
Time-Dependent Density-Functional Theory calculation
(Hokkaido Univ.) Prof. Satoshi Maeda and Dr. Yu Harabuchi
(RIKEN) Dr. Kaoru Yamazaki

Shin-nosuke Kinoshita

Contents

Chapter 1

General introduction	1
1-1 Use of cinnamates as a sunscreen	1
1-2 Studies on the photochemistry of cinnamates.....	7
1-3 Purpose and outline of this study.....	11
References.....	13

Chapter 2

Experimental and Theoretical methods	16
2-1 Supersonic jet.....	16
2-2 Measurement of electronic spectra under jet-cooled condition.....	18
2-3 Lifetime measurement of excited state	20
2-4 Cold matrix-isolation FTIR spectroscopy	22
2-5 Sample preparation.....	23
2-6 Systematic search for the NRD/photoisomerization route.....	25
2-7 Calculation of spin-orbit coupling constant.....	29
2-8 Rate constant of radiative decay	30
References.....	31

Chapter 3

Electronic states and nonradiative decay involving <i>trans</i> → <i>cis</i> photoisomerization of methylcinnamate	34
3-1 Electronic spectra of jet-cooled methylcinnamate.....	34
3-2 Assignment of conformers and electronic transitions	38
3-3 Lifetime measurement and nonradiative decay process	43
3-4 Photoproduct analysis upon UV irradiation.....	49
3-5 Systematic search for the dominant NRD/photoisomerization route	51
3-6 C=C bond twisting route on the $^1\pi\pi^*$ state.....	61
3-7 Conclusion	63
References.....	64

Chapter 4

Substitution and its position effects on the photoisomerization of cinnamates	65
4-1 Electronic spectra of cinnamates.....	65
4-2 Lifetime measurement and nonradiative decay process	73
4-2-1 <i>p</i> -HMC and <i>p</i> -MMC.....	73
4-2-2 <i>m</i> -HMC and <i>o</i> -HMC	78
4-3 Photoproduct analysis upon UV irradiation.....	85
4-4 Systematic search for the NRD/photoisomerization route.....	95
4-4-1 <i>p</i> -HMC and <i>p</i> -MMC.....	95
4-4-2 <i>m</i> -HMC and <i>o</i> -HMC	97
4-5 Mechanism of the NRD/photoisomerization route modulation for substituted cinnamates	106
4-5-1 <i>p</i> -HMC and <i>p</i> -MMC.....	106

4-5-2 <i>m</i> -HMC and <i>o</i> -HMC	120
4-6 Conclusion	124
References.....	126

Chapter 5

Hydrogen-bonding effect on electronic states and nonradiative decay process of cinnamates

128

5-1 Electronic spectra and assignment of the electronic states.....	128
5-2 H-bonding effect on the NRD process	133
5-3 Absorption and fluorescence spectra	138
5-4 Conclusion	141
References.....	142

Chapter 6

Conclusion of this thesis.....

143

Chapter 1

General introduction

1-1 Use of cinnamates as a sunscreen

Ultraviolet (UV) light from the sun is divided into three region of the energy (wavelength); UV-A (400-315 nm), UV-B (315-280 nm) and UV-C (280-100 nm).¹ The red curve shown in Figure 1 is the solar spectrum through the atmosphere.^{2,3} The amount of UV-C leaching the earth's surface is negligible, because the UV-C is absorbed in ozone layer.⁴ For humans, the UV light is necessary to synthesize the vitamin D.⁵ The underexpose of UV causes a lack of the vitamin D, leading to some skeletal diseases.^{6,7} On the other hand, the UV sometimes damages the human skin, therefore its overexpose may cause a skin cancer.⁷⁻¹²

The human body has a mechanism to protect the skin from UV damage.¹³ Skin pigmentation is one of the primary photoprotective mechanism for humans. The pigment absorbs the harmful UV light before the light reaches and interacts with DNA in the skin. The pigment mainly consists of melanin. Eumelanin is the primary melanin and synthesized in the cell called melanocytes.¹⁴ The amount of pigment is controlled to be suitable. This process is called melanogenesis.^{14,15}

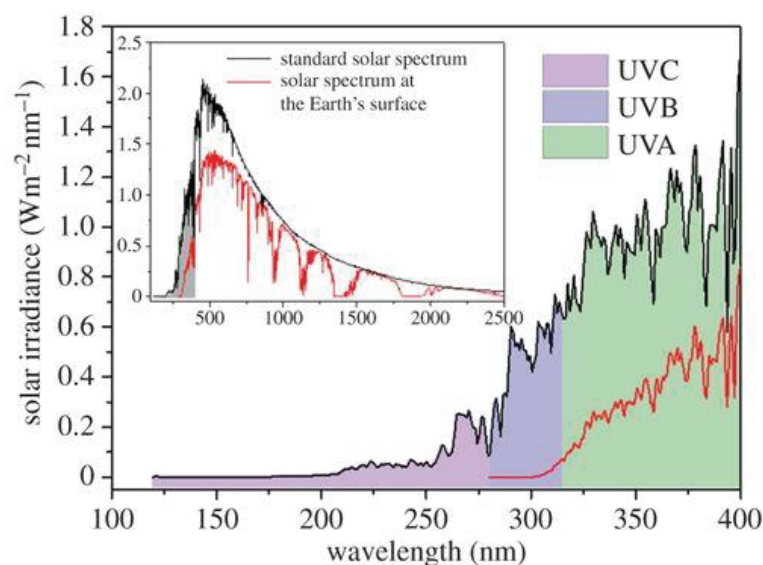


Figure 1 (Black curve) Standard solar spectrum and (Red curve) the solar spectrum after the atmosphere effects. The shade of violet, blue and green color represents the wavelength region of UV-C, UV-B and UV-A, respectively. The inset is the total solar spectrum.^{2,3}

Sunscreen cosmetics are used in our daily life. It is categorized into two main groups; inorganic scatter and organic filter. The common examples of inorganic scatter are nanoparticles of TiO_2 and ZnO , which reflect or scatter the UV light.¹⁶ On the other hand, in ref. 3, it is mentioned that there are roughly seven main categories of organic filters as shown in Figure 2.

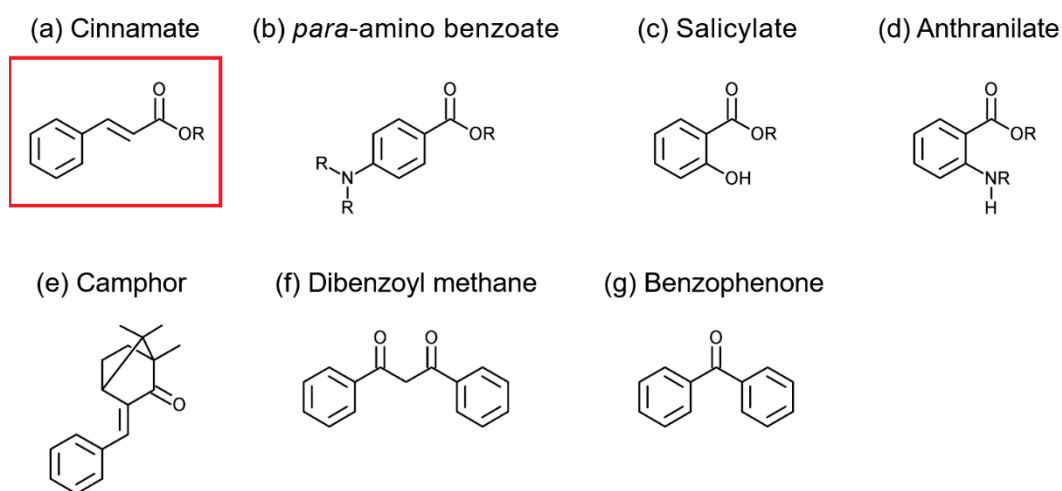


Figure 2 Seven main categories of the organic filter. Derivatives of (a) cinnamate, (b) *para*-amino benzoate, (c) salicylate, (d) anthranilate, (e) camphor, (f) dibenzoyl methane and (g) benzophenone.³

Figure 3 shows an example of the potential energy surfaces (PESs) and photochemical/photophysical decay process of the organic filter. It first absorbs UV light and is excited to the higher energy electronic state (S_2). After the vibrational relaxation (VR) in the S_2 state, it decays to the S_1 state *via* internal conversion (IC), which is the nonradiative decay (NRD) process between two electronic states with the same spin multiplicity. From the S_1 state, it decays to the higher triplet state (T_2) *via* intersystem crossing (ISC), which is the NRD process between two electronic states with the different spin multiplicity. The molecule in the T_2 state then decays to the T_1 state by IC, and finally decays to the S_0 state *via* ISC. The above ICs and ISCs should occur through the conical intersections (CIs) and seam of crossings (SXs). These are crossing points

between different two PESs. In addition to the above NRD processes, the radiative process will compete. An excited molecule can decay to the lower state (S_0) by emitting of photons, whose energy corresponds to the energy difference between upper and lower states. When the spin multiplicity of these two states is same, the emission corresponds to fluorescence (Fluo.), otherwise to phosphorescence (Phos.). The typical time scales of the decay processes are listed in Table 1. For the ideal sunscreen reagent, an effective NRD process is favorable, because the process can rapidly change the UV energy to the thermal energy.

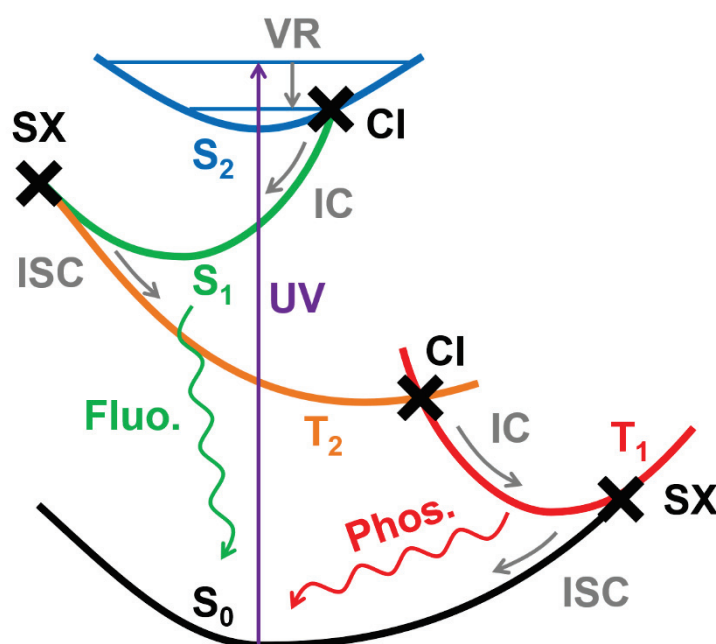


Figure 3 PESs and photochemical/photophysical decay process upon photoexcitation by the UV light. The CIs and SXs are indicated as crosses.

Table 1 Typical time scales of the decay processes which occur upon photoexcitation.¹³

Process	Time (s)
Absorption	$10^{-18} - 10^{-15}$
Vibrational relaxation	$10^{-12} - 10^{-10}$
Internal conversion	$10^{-11} - 10^{-9}$
Intersystem crossing	$10^{-10} - 10^{-8}$
Fluorescence	$10^{-10} - 10^{-7}$
Phosphorescence	$10^{-6} - 1$

Cinnamic acids and cinnamate derivatives, circled with a red square in Figure 2, are one of the chemical sunscreens, which have unsaturated carboxylic or ester group on their phenyl group. Cinnamates adopt a stable *trans* (*E*) form in the S_0 state. Upon UV-B absorption, cinnamates are mostly excited to the optically “bright” $^1\pi\pi^*$ state and rapidly relax *via* several NRD processes, and finally return to the *trans* (*E*) form or isomerize to the *cis* (*Z*) form as seen in Figure 4.¹⁷⁻²¹ Through these NRD process involving the photoisomerization, cinnamates can convert harmful UV energy to safe heat. Octyl methoxy cinnamate and sinapoyl malate is commonly used as a sunscreen in cosmetics and plants, respectively.²²

Cinnamates also exist in bacteria as chromophores.^{23,24} The photoisomerization is a trigger of negative phototaxis against blue light.

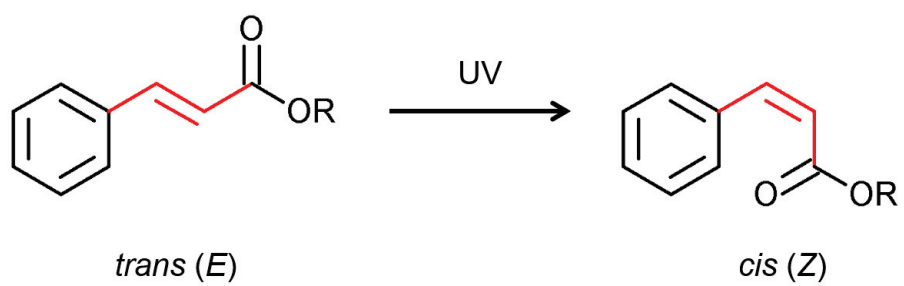


Figure 4 *trans* (*E*) \rightarrow *cis* (*Z*) photoisomerization of cinnamates

1-2 Studies on the photochemistry of cinnamates

Up to now, many experimental and theoretical studies on the electronic states, their lifetime and NRD route involving photoisomerization of cinnamates have been carried out for a development of sunscreens.^{3,13,19,20,25-49} Many results mentioned below indicate that the photochemistry of cinnamates is very sensitive to the substituent at the phenyl ring and hydrogen (H)-bonding with a solvate molecule.

The $^1\pi\pi^*$ state lifetime of the $^1\pi\pi^*$ state for cinnamic acids and cinnamates in the gas-phase is in the range from a few picoseconds to a few tens of nanoseconds, and is quite different depending on the substituent on the phenyl group. For example, the $^1\pi\pi^*$ lifetime of methylcinnamate (MC) was recently measured as 4.5 ps by femtosecond pump-probe spectroscopy.²⁵ Substitution with an OCH₃ group at the *para* position of MC slightly elongates the $^1\pi\pi^*$ lifetime, while the substitution at *meta* or *ortho* position drastically elongates the lifetime by three orders of magnitude.²⁶ On the other hand, the substitution effect at the ester part on the $^1\pi\pi^*$ lifetime is rather small. For example, the reported $^1\pi\pi^*$ lifetime of *para*-methoxy MC (*p*-MMC), *para*-methoxy ethylcinnamate, and octyl methoxycinnamate is 280 ps, 70 ps and 40 ps, respectively.^{26,27,28}

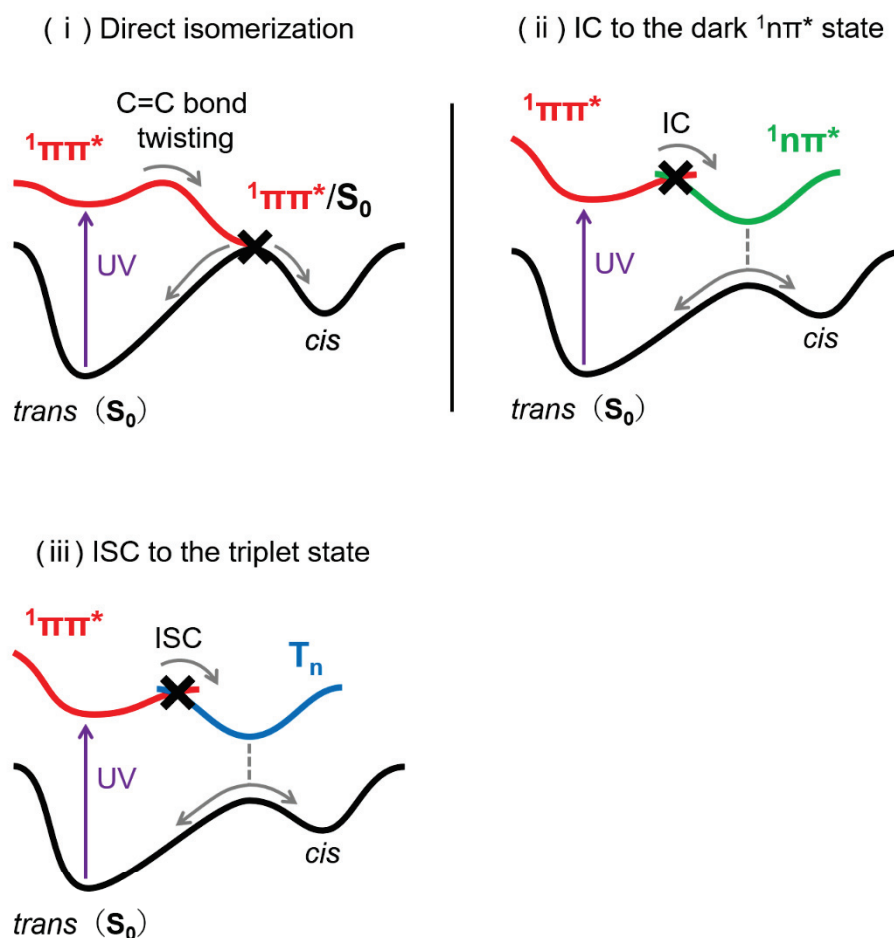


Figure 5 Three suggested NRD/photoisomerization routes for cinnamate. (i) the direct $trans \rightarrow cis$ isomerization, (ii) IC to the dark ${}^1n\pi^*$ state, and (iii) ISC to the triplet state.

In spite of many studies on the photochemistry of cinnamates, the dominant NRD/photoisomerization route has not been understood completely, because the optically “dark” states, such as ${}^1n\pi^*$ and triplet states, are thought to be involved in the route. For example, three possible NRD route from the ${}^1\pi\pi^*$ state have been proposed;²⁵⁻³⁵ (i) the direct $trans \rightarrow cis$ isomerization *via* ${}^1\pi\pi^*/S_0$

CI, (ii) IC to the dark $^1n\pi^*$ state, and (iii) ISC to the triplet state as summarized in Figure 5. The quantum chemical calculation suggests that both of (i) and (ii) routes are possible in *p*-MMC due to their small energy barrier.²⁶ Buma and co-workers first found the dark state, which has a lifetime of ~ 25 ns for *p*-MMC and *para*-hydroxy MC (*p*-HMC) by using a nanosecond pump-probe measurement with the probe laser of 193 nm, and proposed that the dark state would be energetically lower $^1n\pi^*$ state generated upon IC from the $^1\pi\pi^*$ state.^{30,31} However, the energy level as well as character of the dark state has not been revealed, because the frequency of the probe laser was not tunable.

Interestingly, such a long-lived dark state is not found in jet-cooled micro solvated cinnamates, which is 1:1 complex of cinnamate with a solvent molecule, such as a H₂O.^{30,31,36} In addition, the $^1\pi\pi^*$ lifetime is drastically changed by the H-bonding with solvent molecules.^{26,29,37} This means that the NRD process is also affected by the H-bonding and thought to be different between the bare cinnamate and the 1:1 complex.

The femtosecond transient absorption spectroscopy in the solution phase has been also performed by several groups.³⁸⁻⁴⁸ It was reported that upon $^1\pi\pi^*$ absorption, the NRD process involving the photoisomerization proceeds *via* $^1\pi\pi^*/S_0$ CI and this process depends on the surrounding environment, such as pH, polarization and viscosity of solution.

In addition to the photoisomerization, several studies on the photostability against UV irradiation were reported.^{35,49,50} For example, it was

reported that intra molecular H-bonding in cinnamate increases its photostability. The phenolic O-H bond in cinnamates is easily dissociated by UV (~270 nm) irradiation, however intra molecular H-bonding suppresses the O-H bond dissociation and generation of phenoxy radical, which is called reactive oxygen species and will cause harmful effects, such as a skin aging *via* oxidative stress pathway.⁵¹

1-3 Purpose and outline of this study

From these studies mentioned above, three important issues are pointed out to understand the NRD process involving the photoisomerization of cinnamates. The first issue is the detection and assignment of the dark state generated during the NRD process. The second and third issues are the substitution and solvation effects on the electronic states and the NRD/photoisomerization routes.

The target cinnamates in this thesis are MC, structural isomers of HMC (*p*, *m*, *o*-HMC) and *p*-MMC as shown in Chart 1. At first, nanosecond UV-tunable DUV pump-probe spectroscopy is newly developed to determine the energy level of the transient dark state. In addition, systematic exploration for the dominant NRD/photoisomerization route is performed by using the artificial force induced reaction method with (time-dependent) density functional theory calculation. Second, the substitution and its position effects are further examined by measuring the $^1\pi\pi^*$ lifetime, detecting the transient state, exploring the dominant NRD/photoisomerization route and evaluating the energy of the molecular orbitals responsible for the $^1n\pi^*$ and $^1\pi\pi^*$ transitions. Third, the electronic states and NRD process of micro solvated MC with a methanol, which is thought as a model in solution, is also investigated and compared with absorption/fluorescence spectra in solution to reveal the H-bonding effects. Finally, this thesis aims to provide molecular design for the effective cinnamate-based sunscreens.

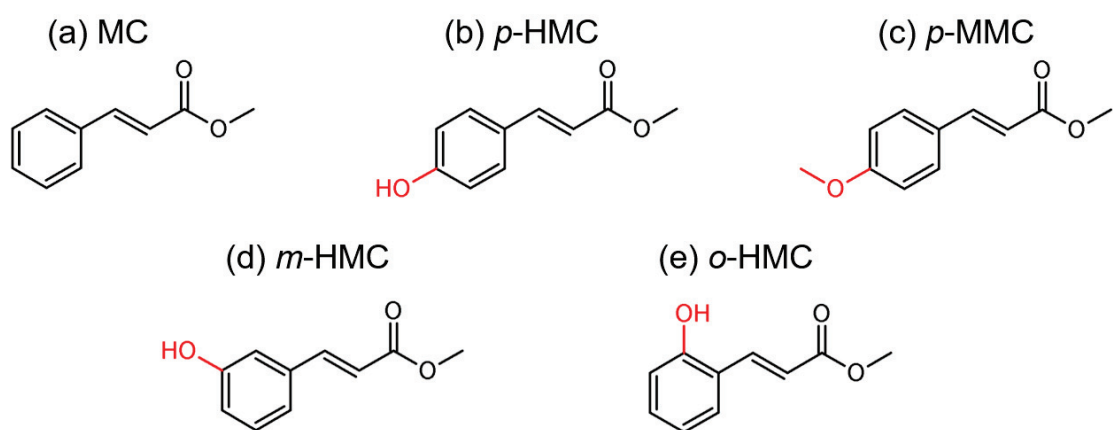


Chart 1 Chemical structures of (a) MC, (b) *p*-HMC, (c) *p*-MMC, (d) *m*-HMC and (e) *o*-HMC.

References

1. World Health Organization 2002 Global solar UV index: a practical guide, Meteorological Organization, UN Environment Programme, International Commission on Non-Ionizing Radiation Protection. Geneva, Switzerland: WHO.
2. National Renewable Energy Laboratory.
<http://www.nrel.gov/iredc/>(accessed June 2016).
3. N. D. N. Rodrigues, M. Staniforth and V. G. Stavros, *Proc. R. Soc. A*, 2016, **472**, 20160677.
4. J. E. Frederick, H. E. Snell and E. K. Haywood, *Photochem. Photobiol.*, 1989, **50**, 443-450.
5. M. F. Holick, *N. Engl. J. Med.*, 2007, **357**, 266-281.
6. M. F. Holick, *Am. J. Clin. Nutr.* 2004, **80**, 1678S-1688S.
7. R. P. Sinha and D. P. Häder, *Photochem. Photobiol. Sci.*, 2002, **1**, 225-236.
8. F. R. de Gruijl, *Methods Enzymol.*, 2000, **319**, 359-366.
9. I. Schulz, H-C. Mahler, S. Boiteux and B. Epe, *Mutation. Res.*, 2000, **461**, 145-156.
10. F. L. Meyskens Jr., P. Farmer, and J. P. Fruehauf, *Pigm. Cell. Research.*, 2001, **14**,148-154.
11. D. L. Narayanan, R. N. Saladi and J. L. Fox, *Int. J. Dermatol.*, 2010, **49**, 978-986.
12. D.S. Rigel, *J. Am. Acad. Dermatol.*, 2008, **58**, S129-S132.
13. L. A. Baker and V. G. Stavros, *Sci. Prog.*, 2016, **99**, 282-311.
14. M. Cichorek, M. Wachulska, A. Stasiewicz and A. Tyimińska, *Postępy. Dermatol. Alergol.*, 2013, **30**, 30-41.
15. R. S. Mason and J. Reichrath, *Anticancer Agents Med. Chem.*, 2013, **13**, 83-97.
16. M. I. Cabrera, O. M. Alfano and A. E. Cassano, *J. Phys. Chem.*, 1996, **100**, 20043-20050.
17. B. Danylec and M. N. Iskander, *Chem. Educ.*, 2002, **79**, 1000-1001.
18. H. El-Gezawy, W. Rettig, A. Danel and G. Jonusauskas, *J. Phys. Chem. B*, 2005, **109**, 18699-18705.
19. Y. Miyazaki, Y. Inokuchi, N. Akai and T. Ebata, *J. Phys. Chem. Lett.*, 2015, **6**, 1134-1139.
20. R. B. Rodríguez, R. L. Zapata, M. L. Salum and R. Erra-Balsells, *Photochem. Photobiol. Sci.*, 2020, **19**, 819-830.
21. Y. Shindo , K. Horie and I. Mita, *J. Photochem.*, 1984, **26**, 185-192.

22. R. Shuab, R. Lone and K. K. Koul, *Acta. Physiol. Plant.*, 2016, **38**, 64.
23. H. Kuramochi, S. Takeuchi and T. Tahara, *J. Phys. Chem. Lett.*, 2012, **3**, 2025-2029.
24. H. Kuramochi, S. Takeuchi, K. Yonezawa, H. Kamikubo, M. Kataoka and T. Tahara, *Nat. Chem.*, 2017, **9**, 660-666.
25. K. M. Krokidi, M. A. P. Turner, P. A. J. Percy and V. G. Stavros, *Mol. Phys.*, 2020, DOI: 10.1080/00268976.2020.1811910.
26. Y. Miyazaki, K. Yamamoto, J. Aoki, T. Ikeda, Y. Inokuchi, M. Ehara, and T. Ebata, *J. Chem. Phys.*, 2014, **141**, 244313.
27. K. Yamazaki, Y. Miyazaki, Y. Harabuchi, T. Taketsugu, S. Maeda, Y. Inokuchi, S. Kinoshita, M. Sumida, Y. Onitsuka, H. Kohguchi, M. Ehara and T. Ebata, *J. Phys. Chem. Lett.*, 2016, **7**, 4001-4007.
28. S. Muramatsu, S. Nakayama, S. Kinoshita, Y. Onitsuka, H. Kohguchi, Y. Inokuchi, C. Zhu and T. Ebata, *J. Phys. Chem. A*, 2020, **124**, 1272-1278.
29. D. Shimada, R. Kusaka, Y. Inokuchi, M. Ehara and T. Ebata, *Phys. Chem. Chem. Phys.*, 2012, **14**, 8999-9005.
30. E. M. M. Tan, M. Hilbers and W. J. Buma, *J. Phys. Chem. Lett.*, 2014, **5**, 2464-2468.
31. E. M. M. Tan, S. Amirjalayer, B. H. Bakker and W. J. Buma, *Faraday Discuss.*, 2013, **163**, 321-340.
32. J. Moon, H. Baek, J. S. Lim and J. Kim, *Bull. Korean Chem. Soc.*, 2018, **39**, 427-434.
33. X.-Y. Xie, C.-X. Li, Q. Fang and G. Cui, *J. Phys. Chem. A*, 2016, **120**, 6014-6022.
34. X. P. Chang, C. X. Li, B.-B. Xie and G. Cui, *J. Phys. Chem. A*, 2015, **119**, 11488-11497.
35. T. N. V. Karsili, B. Marchetti, M. N. R. Ashfold and W. Domcke, *J. Phys. Chem. A*, 2014, **118**, 11999-12010.
36. J. Fan, W. Roeterdink and W. J. Buma, *Mol. Sci.*, 2020, DOI: 10.1080/00268976.2020.1825850
37. Y. Iida, S. Kinoshita, S. Kenjo, S. Muramatsu, Y. Inokuchi, C. Zhu and T. Ebata, *J. Phys. Chem. A*, 2020, **124**, 5580-5589.
38. X. Zhao, J. Luo, Y. Liu, P. Pandey, S. Yang, D. Wei and K. Han, *J. Phys. Chem. Lett.*, 2019, **10**, 5244-5249.
39. X. Zhao, J. Luo, S. Yang and K. Han, *J. Phys. Chem. Lett.*, 2019, **10**, 4197-4202.
40. J. Luo, Y. Liu, S. Yang, A. L. Flourat, F. Allais and K. Han, *J. Phys. Chem. Lett.*, 2017, **8**, 1025-1030.

41. L. A. Baker, M. Staniforth, A. L. Flourat, F. Allais and V. G. Stavros, *ChemPhysChem.*, 2020, **21**, 2006-2011.
42. M. D. Horbury, E. L. Holt, L. M. M. Mouterde, P. Balaguer, J. Cebrián, L. Blasco, F. Allais and V. G. Stavros, *Nat. Commun.*, 2019, **10**, 4748.
43. J. M. Woolley, J. S. Peters, M. A. P. Turner, G. J. Clarkson, M. D. Horbury and V. G. Stavros, *Phys. Chem. Chem. Phys.*, 2019, **21**, 14350-1435.
44. M. D. Horbury, A. L. Flourat, S. E. Greenough, F. Allais and V. G. Stavros, *Chem. Commun.*, 2018, **54**, 936-939.
45. M. D. Horbury, W.-D. Quan, A. L. Flourat, F. Allais and V. G. Stavros, *Phys. Chem. Chem. Phys.*, 2017, **19**, 21127-21131.
46. L. A. Baker, M. D. Horbury, S. E. Greenough, F. Allais, P. S. Walsh, S. Habershon and V. G. Stavros, *J. Phys. Chem. Lett.*, 2016, **7**, 56-61.
47. M. D. Horbury, L. A. Baker, W.-D. Quan, S. E. Greenough and V. G. Stavros, *Phys. Chem. Chem. Phys.*, 2016, **18**, 17691-17697.
48. Y. Peperstraete, M. Staniforth, L. A. Baker, N. D. N. Rodrigues, N. C. Cole-Filipiak, W.-D. Quana and V. G. Stavros, *Phys. Chem. Chem. Phys.*, 2016, **18**, 28140-28149.
49. N. D. N. Rodrigues, M. Staniforth, J. D. Young, Y. Peperstraete, N. C. Cole-Filipiak, J. R. Gord, P. S. Walsh, D. M. Hewett, T. S. Zwier and V. G. Stavros, *Faraday Discuss.*, 2016, **194**, 709-729.
50. J. D. Young, M. Staniforth, J. C. Dean, G. M. Roberts, F. Mazzoni, T. N. V. Karsili, M. N. R. Ashfold, T. S. Zwier and V. G. Stavros, *J. Phys. Chem. Lett.*, 2014, **5**, 2138-2143.
51. F. Poon, S. Kang and A. L. Chien, *Photodermatol. Photoimmunol. Photomed.*, 2015, **31**, 65-74.

Chapter 2

Experimental and Theoretical methods

2-1 Supersonic jet

For understanding a detail of electronic and vibrational structure, measuring well-resolved spectrum is necessary. Thus, in this study, the supersonic jet/laser spectroscopy was applied. At room temperature, only a broad and structure less spectrum is obtained due to an overlap of many transitions from high vibrational and rotational levels. In solution, the solvent molecules also perturb the spectrum.

The details of the supersonic jet is described in ref. 1. Briefly, the schematic view of supersonic free jet and molecular beam is shown in Figure 1. In a vacuum chamber ($\sim 10^{-5}$ Torr), the sample housing was attached at pulsed valve and heated to obtain enough vapor pressure for cinnamates. The mixture of vaporized cinnamates and carrier gas (He or Ar) collided with each other and they were ejected into the chamber at a total pressure of ~ 5 atm. After the collision, their relative velocity became almost zero, corresponding a low translational temperature. By setting a skimmer at the downstream of sample housing, jet-cooled molecular beam was obtained. The micro solvated cinnamates with methanol were generated by mixing the vapor of methanol into the carrier gas.

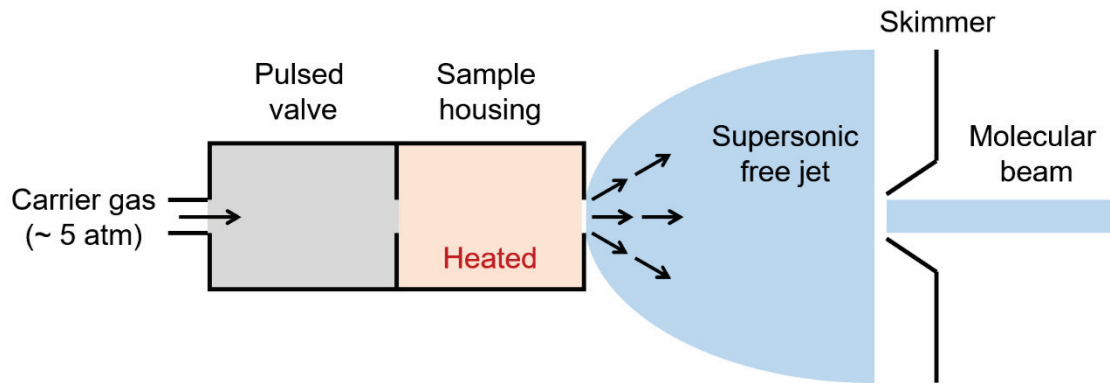


Figure 1 Schematic view of a supersonic free jet and molecular beam.

2-2 Measurement of electronic spectra under jet-cooled condition

Two vacuum chambers were used for the spectroscopy of jet-cooled cinnamates. For the measurement of laser induced fluorescence (LIF) excitation spectrum, a free-jet expansion chamber was used. The energy level diagram is shown in Figure 2-(a). A tunable UV laser pulse was introduced onto the jet-cooled cinnamates at 20 mm downstream of the nozzle. The total fluorescence was collected by a series of lenses and detected using a photomultiplier tube (Hamamatsu Photonics 1P28). A band pass filter was used to eliminate the scatter of laser light. By plotting fluorescence signal as a function of UV frequency, LIF excitation spectrum was obtained.

In addition, in order to obtain conformer specific spectrum, UV-UV' hole-burning (HB) spectroscopy was carried out. The energy level diagram is shown in Figure 2-(b). The probe UV' laser (ν_2) was fixed to a vibronic band of interest, monitoring its fluorescence signal. The hole UV laser (ν_1) was irradiated and scanned at ~ 10 mm upstream of the crossing point between the jet and the probe laser at ~ 4 μ s prior to the probe laser pulse. A depletion of the fluorescence signal was observed due to depopulation of the ground state (S_0) induced by the hole laser.² By plotting the fluorescence signal as a function of UV frequency, UV-UV' HB spectrum was obtained.

For the measurement of resonance two-photon ionization (R2PI) spectrum, the molecular beam chamber equipped with a time-of-flight mass spectrometer (50 cm) was used. The energy level diagram is shown in Figure 2-

(c). Here, two-color (2C)-R2PI scheme, which has a higher frequency of ionization laser (ν_2) than the pump laser (ν_1), was adopted. This is due to the fact that the energies of the S_1 state is lower than half of the ionization potential (IP) and a higher frequency laser is necessary for the ionization step. By plotting mass-selected ion signal as a function of UV frequency, R2PI spectrum was obtained.

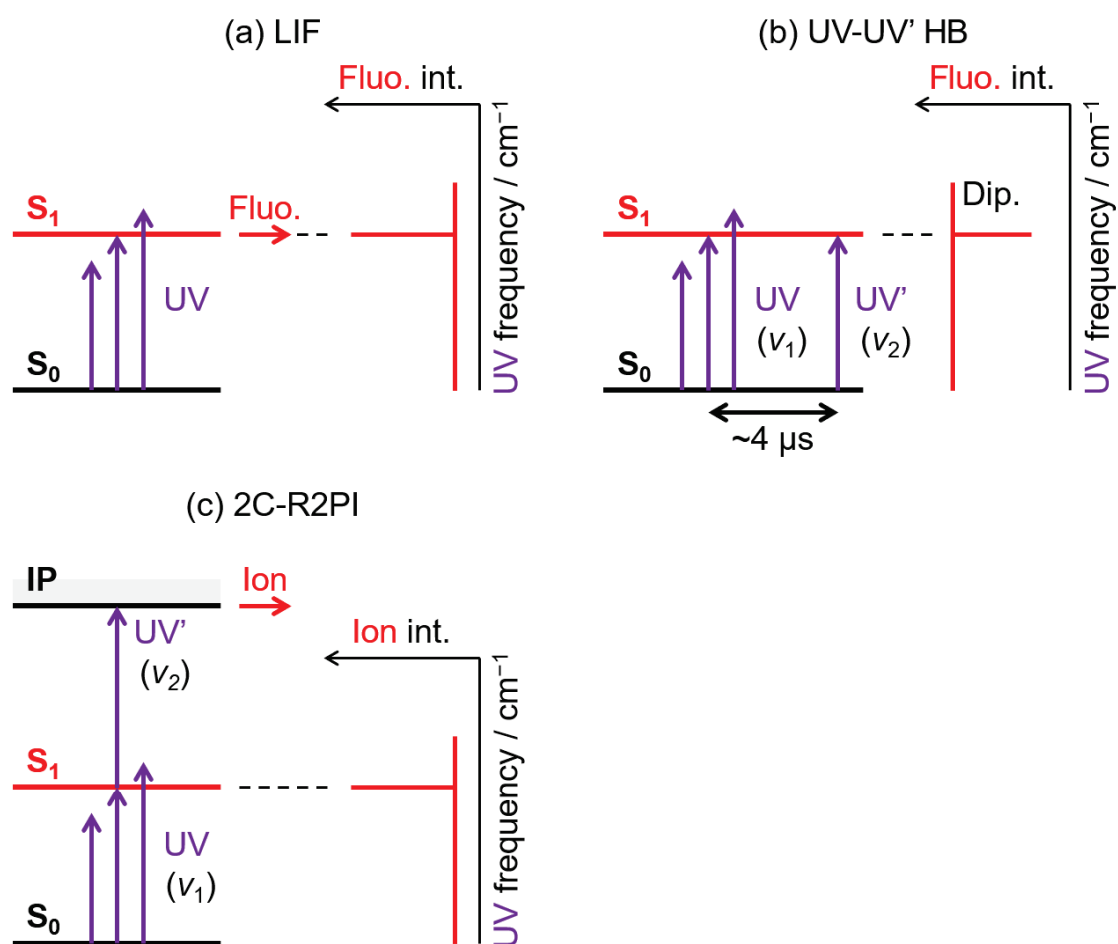


Figure 2 Energy level diagrams of (a) LIF, (b) UV-UV' HB and (c) 2C-R2PI measurements.

2-3 Lifetime measurement of excited state

The fluorescence lifetime of excited states was determined by observing the fluorescence decay profile. A fast response photomultiplier tube (Hamamatsu Photonics R9880U) was used to detect the fluorescence. The lifetime was obtained by deconvolution of the time profile, assuming a laser pulse width of 5 ns.

For the picosecond (ps) UV-UV' pump-probe measurement, two tunable picosecond laser pulses (Ekspra PL2143S/PG401SH) with a pulse width of 12 ps were used. The energy level diagram of the measurement is shown in Figure 3. The first UV laser (ν_1) pumps the cinnamates to the vibronic level of the excited state, and the second UV' laser (ν_2) ionizes the excited cinnamates. The delay time (Δt_1) between the two laser pulses was controlled by an optical delay line. The decay profile of the excited cinnamates was analyzed by deconvolution, assuming a laser pulse width of 12 ps. Then, the lifetime of the S_1 state (τ_1) was obtained.

For nanosecond (ns) UV-tunable deep UV (DUV) pump-probe spectroscopy, the DUV light in the range of 198-230 nm was generated by sum frequency mixing (SFM) of 1064 nm and 243-294 nm with a BBO crystal. The fundamental of a YAG laser and a frequency doubled output of a dye laser pumped by the YAG laser was overlapped on the crystal after adjusting the size and the delay of the two laser beams. A typical conversion efficiency of the SFM generation was 10 % with respect to the near UV pulse energy, providing intense

enough DUV pulse for the present measurement.³ The energy level diagram of the measurement is shown in Figure 3. The dark state generated during nonradiative decay (NRD) process was ionized and detected by the DUV light. The delay time (Δt_2) between the pump UV (ν_1) and ionization DUV laser (ν_2) was controlled by using digital delay/pulse generator. The decay profile of the transient state was analyzed by deconvolution with a laser pulse width of 5 ns. Then, the lifetime of the transient state (τ_2) was obtained. By scanning the ν_2 , the energy level was estimated.

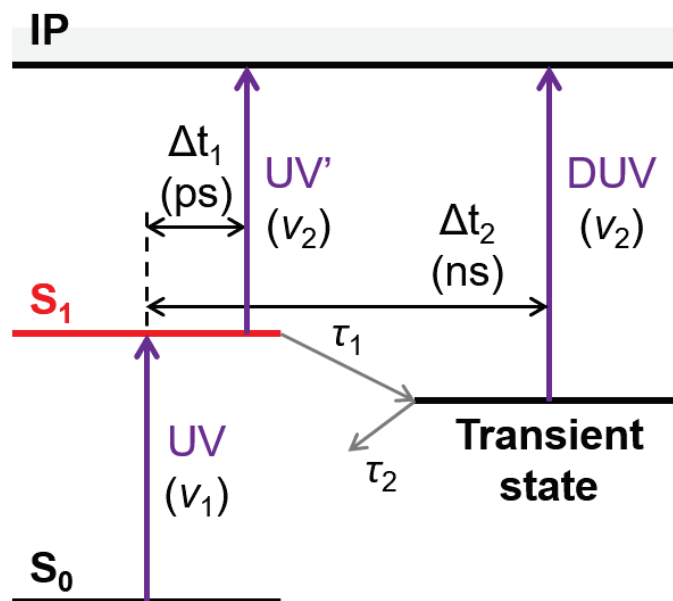


Figure 3 Energy level diagram of ps UV-UV' and ns UV-DUV pump-probe measurements

2-4 Cold matrix-isolation FTIR spectroscopy

The experimental set up of cold matrix-isolation FTIR spectroscopy is shown in Figure 4. The detail of set up is described in ref. 4. Briefly, cinnamate powder was vaporized at 302 K and deposited with Ne gas on a CsI plate cooled at 6 K by a closed-cycle helium refrigerator (Iwatani, Cryo Mini) in vacuum chamber. Two hours were required to prepare the matrix sample. The IR spectrum of the matrix-isolated samples was measured using an FTIR spectrophotometer (JEOL, SPX200ST) with an accumulation number of 100. The spectral resolution is 0.5 cm^{-1} . A Xe lamp (Asahi Spectra, MAX-301uv) was used as the UV light source and narrowed by using short-wavelength cutoff filters. For identifying the photoproduct, the obtained difference IR spectrum before and after UV irradiation was compared with the calculated one at the B3LYP/6-311++G(d,p) level.

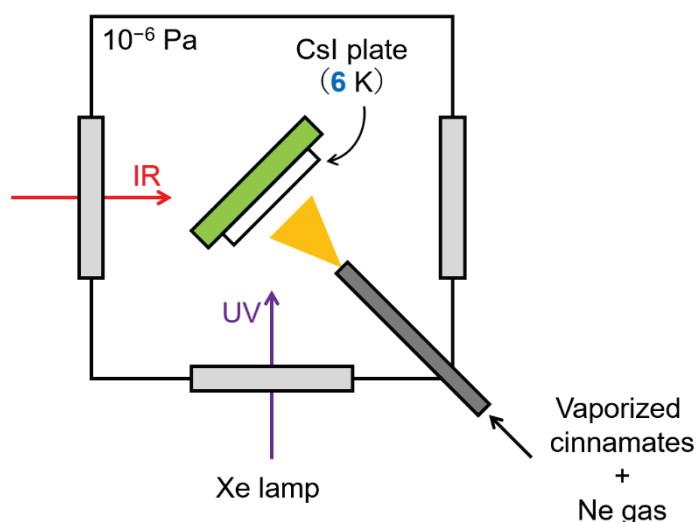


Figure 4 Experimental set up of the cold matrix-isolation FTIR spectroscopy

2-5 Sample preparation

MC (> 99% in purity) and *p*-HMC (> 96% in purity) were purchased from TCI chemicals and used without further purification.

White powdery *p*-MMC was prepared from *p*-hydroxycinnamic acid. To the solution of *p*-hydroxycinnamic acid (1.00 g, 6.1 mmol) and potassium carbonate (8.53 g, 61 mmol), iodomethane (2.3 mL, 36 mmol) was added and stirred for 72 hours under reflux. The resulting mixture was filtered, and the filtrate was evaporated under vacuum. The residue was dissolved by adding ethyl acetate (50 mL), washed with water and brine, dried over Na₂SO₄, and evaporated under vacuum. The recrystallization from ethyl acetate/hexane gave *p*-MMC (0.47 g, 40%) as colorless crystal.²

o-HMC and *m*-HMC were synthesized by the Wittig reaction of hydroxy benzaldehyde and methyl diethylphosphonoacetate.⁵ K₂CO₃ (3.876 g) was slowly added to a mixture of *o*-hydroxy benzaldehyde (3.43 g, 28.1 mmol) and methyl diethylphosphonoacetate (5.09 mL, 36.3 mmol) in toluene (50 mL) and refluxed at 100 °C for 5 hours. After completion of the reaction, 60% NaH was added to neutralize the solution. The crude product was washed with brine, dried with MgSO₄, and recrystallized in methanol to give white powdery *o*-HMC (3.90 g, 78% yield). Similarly, K₂CO₃ was added slowly to a mixture of *m*-hydroxy benzaldehyde (3.43 g, 28.1 mmol) and methyl diethylphosphonoacetate (5.09 mL, 36.3 mmol) in THF (50 mL) and refluxed at 70 °C for one night. After the reaction was completed, NH₄Cl was added to neutralize the solution. The crude product

was washed with water and ethyl ether, dried with MgSO_4 , and recrystallized in methanol to give white powdery *m*-HMC (4.10 g, 82% yield).

2-6 Systematic search for the NRD/photoisomerization route

For the systematic search for the NRD/photoisomerization routes of methylcinnamate (MC), density functional theory (DFT) and time-dependent DFT (TD-DFT) calculations were performed with the development version of the global reaction route mapping program⁶ interfaced with the Gaussian 16 quantum chemistry package⁷.

First, the internal conversion (IC) route from the $^1\pi\pi^*$ state was investigated. The $^1\pi\pi^*$ and $^1n\pi^*$ minima (EQs) and the transition state (TS) between them were optimized at the TD- ω B97XD/6-311G(d,p) level.

Next, the intersystem crossing (ISC) route from the $^1n\pi^*$ or $^1\pi\pi^*$ state was investigated. Minimum energy seams of crossings (MESXs) between the S_1 ($^1n\pi^*$ or $^1\pi\pi^*$) and T_n ($n = 2, 3$) states were optimized at the TD- ω B97XD/6-311G(d,p) level.

The minimum energy conical intersections (MECIs) between the T_2 and T_1 states, were searched by the single-component artificial force induced reaction (SC-AFIR) method⁸⁻¹¹ at the TD- ω B97XD/6-311G(d,p) level. Here, the AFIR method is briefly described. The idea is simple; just push the reactant atoms A and B together and pull them apart. Figure 5 (a) shows a potential curve $E(r_{AB})$ between two atoms A and B as a function of their distance r_{AB} . A barrier separates the A + B region from the product AB region. By adding force term αr_{AB} , a linear function of r_{AB} with a parameter α , the curve $F(r_{AB})$ loses the barrier as shown in Figure 5 (b). On $E(r_{AB})$, the barrier prevents efficient search for the AB region

starting from the A + B region, whereas on $F(r_{AB})$ one can easily get to the product AB starting from the A + B region by minimizing $F(r_{AB})$.

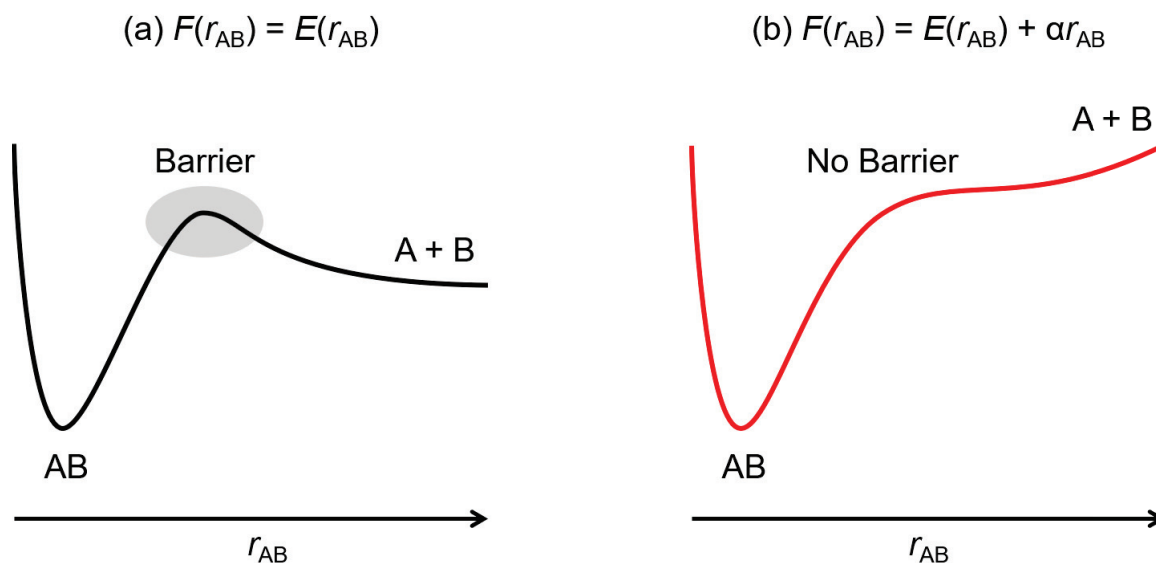


Figure 5 (a) A potential curve $E(r_{AB})$ between two atoms A and B as a function of their distance r_{AB} and (b) AFIR function $F(r_{AB})$. The barrier along $E(r_{AB})$ disappears on $F(r_{AB})$ due to the force term αr_{AB} .

The EQs of the T_1 ($^3\pi\pi^*$) and the MESXs between the T_1 ($^3\pi\pi^*$) and S_0 state were also explored at the U ω B97XD/6-31G(d) level. The MECI/MESX search using the SC-AFIR method can investigate much larger configurational space than manual search and gives us a surprising number of MECI structures. This method has been already applied successfully to the nonradiative processes

in many organic and inorganic systems and obtained the low-lying MECIs/MESXs involved in their NRD processes.^{3,9-16}

For the investigation of the direct isomerization route, which is C=C rotation coordinate on the $^1\pi\pi^*$ state, the geometries of $^1\pi\pi^*/S_0$ MECIs and TSs on the $^1\pi\pi^*$ state were also optimized. The energy shift technique¹⁷⁻¹⁹ was applied for the $^1\pi\pi^*/S_0$ MECI to avoid the instability of TD-DFT calculations nearby the MECI. Initial geometries of the MECIs were created by the SC-AFIR method at the TD- ω B97XD/6-31G(d) level. For the MECI search both of *meta*- and *ortho*-hydroxy MC (*m*-, *o*-HMC), spin-flip TDDFT theory with BHandHLYP functional²⁰ was applied for the initial search. The 6-31G(d) and 6-31G(d,p) basis set was used for the structure search and the refinement, respectively.

In all the SC-AFIR searches, the model collision energy parameter was set to $\gamma = 100 \text{ kJ mol}^{-1}$, and all the carbon atoms, oxygen atoms and hydrogen atoms in the vinyl C=C bond were accounted as the target atoms as shown in Chart 1. All of the obtained EQs in the T_1 state and T_1/S_0 MESXs were further optimized at the U ω B97XD/6-311G(d,p) level, and all the other TS, MESXs, MECIs and EQs were optimized at the TD- ω B97XD/6-311G(d,p) level.

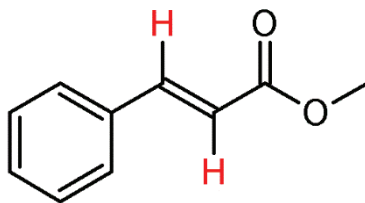


Chart 1 Target atoms for the AFIR method: all the carbon atoms, oxygen atoms and hydrogen atoms (indicated as red) in the vinyl C=C bond.

The decay routes for all the optimized structures were surveyed by calculating the intrinsic reaction coordinates (IRCs) and the meta-IRCs, where IRC and meta-IRC corresponds to the steepest decent path starting from the first-order saddle point and those from non-stationary points, respectively.

2-7 Calculation of spin-orbit coupling constant

To evaluate the efficiency of the ISC ($^1n\pi^*$ or $^1\pi\pi^* \rightarrow$ triplet state) process, the spin-orbit coupling (SOC) constant at the optimized MESX was calculated by using the TD- ω B97XD/6-311G(d,p) level of theory using the Breit-Pauli spin-orbit Hamiltonian with effective charge approximation,²¹⁻²³ implemented in the PySOC program.^{24,25} It is known that the SOC value evaluated by the TD- ω B97XD level well reproduce those calculated by computationally more demanding multistate complete active space second order perturbation theory (MS-CASPT2).²⁵ The single-point energy calculation for the SOC evaluation was performed by the Gaussian 09 quantum chemistry package.²⁶

The SOC constant at T_1/S_0 MESX was evaluated at the MS-CASPT2²⁷/ANO-RCC-VTZP²⁸ level of theory with active space of 10 electrons in 9 orbitals ([10e, 9o]-MS-CASPT2). Mean field spin-orbit Hamiltonian and SOC between the T_1 and S_0 states²⁹ were used. The SOC values were evaluated by using the restricted active space state interaction approach.³⁰ The OpenMolcas 18.09 quantum chemistry package²⁷ was used for the MS-CASPT2 calculations.

2-8 Rate constant of radiative decay

The rate constant of radiative decay k_{rad} was estimated using Fermi's golden rule.

The k_{rad} is represented as a function of the vertical emission energy $\hbar\omega$ and the oscillator strength $f(\omega)$ at the EQ (${}^1\pi\pi^*$),³¹

$$k_{rad} = \frac{e\omega^3}{2\pi\epsilon_0 m_e c^3} f(\omega) \quad (1)$$

where e , ϵ_0 , m_e , and c is the elemental charge of the electron, the vacuum permittivity, the mass of the electron, and the speed of light, respectively.

References

1. N. Mikami, Oyo Buturi, 1980, **49**, 802-812.
2. Y. Miyazaki, K. Yamamoto, J. Aoki, T. Ikeda, Y. Inokuchi, M. Ehara and T. Ebata, *J. Chem. Phys.*, 2014, **141**, 244313.
3. K. Yamazaki, Y. Miyazaki, Y. Harabuchi, T. Taketsugu, S. Maeda, Y. Inokuchi, S. Kinoshita, M. Sumida, Y. Onitsuka, H. Kohguchi, M. Ehara and T. Ebata, *J. Phys. Chem. Lett.*, 2016, **7**, 4001-4007.
4. Y. Miyazaki, Y. Inokuchi, N. Akai and T. Ebata, *J. Phys. Chem. Lett.*, 2015, **6**, 1134-1139.
5. W. Hongbo, L. Yun, X. Ke, C. Bin, W. Huifei, H. Lin and Z. Hongbin, *Org. Lett.*, 2015, **17**, 5974-5977.
6. S. Maeda, Y. Harabuchi, K. Takagi, K. Saita, T. Suzuki, Y. Ichino, K. Sumiya, K. Sugiyama and Y. Ono, *J. Comput. Chem.*, 2018, **39**, 233-250.
7. M. J. Frisch, G. W. Trucks, H. B. Schlegel, G. E. Scuseria, M. A. Robb, J. R. Cheeseman, G. Scalmani, V. Barone, G. A. Petersson, H. Nakatsuji, X. Li, M. Caricato, A. V. Marenich, J. Bloino, B. G. Janesko, R. Gomperts, B. Mennucci, H. P. Hratchian, J. V. Ortiz, A. F. Izmaylov, J. L. Sonnenberg, D. Williams-Young, F. Ding, F. Lipparini, F. Egidi, J. Goings, B. Peng, A. Petrone, T. Henderson, D. Ranasinghe, V. G. Zakrzewski, J. Gao, N. Rega, G. Zheng, W. Liang, M. Hada, M. Ehara, K. Toyota, R. Fukuda, J. Hasegawa, M. Ishida, T. Nakajima, Y. Honda, O. Kitao, H. Nakai, T. Vreven, K. Throssell, J. A. Montgomery, Jr., J. E. Peralta, F. Ogliaro, M. J. Bearpark, J. J. Heyd, E. N. Brothers, K. N. Kudin, V. N. Staroverov, T. A. Keith, R. Kobayashi, J. Normand, K. Raghavachari, A. P. Rendell, J. C. Burant, S. S. Iyengar, J. Tomasi, M. Cossi, J. M. Millam, M. Klene, C. Adamo, R. Cammi, J. W. Ochterski, R. L. Martin, K. Morokuma, O. Farkas, J. B. Foresman and D. J. Fox, Gaussian 16, Revision B.01, Gaussian, Inc., Wallingford CT, 2016
8. S. Maeda, K. Ohno and K. Morokuma, *Phys. Chem. Chem. Phys.*, 2013, **15**, 3683-3701.
9. S. Maeda, T. Taketsugu and K. Morokuma, *J. Comput. Chem.*, 2014, **35**, 166-173.
10. S. Maeda, Y. Harabuchi, T. Taketsugu and K. Morokuma, *J. Phys. Chem. A*, 2014, **118**, 12050-12058.
11. Y. Harabuchi, T. Taketsugu and S. Maeda, *Chem. Phys. Lett.*, 2017, **674**, 141-145.
12. Y. Harabuchi, T. Taketsugu and S. Maeda, *Phys. Chem. Chem. Phys.*, 2015, **17**, 22561-22565.

13. Y. Harabuchi, T. Taketsugu and S. Maeda, *Chem. Lett.*, 2016, **45**, 940-942.
14. K. Saita, Y. Harabuchi, T. Taketsugu, O. Ishitani and S. Maeda, *Phys. Chem. Chem. Phys.*, 2016, **18**, 17557-17564.
15. Y. Harabuchi, K. Saita and S. Maeda, *Photochem. Photobiol. Sci.*, 2018, **17**, 315-322.
16. K. Saita, M. Takagi, Y. Harabuchi, H. Okada and S. Maeda, *J. Chem. Phys.*, 2018, **149**, 072329.
17. Y. Harabuchi, M. Hatanaka and S. Maeda, *Chem. Phys. Lett.: X*, 2019, **2**, 100007.
18. M. Hatanaka and K. Morokuma, *J. Chem. Theory Comput.*, 2014, **10**, 4184-4188.
19. M. Hatanaka, Y. Hirai, Y. Kitagawa, T. Nakanishi, Y. Hasegawa and K. Morokuma, *Chem. Sci.*, 2017, **8**, 423-429.
20. Y. Shao, M. Head-Gordon and A. I. Krylov, *J. Chem. Phys.*, 2003, **118**, 4807.
21. S. Koseki, M. W. Schmidt and M. S. Gordon, *J. Phys. Chem.*, 1992, **96**, 10768-10772.
22. S. Koseki, M. S. Gordon, M. W. Schmidt and N. Matsunaga, *J. Phys. Chem.*, 1995, **99**, 12764-12772.
23. S. G. Chiodo and N. J. Russo, *Comput. Chem.*, 2009, **30**, 832-839.
24. S. G. Chiodo and M. Leopoldini, *Comput. Phys. Commun.*, 2014, **185**, 676-683.
25. X. Gao, S. Bai, D. Fazzi, T. Niehaus, M. Barbatti and W. Thiel, *J. Chem. Theory Comput.*, 2017, **13**, 515-524.
26. M. J. Frisch, G. W. Trucks, H. B. Schlegel, G. E. Scuseria, M. A. Robb, J. R. Cheeseman, G. Scalmani, V. Barone, B. Mennucci, G. A. Petersson, H. Nakatsuji, M. Caricato, X. Li, H. P. Hratchian, A. F. Izmaylov, J. Bloino, G. Zheng, J. L. Sonnenberg, M. Hada, M. Ehara, K. Toyota, R. Fukuda, J. Hasegawa, M. Ishida, T. Nakajima, Y. Honda, O. Kitao, H. Nakai, T. Vreven, J. A. Montgomery, J. E. Peralta, F. Ogliaro, M. Bearpark, J. J. Heyd, E. Brothers, K. N. Kudin, V. N. Staroverov, T. Keith, R. Kobayashi, J. Normand, K. Raghavachari, A. Rendell, J. C. Burant, S. S. Iyengar, J. Tomasi, M. Cossi, N. Rega, J. M. Millam, M. Klene, J. E. Knox, J. B. Cross, V. Bakken, C. Adamo, J. Jaramillo, R. Gomperts, R. E. Stratmann, O. Yazyev, A. J. Austin, R. Cammi, C. Pomelli, J. W. Ochterski, R. L. Martin, K. Morokuma, V. G. Zakrzewski, G. A. Voth, P. Salvador, J. J. Dannenberg, S. Dapprich, A. D. Daniels, O. Farkas, J. B. Foresman, J. V. Ortiz, J. Cioslowski and D. J. Fox, Gaussian 09, Revision D.01, Gaussian, Inc., Wallingford CT, 2013.
27. J. Finley, P.-Å. Malmqvist, B. O. Roos and L. Serrano-Andre's, *Chem. Phys. Lett.*,

- 1987, **288**, 299-306.
28. B. O. Roos, R. Lindh, P.-Å. Malmqvist, V. Veryazov and P.-O. Widmark, *J. Phys. Chem. A*, 2004, **108**, 2851-2858.
29. B. A. Heß, C. M. Marian, U. Wahlgren and O. Gropen, *Chem. Phys. Lett.*, 1996, **251**, 365-371.
30. P.-Å. Malmqvist, B. O. Roos and B. Schimmelpfennig, *Chem. Phys. Lett.*, 2002, **357**, 230-240.
31. P. Atkins and R. Friedman, *Molecular Quantum Mechanics*, Oxford University Press, Oxford, UK, 4th edn, 2005.

Chapter 3

Electronic states and nonradiative decay involving *trans* → *cis* photoisomerization of methylcinnamate

3-1 Electronic spectra of jet-cooled methylcinnamate

The electronic spectra of jet-cooled methylcinnamate (MC) were measured by using laser induced fluorescence (LIF) or two color-resonance two photon ionization (2C-R2PI) method.

Figure 1 (a) shows the electronic spectrum of jet-cooled MC in 33200-34200 cm^{-1} region measured by LIF method. The spectral feature that there are two electronic transitions is essentially the same as that reported by Ebata *et al.*¹ One is the vibronic bands in the 33300-33600 cm^{-1} region with the band origin at 33300 cm^{-1} (band A), and the other is in the 33700-34100 cm^{-1} region with the band origin at 33740 cm^{-1} (band B). Ebata *et al.* concluded that almost all the vibronic bands belong to the electronic transitions of the *trans/cis* (TC) and *trans/trans* (TT) conformers by UV-UV' hole-burning spectroscopy, however the assignment of the conformer was not done at that time. The optimized structures of the TC and TT conformers in the S_0 state are shown in Figure 2. The notation of first T represents configuration of the $C_2=C_3$ bond, corresponding to *trans* (*E*)

isomer. The notation of second T/C represents the direction between C₂=C₃ and C₄=O₅ bonds (see Figure 2). The TC conformer is more stable than TT by 357 cm⁻¹. Figure 1 (b) and (c) shows the mass-selected 2C-R2PI spectra obtained by fixing the frequency of the ionization laser (ν_2) to 48600 cm⁻¹ (205.75 nm) and 49500 cm⁻¹ (202.0 nm), respectively. These spectra were measured by two nanosecond (ns) time resolved lasers, where the delay time between the pump and probe laser was fixed to almost zero ns. As can be seen in Figure 1 (b), neither band A nor band B is observed, however a new strong band C appears at 33960 cm⁻¹. In Figure 1 (c), on the other hand, all the bands A, B and C appear. These results indicate that an electronic state of the band C is different from those of the bands A and B. Such a state has not been observed in either *p*-HMC or *p*-MMC.

2-8

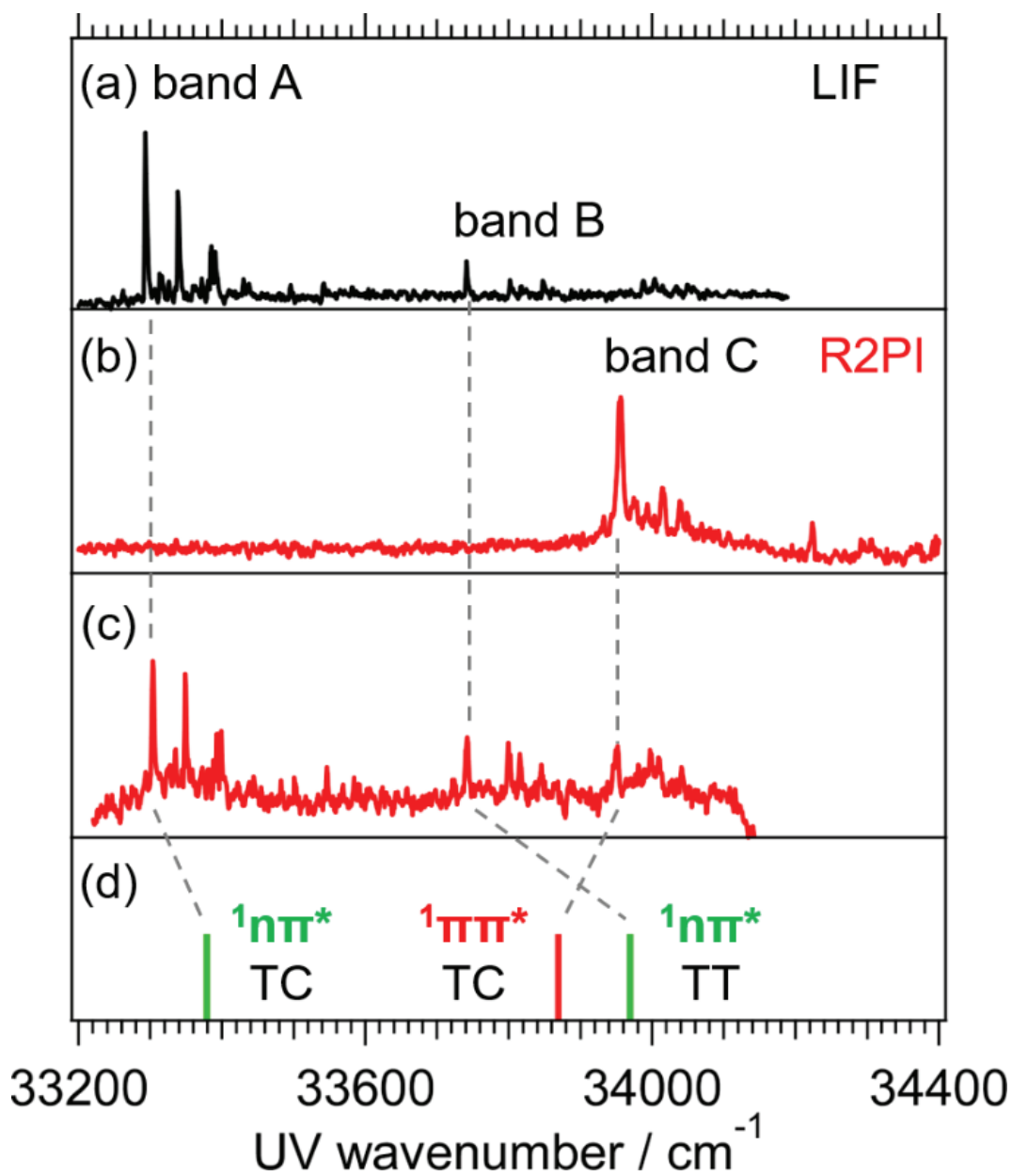


Figure 1 Electronic spectra of jet-cooled MC measured by (a) LIF and 2C-R2PI method, fixing the ν_2 to (b) 48600 cm^{-1} (205.75 nm) and (c) 49500 cm^{-1} (202.0 nm). (d) ZPE collected adiabatic energies calculated at the $\omega\text{B97XD/6-311G(d,p)}$ level of theory scaled with 0.9725.

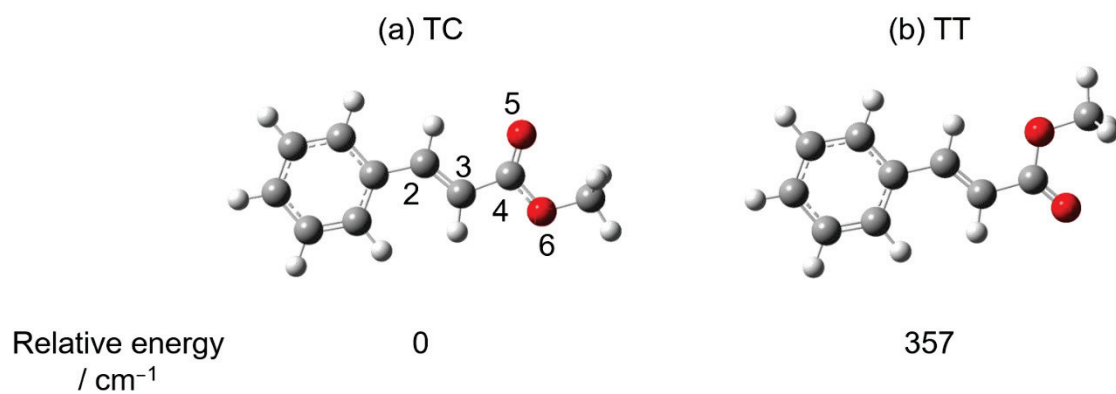


Figure 2 Optimized structures of the (a) TC and (b) TT conformers in the S_0 state calculated at the $\omega\text{B97XD}/6\text{-}311\text{G(d,p)}$ level, Their relative energies are also shown in unit of cm^{-1} .

3-2 Assignment of conformers and electronic transitions

For assignment of the electronic state and conformer, the ionization energies of bands A, B and C were measured by two ns lasers and compared with the calculated values at the ω B97XD/6-311G(d,p) or Symmetry Adapted Cluster/Configuration Interaction calculation (SAC-CI)/6-311G(d) Lv5 level.

Figure 3 (a) shows the ionization efficiency curve from band C. Here, frequency of the pump laser (ν_1) was fixed to band C (33960 cm^{-1}), and the ν_2 was scanned. In Figure 3 (a), an ionization threshold is observed at $\nu_2 = 35130 \text{ cm}^{-1}$, corresponding to the ionization energy of 69090 cm^{-1} . Figure 3 (b) shows the ionization efficiency curves from bands A (black plots) and B (red plots). An ionization threshold is observed at $\nu_2 = 48280 \text{ cm}^{-1}$, corresponding to the ionization energy of 81610 cm^{-1} for band A and 82020 cm^{-1} for band B. This threshold is much higher than that of band C as shown in Figure 3 (c). The result means that bands A and B are correlated to the excited state of the ion. Thus, the adiabatic ionization energies of the $D_0 (\pi^{-1})$, $D_1 (\pi^{-1})$ and $D_2 (n^{-1})$ states were calculated at the SAC-CI-NV/6-311G(d,p) Lv5 level. The calculated energy of the $D_0 (\pi^{-1})$ state is 67107 cm^{-1} and agrees with the obtained ionization energy from band C (69090 cm^{-1}). The calculated energy gap between the $D_2 (n^{-1})$ and $D_0 (\pi^{-1})$ states is 10767 cm^{-1} and agrees with the ionization energy difference between band A and C (12520 cm^{-1}). Thus, the electronic state corresponding to band C is ionized to the $D_0 (\pi^{-1})$ state and bands A and B to the $D_2 (n^{-1})$ state.

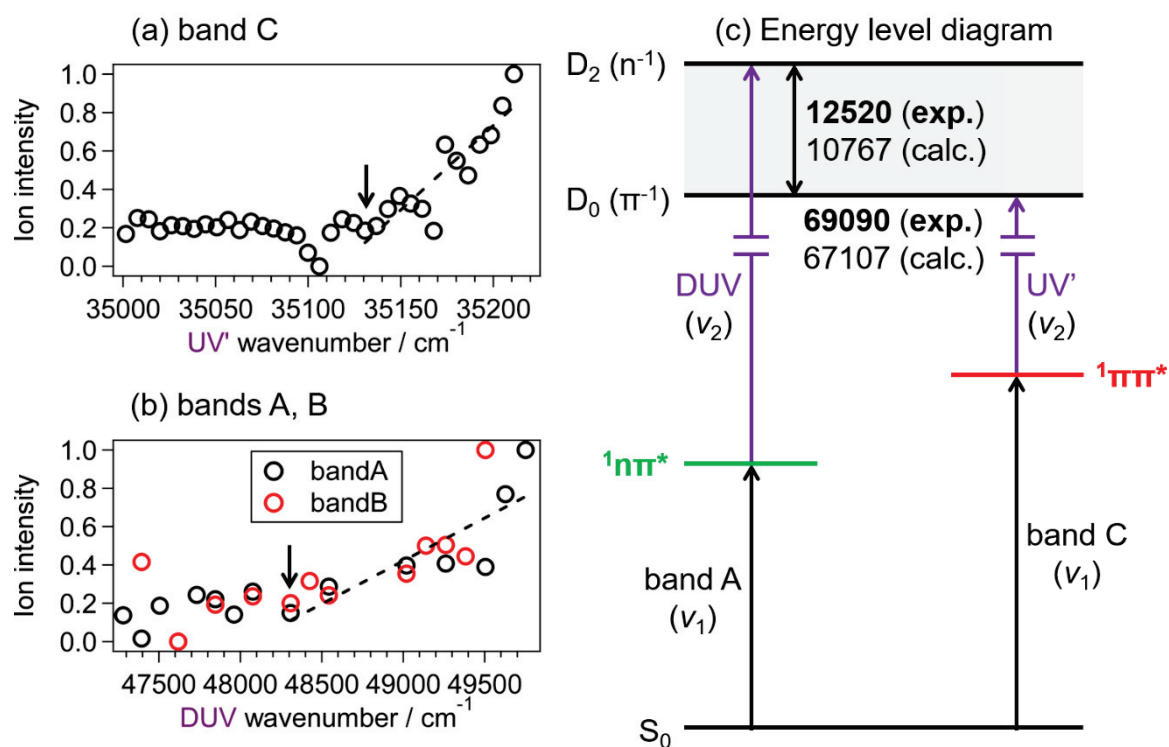


Figure 3 Ionization efficiency curves from (a) band C and (b) bands A and B. The arrows indicate the ionization threshold. (c) Energy level diagram of all bands (A, B and C) and their ionic states in unit of cm⁻¹.

Table 1 Observed electronic transitions, calculated non-scaled ZPE corrected adiabatic excitation energies in unit of cm^{-1} and characters of the two lowest singlet excited states of MC (TC), *p*-HMC (*anti* TC) and *p*-MMC (*anti* TC).

	MC		<i>p</i> -HMC		<i>p</i> -MMC		
	State	Energy / cm^{-1}	ΔE	Energy / cm^{-1}	ΔE	Energy / cm^{-1}	ΔE
Obs.	S ₁	33300 ($n\pi^*$)		32710 ($\pi\pi^*$)		32667 ($\pi\pi^*$)	
	S ₂	33960 ($\pi\pi^*$)	660	-	-	-	-
ω B97XD/	S ₁	34323 ($n\pi^*$)		33697 ($\pi\pi^*$)		33368 ($\pi\pi^*$)	
6-311G(d,p)	S ₂	34827 ($\pi\pi^*$)	504	34692 ($n\pi^*$)	995	34743 ($n\pi^*$)	1375
SAC-CI/	S ₁	35765 ($n\pi^*$)					
6-311G(d)	S ₂	37621 ($\pi\pi^*$)	1856				

For secure assignment, the geometric optimization and evaluation of the adiabatic energies of the $^1n\pi^*$ and $^1\pi\pi^*$ states were performed for the TC conformer at the ω B97XD/6-311G(d,p) and SAC-CI/6-311G(d) Lv5 levels of theory. The obtained stable structures in the $^1n\pi^*$ and $^1\pi\pi^*$ states are planar. The remarkable differences between them are C₄=O₅ bond length and O₅-C₄-O₆ angle (see Figure 2). The bond length in the $^1n\pi^*$ and $^1\pi\pi^*$ state is 1.31 and 1.22 Å, respectively. The angle in the $^1n\pi^*$ and $^1\pi\pi^*$ state is 115 and 123°, respectively. The calculated zero-point energy (ZPE) corrected adiabatic energies and the

energies of the observed 0-0 band are listed in Table 1. As can be seen in the table, both theoretical calculations predict that the character of the lowest singlet excited state (S_1) and second (S_2) is $^1n\pi^*$ and $^1\pi\pi^*$, respectively. Thus, it is quite possible that bands A and B are assigned to the $^1n\pi^*$ state of the two conformers, and band C to the $^1\pi\pi^*$ state. The scaled adiabatic excitation energies of the $^1n\pi^*$ and $^1\pi\pi^*$ states are shown in Figure 1 (d) as sticks. As shown in the figure, the band C corresponds to the origin of the $^1\pi\pi^*$ state of the TC conformer, and the band A and B corresponds to the $^1n\pi^*$ state of the TC and TT conformer, respectively. It should be noted that this study is the first case of the direct observation of the $^1n\pi^*$ state among the cinnamate family.

Although it is expected that two $^1\pi\pi^*$ transitions of the TC and TT conformers will appear, only one transition is observed for the $^1\pi\pi^*$ (band C). In order to investigate the reason of the absence, the geometry optimization of the $^1\pi\pi^*$ and $^1n\pi^*$ states was further performed for the TT conformer. However, a stable structure of the $^1\pi\pi^*$ state was not found at the ω B97XD/6-311G(d,p) and SAC-CI/6-311G(d) level of theory near its Franck-Condon region. Actually, the calculation at the ω B97XD/6-311G(d,p) level shows that the $^1\pi\pi^*$ state of the TT conformer is unstable and collapses into a conical intersection having a $C_2=C_3$ (see Figure 2) twisted structure without experiencing any barrier. This is consistent with the experimental result that only band C assigned to the $^1\pi\pi^*$ state for TC conformer is observed in the 2C-R2PI spectra. In the Figure 1 (b), a weak band appears at 34210 cm^{-1} . It is not clear whether this band is the vibronic band

belonging to band C or the band origin of the TT conformer. Another possible reason for the absence of the another ${}^1\pi\pi^*$ state is the short lifetime. As will be discussed later, the lifetime of band C is equal to or shorter than 10 ps. If the band has a shorter lifetime, its intensity will be very weak.

The adiabatic ${}^1n\pi^*$ and ${}^1\pi\pi^*$ energies of the *anti*-TC conformer of *p*-HMC as well as *p*-MMC are also listed in Table 1. In both *p*-HMC and *p*-MMC, *anti*-TC is the most stable conformer in the S_0 state.^{2,4} The calculated results in this table show that the order of the energies between the ${}^1n\pi^*$ and ${}^1\pi\pi^*$ state of MC is opposite to that of *p*-HMC and *p*-MMC. Actually, in *p*-HMC and *p*-MMC, only the ${}^1\pi\pi^*$ state is observed as the S_1 state,²⁻⁸ due to the fact that the weak S_0 - S_2 (${}^1n\pi^*$) absorption is buried by the strong S_0 - S_1 (${}^1\pi\pi^*$) absorption in those molecules. It clearly shows that the substitution to the phenyl ring effects on the electronic states. The energy of the ${}^1\pi\pi^*$ state becomes lower upon substitution, while that of ${}^1n\pi^*$ remains the same. This is the reason why the ${}^1n\pi^*$ state is directly observed in lower energy region than the ${}^1\pi\pi^*$ state in electronic spectra of MC. The reason of energetic modulation of these two states will be discussed in Chapter 4.

3-3 Lifetime measurement and nonradiative decay process

For the investigation of the nonradiative decay (NRD) process, the lifetime of the S_1 ($^1n\pi^*$) and S_2 ($^1\pi\pi^*$) states were measured by various spectroscopic techniques.

Figure 4 shows the fluorescence decay curves at (a) band A (0-0), (b) band A + 46 cm^{-1} , (c) band A + 92 cm^{-1} and (d) band B. The red and gray plots represent the signals due to fluorescence and scatters of UV light, respectively. The black curves correspond to deconvoluted curve with laser pulse width (5 ns). The lifetime at the 0-0 band (band A) was measured as 8.5 ns, however the lifetime becomes too short to be measured at above 33400 cm^{-1} region. This result indicates that the $^1n\pi^* \rightarrow$ triplet intersystem crossing (ISC) channel is open even at the low excess energy.

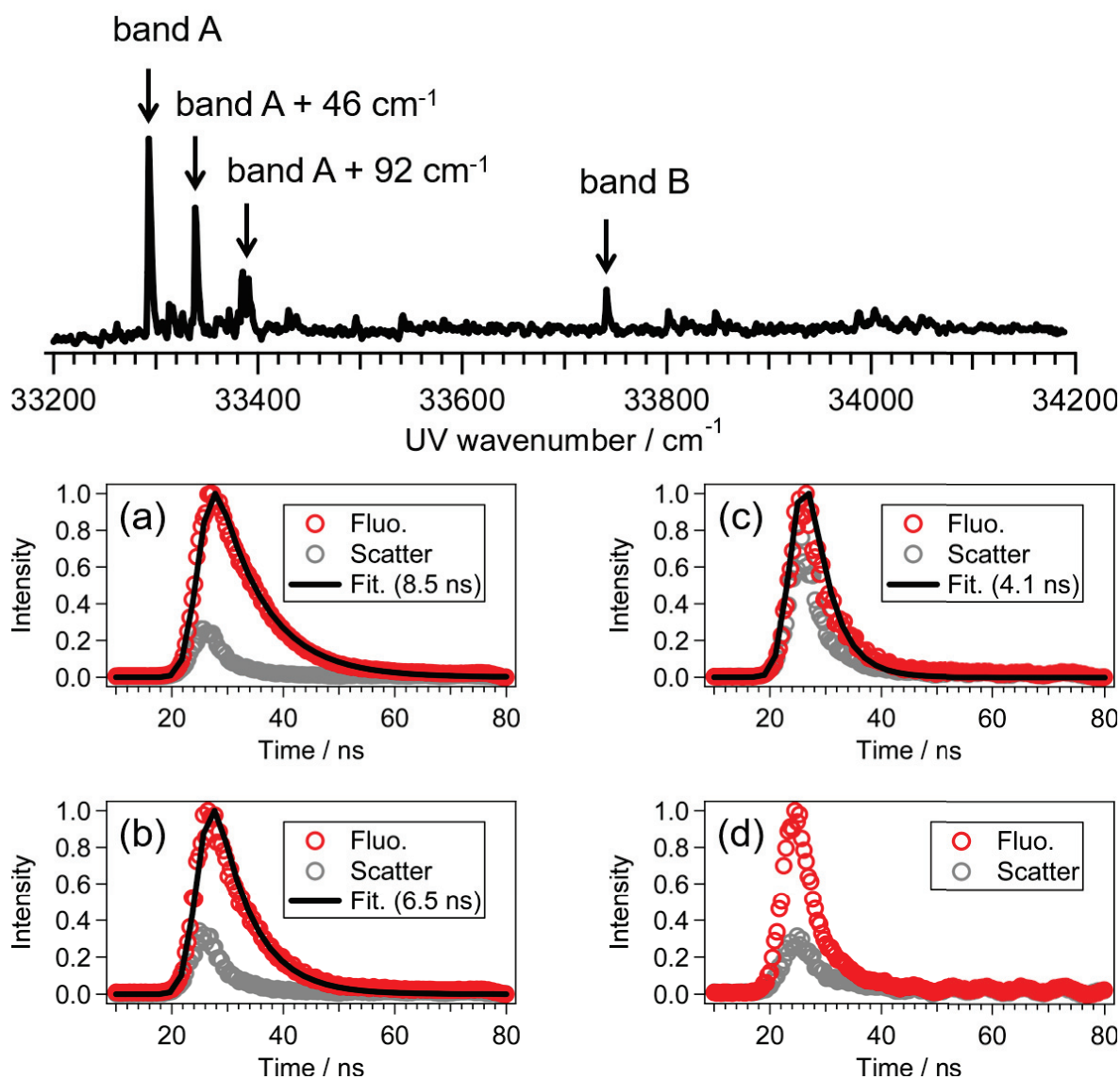


Figure 4 (Upper) LIF excitation spectrum of jet-cooled MC. Fluorescence decay curves at (a) band A (0-0), (b) band A + 46 cm^{-1} , (c) band A + 92 cm^{-1} and (d) band B. The red and gray plots represent the signals due to fluorescence and scatters of UV light, respectively. The black curves correspond to deconvoluted curve with laser pulse width (5 ns).

Figure 5 (a) shows the energy level diagram in unit of cm^{-1} and NRD process from the S_2 ($^1\pi\pi^*$). Figure 5 (b) shows the time profile of band C ($^1\pi\pi^*$) obtained by picosecond (ps) UV-UV' pump-probe measurement. Here, the ν_1 and ν_2 was fixed to 33960 cm^{-1} (band C) and 41140 cm^{-1} (243.1 nm), respectively. The red plots are the observed pump-probe ion signal, and the black curve is the convoluted decay curve fitted by assuming a single exponential decay of $\tau = 10$ ps with a laser pulse width (12 ps). This lifetime is the shortest one that can be obtained with our ps laser system, thus the true lifetime may be shorter than 10 ps. Recently, the $^1\pi\pi^*$ lifetime was measured as 4.5 ps by Stavros and co-workers.⁹ This short lifetime means that the $^1\pi\pi^*$ lifetime can be controlled mainly by internal conversion (IC) to the $^1n\pi^*$ state.

Figure 5 (c) shows the time profile obtained by ns UV-DUV pump-probe measurement. Here, the ν_1 and ν_2 was fixed to 33960 cm^{-1} (band C) and 49260 cm^{-1} (203.0 nm), respectively. The deconvolution of the decay curve fitted by a single exponential decay gives a lifetime of $\tau = 20$ ns (black curve). The $^1n\pi^*$ lifetime was measured as 8.5 ns, therefore this long-lived state is thought to be different from the $^1n\pi^*$ state and transiently generated upon excitation to the $^1\pi\pi^*$ state.

Figure 5 (d) shows the ionization efficiency curve of the transient state obtained by ns UV-DUV pump-probe measurement. Here, the ν_1 was fixed to 33960 cm^{-1} (band C) and the ν_2 was scanned, with a delay time (Δt) of 15 ns. The ion intensity gradually increases at 47300 cm^{-1} . By assuming that the transient

state can be ionized to $D_0 (\pi^{-1})$ (69090 cm^{-1}), the energy of the transient state is determined to be 21790 cm^{-1} . Herkstroeter and Farid reported that the T_1 energy of MC is 54.8 kcal/mol (19170 cm^{-1}) by T-T energy transfer in solution.¹⁰ The value agrees with that of the present transient state.

Figure 5 (e) shows the optimized T_1 (${}^3\pi\pi^*$) structure calculated at the $\omega\text{B97XD/6-311G(d,p)}$ level. The dihedral angle between C_1-C_2 and C_3-C_4 (see Figure 2) in the T_1 structure is rotated by 89° , suggesting the transient structure between *trans* (*E*) and *cis* (*Z*) isomers. Although the calculated energy value (17799 cm^{-1}) is a little bit smaller than that of the experimental one, the transient state was assigned to the T_1 (${}^3\pi\pi^*$).

Figure 6 (a)-(e) show the time profiles obtained by ns UV-DUV pump-probe measurement with the several ν_2 values (49260 , 48780 , 48310 , 47620 and 46510 cm^{-1}). It is found that in Figure 6 (a)-(d), the slow component fitted by 20 ns, corresponding to the T_1 state is seen, however its intensity becomes smaller with lowering the energy of the ionization laser (ν_2). In Figure 6 (e), this slow component disappears, because the ν_2 is not high enough to ionize the T_1 state. The fast component corresponds to the decay of the ${}^1\pi\pi^*$ state. This means that only decay profile of the T_1 (${}^3\pi\pi^*$) can be obtained as slow component by our ns laser system. From these results, it is concluded that the NRD route from S_2 (${}^1\pi\pi^*$) is described as “ S_2 (${}^1\pi\pi^*$) \rightarrow S_1 (${}^1n\pi^*$) \rightarrow T_1 (${}^3\pi\pi^*$) \rightarrow S_0 (*trans* or *cis*)”.

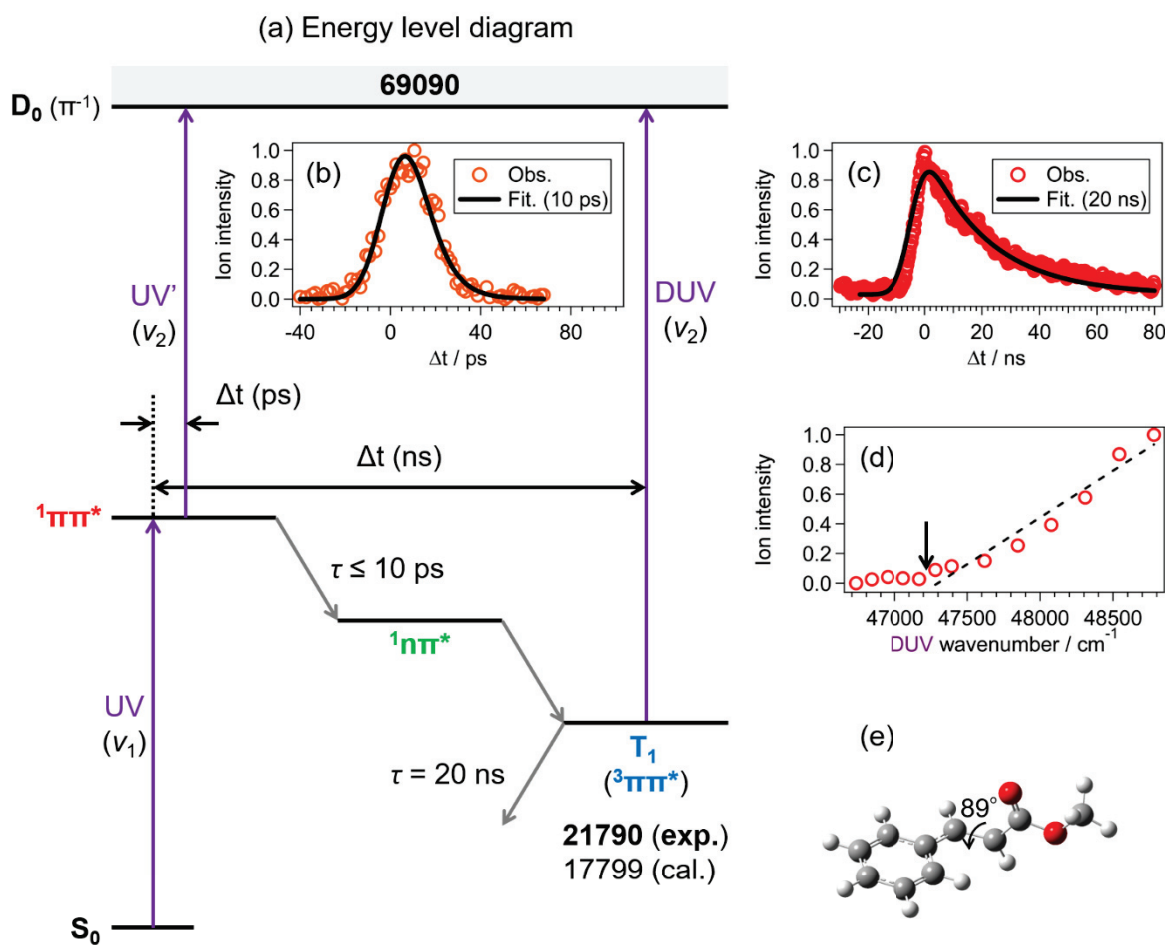


Figure 5 (a) Energy level diagram in unit of cm^{-1} and NRD process from the S_2 ($1\pi\pi^*$). (b) Time profile of the $1\pi\pi^*$ state obtained by ps UV-UV' pump-probe measurement. The black curve is deconvoluted curve with laser pulse width (12 ps). (c) Time profile and (d) ionization efficiency curve of the T_1 ($3\pi\pi^*$) obtained by ns UV-DUV pump-probe measurement. The black curve in (c) is deconvoluted curve with laser pulse width (5 ns). The arrow in (d) indicates the ionization threshold. (e) Optimized T_1 ($3\pi\pi^*$) structure calculated at the $\omega\text{B97XD}/6\text{-}311\text{G(d,p)}$ level

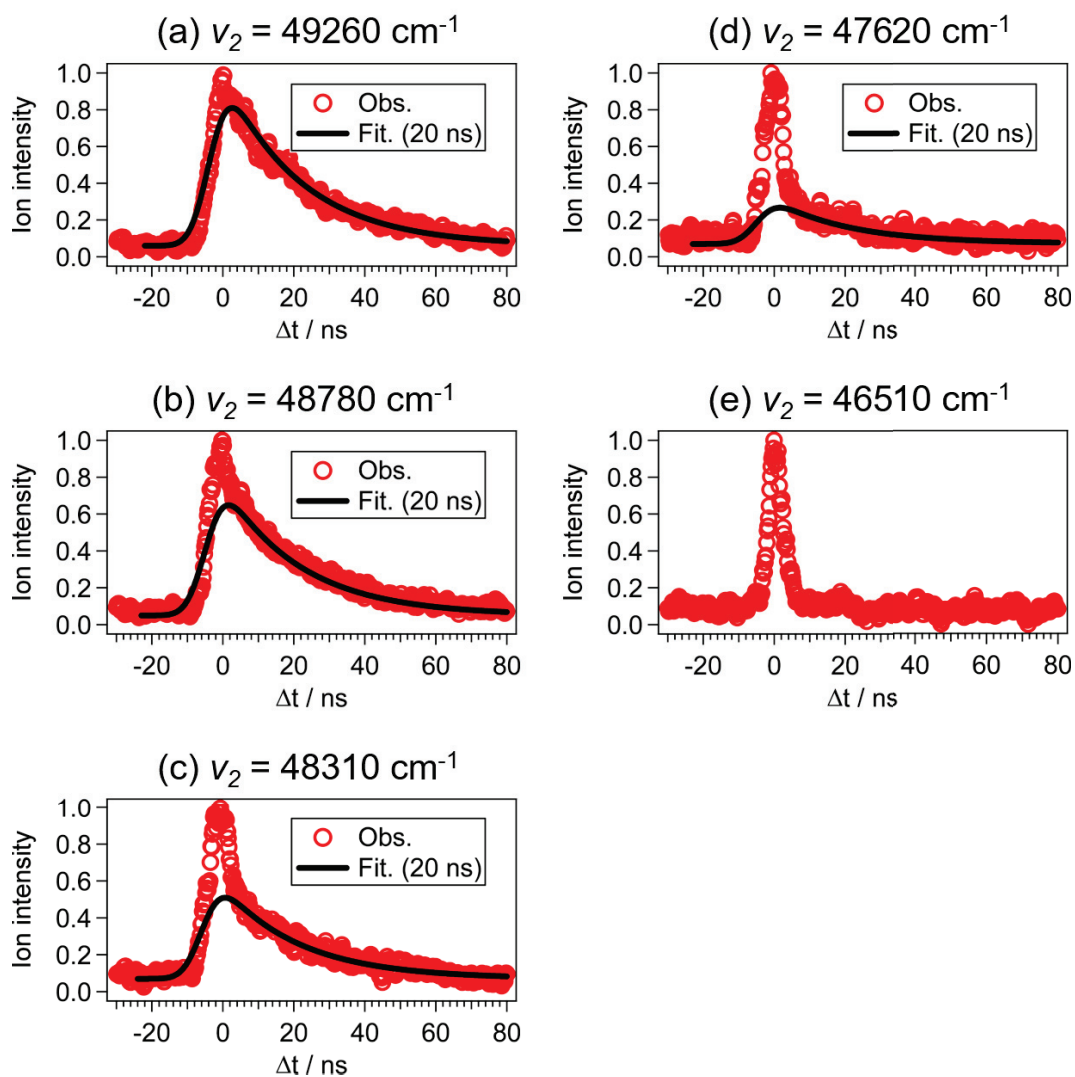


Figure 6 Time profiles of the transient state (T_1) obtained by ns UV-DUV pump-probe measurement. Here, the ν_2 was fixed to (a) 49260, (b) 48780, (c) 48310, (d) 47620 and (e) 46510 cm^{-1} . The black curves are deconvoluted curves with laser pulse width (5 ns).

3-4 Photoproduct analysis upon UV irradiation

For identifying the photoproduct upon UV irradiation, cold matrix-isolation FTIR spectroscopy was performed. The obtained difference IR spectrum before and after UV irradiation was compared with the calculated ones between *trans* (*E*) and *cis* (*Z*) isomer at the B3LYP/6-311++G(d,p) level.

Figure 7 (a) represents observed IR spectrum of MC deposited on the cold Ne matrix before UV irradiation. In the IR spectrum, strong peak can be assigned to the C-O stretching mode of the ester group appears at 1176 cm^{-1} . In addition, relatively strong peak assigned to the C=C and C=O stretching mode appears at 1646 and 1740 cm^{-1} , respectively. Figure 7 (b) and (c) represents calculated IR spectrum of TC and TT conformer, respectively at the B3LYP/6-311++G(d,p) level. Figure 7 (d) represents sum of the calculated IR spectrum of the TC and TT conformers assuming a Boltzmann distribution at the vaporized temperature (302 K). Here, these calculated spectra were scaled by 0.994. It is found that the calculated spectrum (Figure 7 (d)) well reproduces the observed one (Figure 7 (a)).

Figure 7 (e) represents observed difference IR spectrum of the matrix-isolated MC before and after UV irradiation at $\lambda_{UV} > 300\text{ nm}$. Positive and negative peaks indicate generation of the photoproduct and depletion of the reactant, respectively. Figure 7 (f) and (g) represents calculated difference IR spectra between TC and *cis/cis* (CC) conformer, TC and *cis/trans* (CT) conformer, respectively. The CC conformer is more stable than the CT conformer by 802 cm^{-1} . The observed vibration at 1640 cm^{-1} in Figure 7 (e) highlighted by yellow line

was assigned to the propenyl C=C stretching of the CC conformer. Therefore, it is concluded that the *trans* → *cis* photoisomerization occurs after UV irradiation.

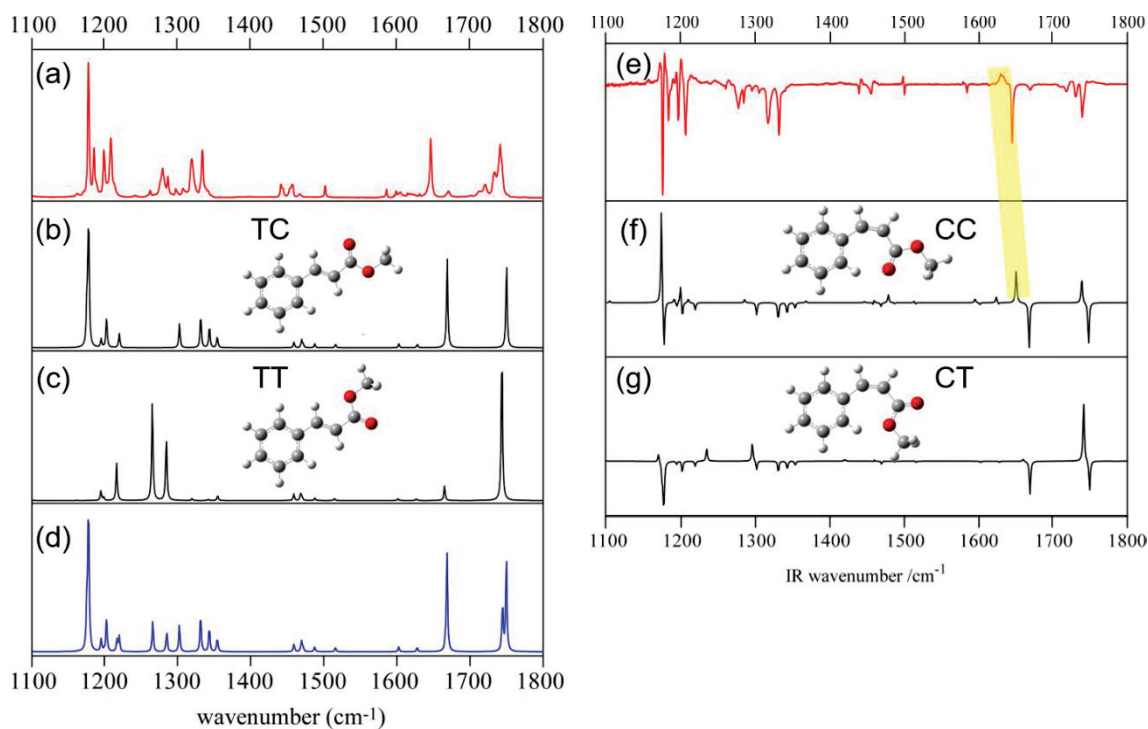


Figure 7 (a) IR spectrum of MC deposited on the cold Ne matrix before UV irradiation. Calculated IR spectrum of the (b) TC and (c) TT conformer. (d) The sum of the calculated IR spectrum of the TC and TT conformers. (e) Difference IR spectrum of the matrix-isolated MC before and after UV irradiation. Calculated difference IR spectra between (f) TC and CC conformer, (g) TC and CT conformer.

3-5 Systematic search for the dominant NRD/photoisomerization route

The NRD/photoisomerization route was explored by artificial force induced reaction method with (time-dependent) density functional theory (AFIR/TD-DFT) calculation at the ω B97XD/6-311G(d,p) level for secure understanding the experimental results.

Figure 8 shows the energy diagram of the excited states and the photoisomerization route starting from the $^1\pi\pi^*$ minima (EQ 1) to the T_1 ($^3\pi\pi^*$) minima (EQ 7 and EQ 8). The values with ZPE correction are also shown in parentheses. The crosses in Figure 8 indicate minimum energy conical intersections (MECIs) or minimum energy seam of crossings (MESXs). Hereafter, the dihedral angles of C-C=C-C and C-C-O-Me is defined as the twisting angles around C=C bond and methoxy group, respectively. According to this definition, the twisting angles around C=C bond for *trans* (*E*) and *cis* (*Z*) isomers is 180° and 0° , respectively.

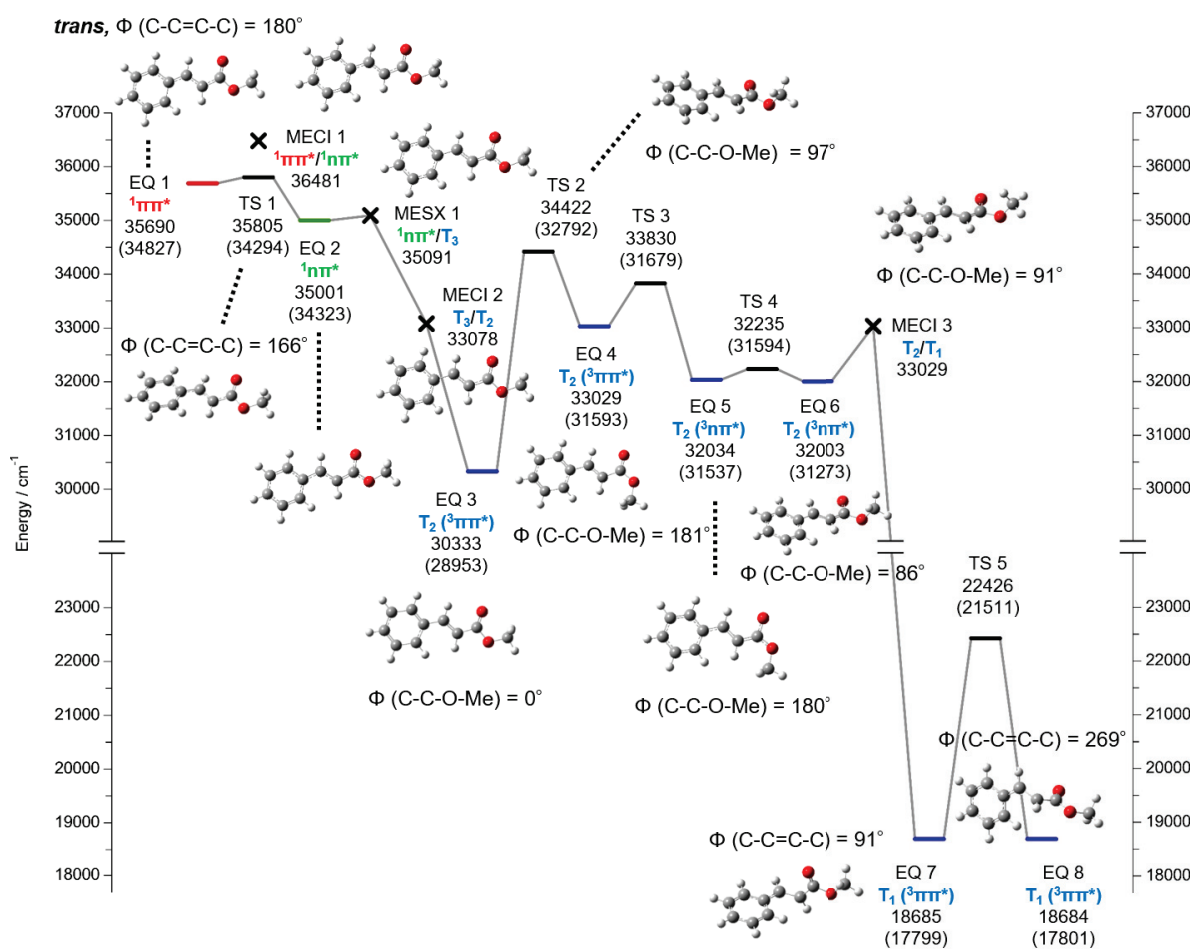


Figure 8 Energy diagram along the decay route of the photoisomerization for MC from the *trans* $^1\pi\pi^*$ minimum (EQ 1) to the T_1 ($^3\pi\pi^*$) minima (EQ 7 and EQ 8) calculated at the ω B97XD/6-311G(d,p) level. The values in parentheses are the ZPE corrected ones. The angles in the structures are the tilting angle of the propenyl C=C bond with respect to the planar structure (*trans* form). The crosses indicate minimum energy conical intersections (MECIs) or minimum energy seam of crossings (MESXs).

The first IC from the $^1\pi\pi^*$ (EQ 1) to $^1n\pi^*$ (EQ 2) state immediately occurs through the nonplanar avoided crossing-type transition state (TS 1) at 35805 cm^{-1} . This IC is a barrier-less process since the energy of TS 1 with ZPE correction (34294 cm^{-1}) is lower than that of EQ 1 (34827 cm^{-1}). This explains very well the observed very short lifetime of the $^1\pi\pi^*$ state in the gas phase (4.5 ps).⁹ The planar $^1\pi\pi^*/^1n\pi^*$ MECI 1 was found at 36481 cm^{-1} . MECI 1 is energetically higher than that *via* TS 1 by 676 cm^{-1} , thus is not much involved in this IC process.

MC next undergoes ISC to the T_3 ($^3\pi\pi^*$) *via* MESX 1 found at 35091 cm^{-1} near EQ 2. Several low-lying MESXs between singlet ($^1\pi\pi^*$, $^1n\pi^*$) and triplet (T_2 , T_3) states as displayed in Figure 9. In addition, calculated spin-orbit coupling (SOC) values at these MESXs are listed in Table 2. It is found that the energy of MESX 1 is lower than that of other MESXs, and the calculated SOC value at MESX 1 (24 cm^{-1}) is large enough for ISC to occur *via* MESX 1. MESXs 2 and 3 have very small SOC values due to the El-Sayed's rule¹¹ and they have minor contributions to the triplet mediated NRD route. MC in the T_3 state immediately decays to the T_2 ($^3\pi\pi^*$) by IC *via* MECI 2, since the intrinsic reaction coordinate (IRC) calculation from MESX 1 to the T_3 state directly reaches MECI 2.

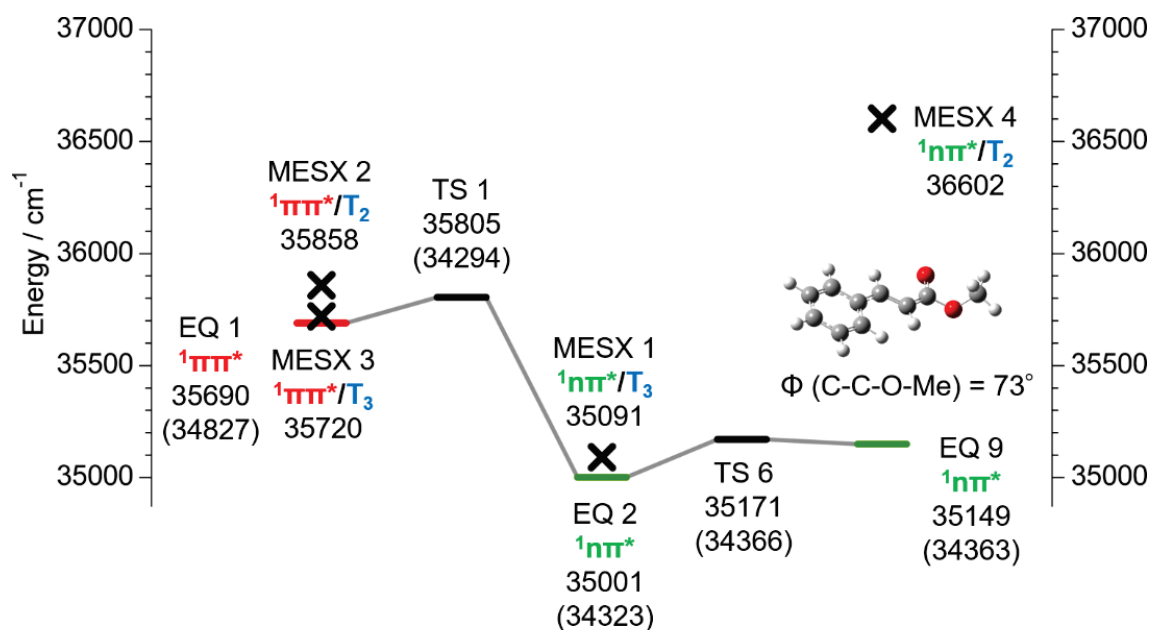


Figure 9 Energy diagram of the EQs, TSs and MESXs between the singlet ($^1\pi\pi^*$, $^1n\pi^*$) and triplet (T_2 , T_3) state of MC. The values in parentheses are the ZPE corrected ones. MESXs are indicated as crosses.

Table 2 SOC values in unit of cm^{-1} at MESXs calculated at the $\omega\text{B97XD}/6\text{-}311\text{G(d,p)}$ level.

Structure	Character	SOC value / cm^{-1}
MESX 2	$^1\pi\pi^*/^3\pi\pi^*$ (T_2)	0.07443
MESX 3	$^1\pi\pi^*/^3\pi\pi^*$ (T_3)	0.2572
MESX 1	$^1n\pi^*/^3\pi\pi^*$ (T_3)	24.09
MESX 4	$^1n\pi^*/^3\pi\pi^*$ (T_2)	26.37

After the IC to the T_2 ($^3\pi\pi^*$), the OMe group starts tilting. This OMe tilting changes the character of the T_2 state from $^3\pi\pi^*$ to $^3n\pi^*$ by passing through an avoided crossing-type TS 3, the same as the IC from the $^1\pi\pi^*$ to $^1n\pi^*$ state (TS 1) discussed above. The OMe torsion further triggers IC to the T_1 ($^3\pi\pi^*$). MC reaches the C=C twisted T_1 structure (EQ 7). This multistep IC process from the T_3 to T_1 state completes within a few ns according to our ns UV-DUV pump-probe measurement, where only EQ 7 (T_1) was experimentally detected. The 0-0 energy level of EQ 7 is 17799 cm^{-1} , which reasonably agrees with the experimental value (21790 cm^{-1}). The C=C bond in EQ 7 is twisted by 91° , and EQ 7 looks like the TS between *trans* and *cis* isomers. MC at EQ 7 has large excess energy (17028 cm^{-1}), therefore it can further isomerize to another T_1 minima (EQ 8) through TS 5. The C=C bond in EQ 8 is twisted by 269° .

It is found that MECI 3 is the most preferable T_2/T_1 MECI for $T_2 \rightarrow T_1$ IC. Despite of the high energy barrier for OMe tilting (TS 2, 3839 cm^{-1}), this $T_2 \rightarrow T_1$ IC process is possible due to the large excess energy at the T_2 EQ 3 (5874 cm^{-1}), assuming the 0-0 transition from the S_0 state to EQ 1. The reaction rate for the rate-determining step from EQ 3 to EQ 4 was calculated to be $1.44 \times 10^7\text{ s}^{-1}$, corresponding to time constant of 69.4 ns by using Rice-Ramsperger-Kassel-Marcus (RRKM) theory¹² and this long time constant suggests a multiple reaction pathway picture for $T_2 \rightarrow T_1$ IC process discussed below.

The other $T_2 \rightarrow T_1$ IC channels apart from the route *via* MECI 3 was also investigated. Other MECIs between the T_2 and T_1 state were also explored. The

resultant nine MECIs are summarized in Figure 10. It is found that MECI 4 is basically the mirror inversion structure of MECI 3. The small deviations in energy among these mirror inversion structures may be originated from the numerical errors in the TD-DFT calculations and/or geometry optimization.

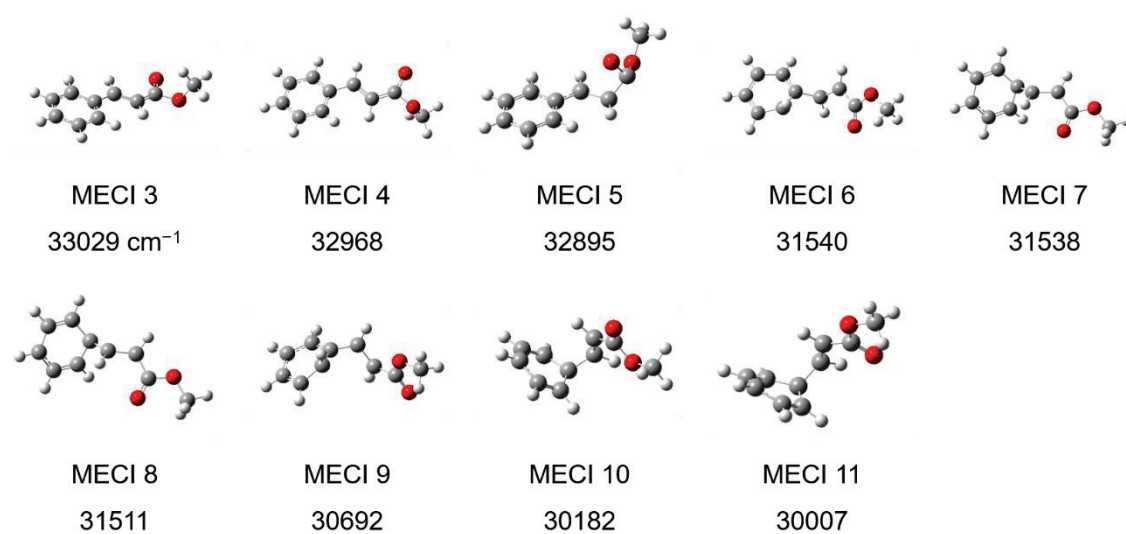


Figure 10 Optimized structures of MECIs (T_2/T_1) in the region around 30000-33000 cm^{-1} obtained by AFIR/TD-DFT calculation at $\omega\text{B97XD}/6\text{-}311\text{G}(\text{d},\text{p})$ level. The relative energies are also shown in unit of cm^{-1} .

It was also tried to search intermediates and TSs between the other low-lying T_2/T_1 MECI and other EQs in the T_2 and T_1 states by using meta-IRC and AFIR methods. Figure 11 shows the $T_2 \rightarrow T_1$ IC route from EQ 10 (T_2) to EQ 7 (T_1) via MECI 4. The EQ 10 is mirror inversion structure of the EQ 6. The structural change on the T_2 state from EQ 3 to MECI 4 is essentially same as those to MECI 3, since MC at EQ 3 belongs to C_s point group. After the $T_2 \rightarrow T_1$ IC via MECI 4, MC reaches EQ 8. EQ 8 and EQ 7 co-exist due to large excess energy in the T_1 state. The search for other $T_2 \rightarrow T_1$ IC routes via MECI 5-11 in Figure 10 were unsuccessful due to serious SCF convergence problems on the TD-DFT calculations.

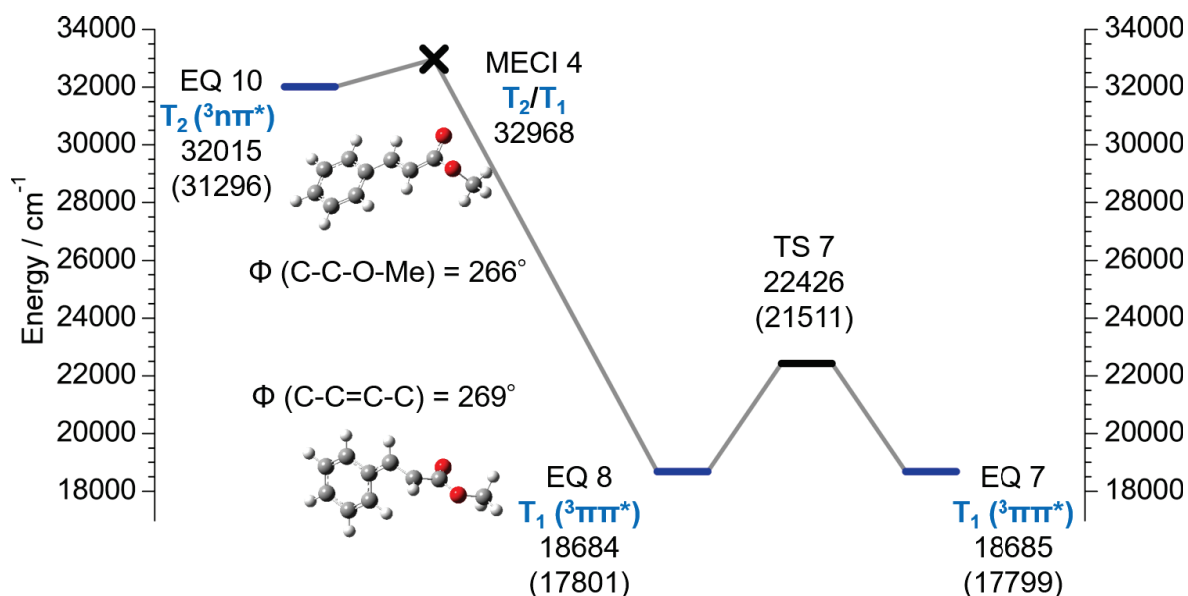


Figure 11 The $T_2 \rightarrow T_1$ pathway from EQ 10 to EQ 7 which competes with the main pathway of Figure 8. The values in parentheses are the ZPE corrected ones.

The final step of the multistep NRD is the ISC from the T_1 (${}^3\pi\pi^*$) to S_0 state. Two low-lying T_1/S_0 MESXs, MESX 5 and 6, were found as shown in Figure 12. The calculated SOC value of MESX 5 and 6 at the [10e,9o]-MS-CASPT2/ANO-RCC-VTZP level of theory is 0.07 and 0.38 cm^{-1} , respectively. According to our meta-IRC analysis from these two MESXs, formation of *trans*- S_0 isomer *via* the lower-lying MESX 5 seems to be energetically more favorable than that of *cis* isomer (EQ 11) *via* the higher lying MESX 6.

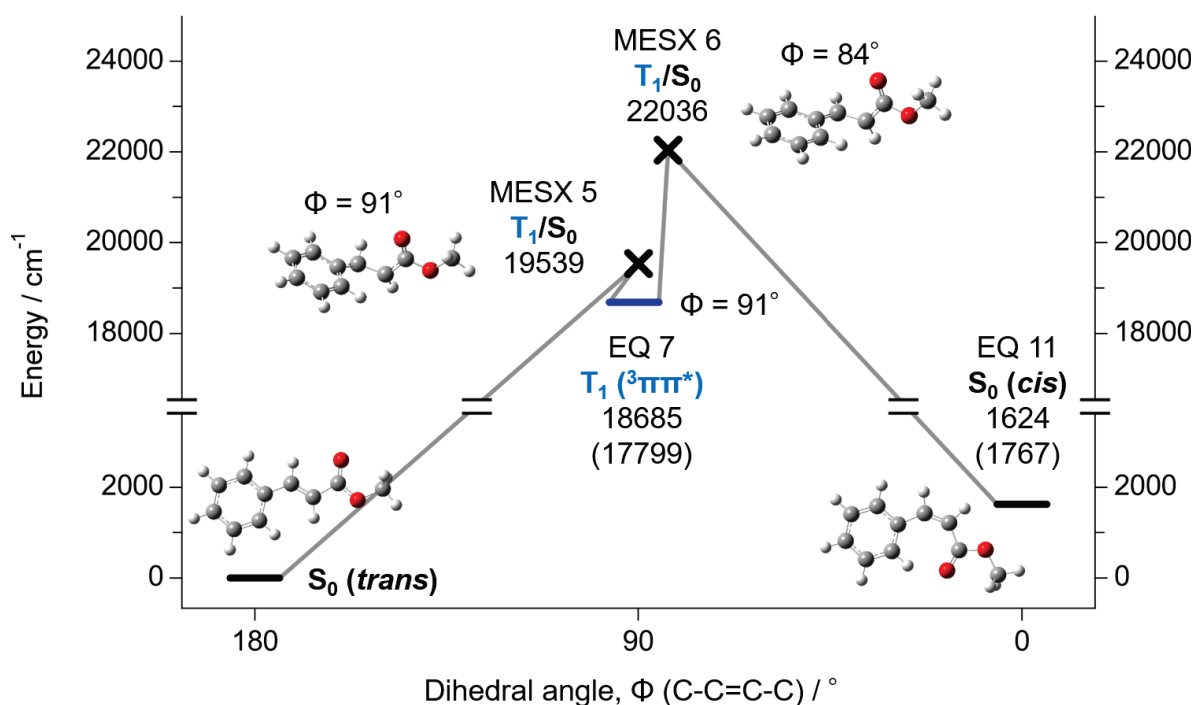


Figure 12 Energy diagram and decay routes of isomerization to *cis* (EQ 11) and going back to *trans* isomer from EQ 7 (T_1 , ${}^3\pi\pi^*$). The x-axis represents the dihedral angle around the C=C bond. The angle of *trans* isomer is defined as 180° .

The ${}^1\pi\pi^*$ state decays to ${}^1n\pi^*$ (EQ 2) in less than 10 ps according to experimental studies. It is concluded that the transient state (T_1) is produced faster than time resolution of ns UV-DUV pump-probe measurement (6-7 ns). Thus, the decay process from EQ 1 to EQ 7 involving ISC *via* MESX 1 occurs within a few ns. The calculated SOC values of T_1/S_0 MESXs 5 and 6 (0.07 and 0.38 cm^{-1} , respectively) are approximately 100 times smaller than that of ${}^1n\pi^*/{}^3\pi\pi^*$ MESX 1 (24 cm^{-1}). Thus, the ISC from the T_1 to S_0 state is much slower and EQs 7 and 8 can be observed by ns UV-DUV pump-probe measurements.

In the gas-phase condition such as in a supersonic beam, MC in the T_1 state has large excess energy of 17028 cm^{-1} . This large excess energy can drive MC to (i) ISC *via* non-IRC pathways (*cis* formation *via* MESX 5 and *trans* formation *via* MESX 6), (ii) conformation change in the T_1 state, and (iii) *trans* \rightarrow *cis* and *cis* \rightarrow *trans* isomerization in the S_0 state after the ISC. However, in solution the collisional cooling will interrupt the isomerization process. For the determination of the branching ratio of *trans/cis* isomerization *via* multistep ISC, a detailed nonadiabatic kinetics study including these three effects is essential.

It was also investigated that another multistep ISC pathway where MC directly undergoes ISC from the ${}^1\pi\pi^*$ to triplet states as suggested by Moon *et al.*¹³ and by Yamazaki *et al.*¹⁴ in *p*-MMC. However, it is found that this pathway plays a very minor role for the decay from the ${}^1\pi\pi^*$ state in the case of MC. The character of the all low-lying MESXs around EQ 1 is ${}^1\pi\pi^*/{}^3\pi\pi^*$, where ISC is not preferable according to El-Sayed's rule as shown in Figure 9 and Table 2. As a

result, the values of SOC are too small ($< 1 \text{ cm}^{-1}$) to explain the experimentally observed decay of the $^1\pi\pi^*$ state within 10 ps.

Above calculated results are summarized in this paragraph. The excited *trans*-MC to the $^1\pi\pi^*$ state rapidly decays to the $^1n\pi^*$ state by IC followed by ISC to the triplet manifold, first to the T_3 ($^3\pi\pi^*$) *via* $^1n\pi^*/T_3$ ($^3\pi\pi^*$) MESX found near the $^1n\pi^*$ minima. After this ISC, MC relaxes to the T_2 ($^3\pi\pi^*$) by IC. OCH₃ torsion in the T_2 state changes the character to $^3n\pi^*$ and promotes IC to the T_1 ($^3\pi\pi^*$). The optimized T_1 structure has a C=C twisted form, which is close to T_1/S_0 MESXs. From the T_1 state, MC either goes back to the *trans*- S_0 or undergoes *trans* \rightarrow *cis* isomerization *via* T_1/S_0 MESXs.

3-6 C=C bond twisting route on the ${}^1\pi\pi^*$ state

Several previous studies investigated the direct *trans* \rightarrow *cis* isomerization route via ${}^1\pi\pi^*/S_0$ CI, since it is essential to examine the competition between this direct route and the ${}^1\pi\pi^* \rightarrow {}^1n\pi^*$ IC discussed in Section 3-5 for gaining an overall picture of the photoisomerization.^{2,6,14-18} Therefore, the direct isomerization route is also examined in this section.

Figure 13 shows the two competing NRD routes connected to photoisomerization from the ${}^1\pi\pi^*$ minimum (EQ 1). The rightward direction from EQ 1 is the IC to the ${}^1n\pi^*$ state (EQ 2) discussed in Section 3-5 and the leftward direction is the decay route along the C=C bond twisting on the same potential energy surface (PES) of the ${}^1\pi\pi^*$ state. TS 8 at 35751 cm^{-1} , located between EQ 1 and ${}^1\pi\pi^*/S_0$ MECI 12 was found. TS 8 is the result of the avoided crossing between the first and second ${}^1\pi\pi^*$ states,¹⁸ which consist of several $\pi \rightarrow \pi^*$ configurations such as HOMO (π) \rightarrow LUMO (π^*), HOMO-1 (π) \rightarrow LUMO (π^*) (Figure 22 in Chapter 4). The molecular orbitals involved in these states originate from the π and π^* orbitals of benzene ring and propenyl group. The weight of these $\pi \rightarrow \pi^*$ configurations changes according C=C twisting and leads to the avoided crossing TS 8. After MECI 12 \rightarrow S_0 IC, *trans* \rightarrow *cis* isomerization will occur in the S_0 state due to the large excess energy even though the IRC calculation from MECI 12 reaches *trans*- S_0 . The ZPE corrected energy of TS 1 is lower than that of TS 12 by 519 cm^{-1} . This indicates that the ${}^1\pi\pi^* \rightarrow {}^1n\pi^*$ IC route (rightward direction) is energetically more favorable than the C=C bond twisting route via

$^1\pi\pi^*/S_0$ MECI 12. This theoretical result is consistent with the experimental result that the T_1 ($^3\pi\pi^*$) corresponding to EQ 7 was detected by ns UV-DUV pump-probe measurement.

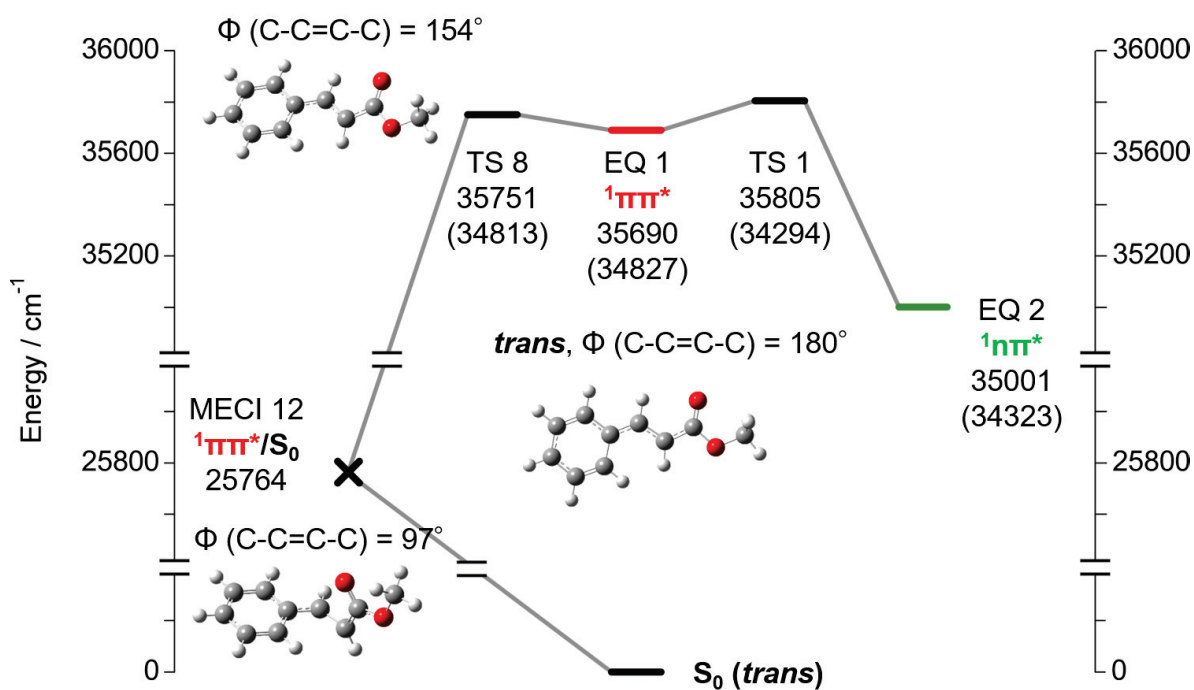


Figure 13 Two competing photoisomerization routes of MC from EQ 1 ($^1\pi\pi^*$). The leftward direction represents the direct photoisomerization process on the PES of the $^1\pi\pi^*$ state and the rightward direction represents the IC (EQ 1 \rightarrow EQ 2) process.

3-7 Conclusion

The electronic states and the NRD process of MC has been investigated under jet-cooled gas phase conditions. In the LIF spectrum, two transitions with the origin of bands A and B are observed and are assigned to the $S_0 \rightarrow S_1$ ($^1n\pi^*$) transition of TC and TT conformers, respectively. While in the 2C-R2PI spectra, a new band C appears in a higher frequency region, which is assigned to the $S_0 \rightarrow S_2$ ($^1\pi\pi^*$) transition of the TC conformer. From the lifetime measurement, it is found that the $^1n\pi^*$ state decays to the triplet state by ISC even at low excess energy. Upon excitation to the $^1\pi\pi^*$ state (band C), MC decays within 10 ps to the $^1n\pi^*$ state by IC followed by ISC to the T_1 ($^3\pi\pi^*$). Finally, MC decays to the S_0 state from the T_1 state with lifetime of ~ 20 ns. By cold matrix-isolation FTIR spectroscopy, it is found that the photoisomerization occurs upon UV irradiation.

The NRD/photoisomerization route was further explored by AFIR/TD-DFT calculation at the ω B97XD/6-311G(d,p) level. The results of calculation shows that the efficient $^1\pi\pi^* \rightarrow ^1n\pi^*$ IC process is energetically favorable compared with the C=C bond twisting process on the PES of the $^1\pi\pi^*$ state.

From these experimental and theoretical results, it is concluded that the dominant photoisomerization route of MC is described as “ S_2 ($^1\pi\pi^*$) (*trans*) $\rightarrow S_1$ ($^1n\pi^*$) $\rightarrow T_1$ ($^3\pi\pi^*$) $\rightarrow S_0$ (*trans* or *cis*)”.

References

1. T. Ebata, K. Saito, H. Ishikawa and N. Mikami, *Res. Chem. Intermed.*, 1998, **24**, 803-812.
2. Y. Miyazaki, K. Yamamoto, J. Aoki, T. Ikeda, Y. Inokuchi, M. Ehara and T. Ebata, *J. Chem. Phys.*, 2014, **141**, 244313.
3. E. M. M. Tan, M. Hilbers and W. J. Buma, *J. Phys. Chem. Lett.*, 2014, **5**, 2464-2468.
4. E. M. M. Tan, S. Amirjalayer, S. Smolarek, A. Vdovin, A. M. Rijs and W. J. Buma, *J. Phys. Chem. B*, 2013, **117**, 4798-4805.
5. E. M. M. Tan, S. Amirjalayer, B. H. Bakker and W. J. Buma, *Faraday Discuss.*, 2013, **163**, 321-340.
6. D. Shimada, R. Kusaka, Y. Inokuchi, M. Ehara and T. Ebata, *Phys. Chem. Chem. Phys.*, 2012, **14**, 8999-9005.
7. S. Smolarek, A. Vdovin, E. M. M. Tan, M. de Groot and W. J. Buma, *Phys. Chem. Chem. Phys.*, 2011, **13**, 4393-4399.
8. M. de Groot, E. V. Gromov, H. Köppel and W. J. Buma, *J. Phys. Chem. B*, 2008, **112**, 4427-4434.
9. K. M. Krokidi, M. A. P. Turner, P. A. J. Percy and V. G. Stavros, *Mol. Phys.*, 2020, DOI: 10.1080/00268976.2020.1811910.
10. W. G. Herkstroeter and S. Farid, *J. Photochem.*, 1986, **35**, 71-85.
11. M. A. El-Sayed, *J. Chem. Phys.*, 1963, **38**, 2834.
12. R. A. Marcus, *J. Chem. Phys.*, 1952, **20**, 359.
13. J. Moon, H. Baek, J. S. Lim and J. Kim, *Bull. Korean Chem. Soc.*, 2018, **39**, 427-434.
14. K. Yamazaki, Y. Miyazaki, Y. Harabuchi, T. Taketsugu, S. Maeda, Y. Inokuchi, S. Kinoshita, M. Sumida, Y. Onitsuka, H. Kohguchi, M. Ehara and T. Ebata, *J. Phys. Chem. Lett.*, 2016, **7**, 4001-4007.
15. X.-Y. Xie, C.-X. Li, Q. Fang and G. Cui, *J. Phys. Chem. A*, 2016, **120**, 6014-6022.
16. X.-P. Chang, C.-X. Li, B.-B. Xie and G. Cui, *J. Phys. Chem. A*, 2015, **119**, 11488-11497.
17. T. N. V. Karsili, B. Marchetti, M. N. R. Ashfold and W. Domcke, *J. Phys. Chem. A*, 2014, **118**, 11999-12010.
18. X. Zhao, F. Ji, Y. Liang, P. Li, Y. Jia, X. Feng, Y. Sun, Y. Shi, L. Zhu and G. Zhao, *J. Lumin.*, 2020, **223**, 117228.

Chapter 4

Substitution and its position effects on the photoisomerization of cinnamates

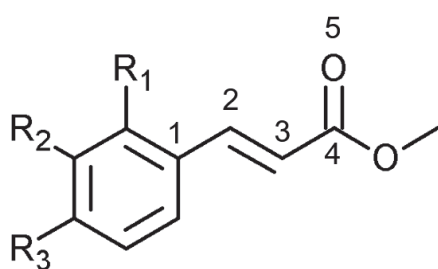
4-1 Electronic spectra of cinnamates

The electronic spectra of the $^1\pi\pi^*$ - S_0 transition for structural isomers of hydroxy methylcinnamate (*p*-, *m*-, *o*-HMC) and *para*-methoxy MC (*p*-MMC) were obtained by laser induced fluorescence (LIF) and one-color or two-color resonance two-photon ionization (1C/2C-R2PI) method. In addition, conformer specific spectra were obtained by UV-UV' hole-burning (HB) spectroscopic measurement for *m*-, *o*-HMC.

Figure 1 (a) shows the electronic spectrum of the $^1\pi\pi^*$ - S_0 transition measured by 1C-R2PI method for jet-cooled *p*-HMC. Buma and coworkers reported that the spectrum consists of the vibronic bands of four conformers.¹ Here, these four conformers are called sTC, aTC, sTT and aTT. The first notation of a/s indicates the *anti* or *syn* orientation of the OH group, the second T shows the *trans* (*E*) configuration of the $C_2=C_3$ bond, and the third T/C stands for the direction between $C_2=C_3$ and $C_4=O_5$ bonds as shown in Chart 1. Figure 2 shows the structures and relative energies corrected with zero-point energy (ZPE) of these four conformers in the S_0 state calculated at B3LYP/6-311G(d,p), PBE0/cc-pVDZ, and M05-2X/6-31+G(d) levels of theory. These calculations show the same results

for the relative energies. The energy difference between the *anti/syn* conformers is very small, while the TT conformer is $\sim 300\text{ cm}^{-1}$ higher in energy than the TC conformer. The band at 32710 cm^{-1} consists of the 0-0 bands of the sTC and aTC conformers, and the band at 32880 cm^{-1} consists of the 0-0 bands of the sTT and aTT conformers.

Figure 1 (b) shows the electronic spectrum of the $^1\pi\pi^*\text{-S}_0$ transition measured by 1C-R2PI method for jet-cooled *p*-MMC. It was reported that the electronic spectrum of *p*-MMC consists of more than three conformers. The band at $32328, 32582, 32667\text{ cm}^{-1}$ was assigned to the 0-0 band of the sTC, sTT, aTC conformer, respectively.² Similar with *p*-HMC, the notation of first a/s represents orientation of the OCH₃ group, the second T shows the *trans* (*E*) configuration of the C₂=C₃ bond, and the third T/C stands for the direction between C₂=C₃ and C₄=O₅ bonds.



Molecule	R ₁	R ₂	R ₃	Predicted number of conformers
<i>p</i> -HMC	H	H	OH	4
<i>m</i> -HMC	H	OH	H	8
<i>o</i> -HMC	OH	H	H	8
<i>p</i> -MMC	H	H	OCH ₃	4

Chart 1 Molecular structures and number of conformations for the structural isomers of HMC (*p*-, *m*-, *o*-HMC) and *p*-MMC.

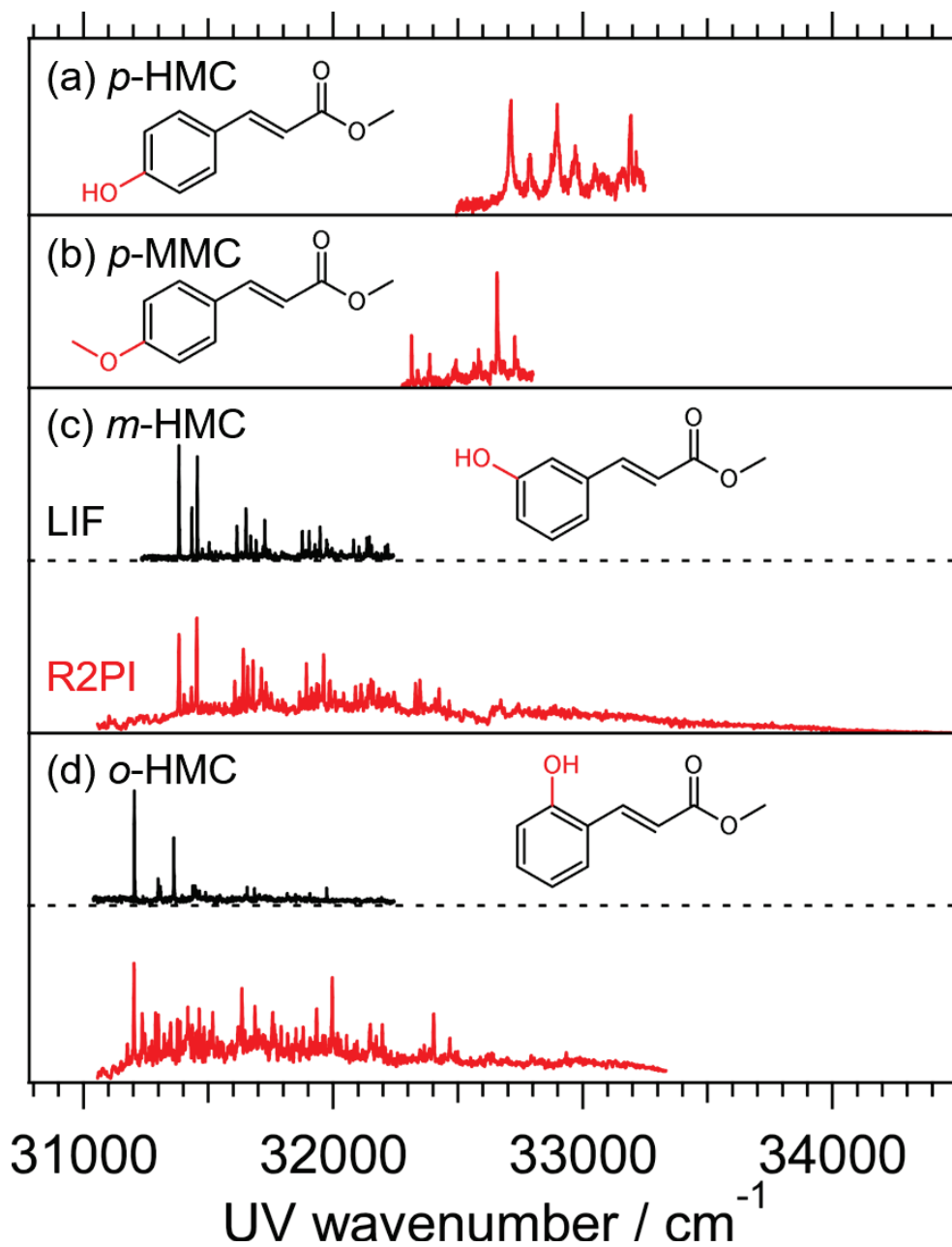
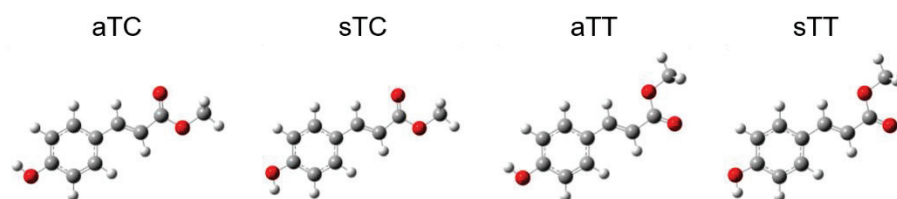


Figure 1 Electronic spectrum of jet-cooled (a) *p*-HMC and (b) *p*-MMC measured by 1C-R2PI method. Electronic spectrum of jet-cooled (c) *m*-HMC and (d) *o*-HMC measured by LIF (upper black curve) and 2C-R2PI (lower red curve) method, fixing the ν_2 to 44440 cm^{-1} (225.0 nm).



Level	Relative energy / cm^{-1}			
B3LYP/6-311G(d,p)	0	14	327	327
PBE0/cc-pVDZ	0	29	361	369
M05-2X/6-31+G(d)	0	40	304	312

Figure 2 Optimized structures of *p*-HMC in the S_0 state and their relative energies in unit of cm^{-1} calculated at (top) B3LYP/6-311G(d,p), (middle), PBE0/cc-pVDZ, and (bottom) M05-2X/6-31+G(d) levels of theory. These values are corrected with ZPE.

Figure 1 (c) and (d) shows the electronic spectrum of the ${}^1\pi\pi^*-S_0$ transition for jet-cooled *m*-HMC and *o*-HMC measured by LIF (black curve) and 2C-R2PI (red curve) method, respectively. In the 2C-R2PI measurement, frequency of ionization laser (ν_2) was fixed to 44440 cm^{-1} (225.0 nm). As shown in Chart 1, eight conformers are possible for both *m*-HMC and *o*-HMC due to the addition of the rotation along the C_1-C_2 axis (see Chart 1). Thus, one more labeling letter is added to discriminate the conformers, e.g., TTTC. The optimized structures and relative energies of the eight conformers of *m*-HMC are shown in Figure 3 (upper). By UV-UV' HB measurement, at least six conformer specific spectra were obtained shown in Figure 3 (lower), however the assignment of the observed vibronic bands to these conformers is difficult because of the lack of structural information available in an electronic/vibrational spectrum.

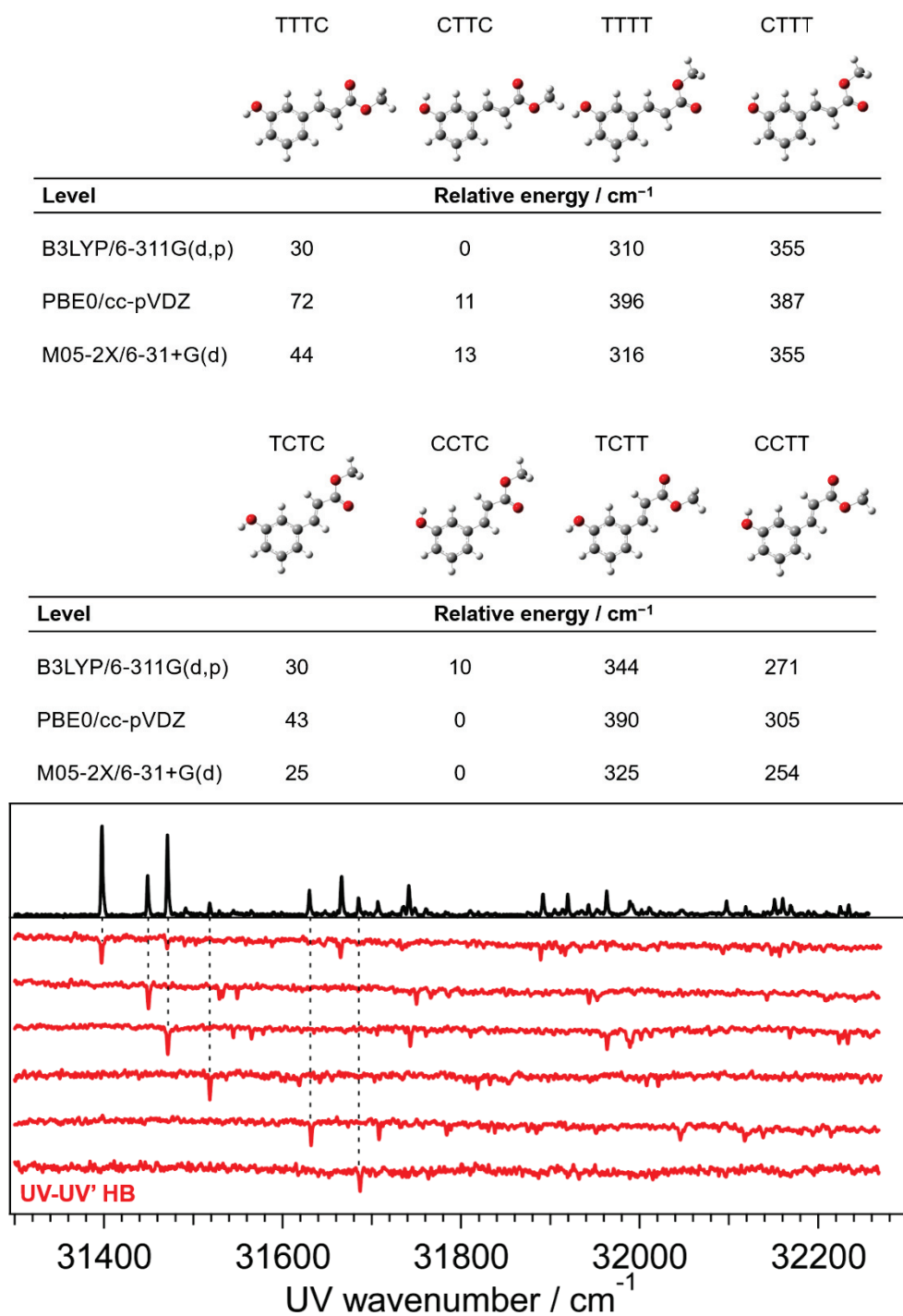


Figure 3 (Upper) Optimized structures of *m*-HMC in the S_0 state and their relative energies in unit of cm^{-1} at the several levels of theory. (Lower) (black curve) LIF excitation and (red curves) UV-UV' HB spectra of jet-cooled *m*-HMC. The frequency of probe laser was fixed to the vibronic bands marked by dot lines.

For *o*-HMC, only two conformer specific spectra were obtained due to the steric hindrance between the two substituents shown in Figure 4 (lower). The calculated S_0 energy of the TTTC and TCTC conformers at the several levels of theory is lower than those of others as shown in Figure 4 (upper), therefore it is suggested that two observed conformers can be assigned to the two stable conformers. In addition, the calculated vertical S_1 ($^1\pi\pi^*$)- S_0 excitation energy of the TTTC (33135 cm^{-1}) is lower than that of the TCTC (34436 cm^{-1}), therefore the lower energy 0-0 band can be assigned to the TTTC conformer and higher one to the TCTC conformer.

In the LIF and R2PI spectra, sharp vibronic bands can be identified up to $\sim 2000\text{ cm}^{-1}$ above the 0-0 band for both *m*-HMC and *o*-HMC. In the region higher than $\sim 2000\text{ cm}^{-1}$, the bands become broad and weak due to fast intermolecular vibrational energy redistribution (IVR) and nonradiative decay (NRD) process. Even in the R2PI spectra recorded by the ns laser, the spectra show rather broad features in higher frequency region.

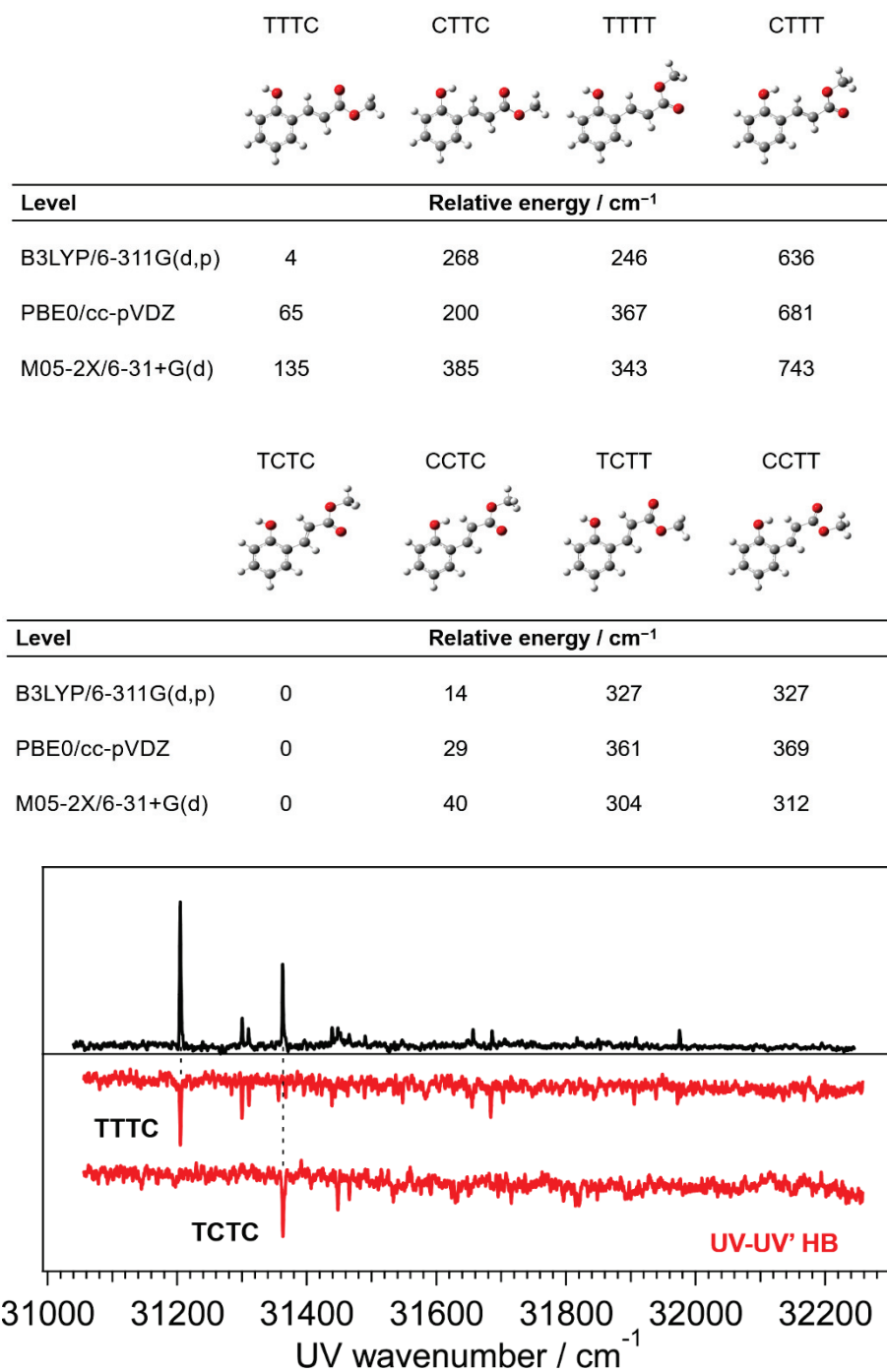


Figure 4 (Upper) Optimized structures of *o*-HMC in the S_0 state and their relative energies in unit of cm^{-1} at the several levels of theory. (Lower) (black curve) LIF excitation and (red curves) UV-UV' HB spectra of jet-cooled *o*-HMC. The frequency of probe laser was fixed to the vibronic bands marked by dot lines.

4-2 Lifetime measurement and nonradiative decay process

4-2-1 *p*-HMC and *p*-MMC

For the investigating the NRD process for *p*-HMC, the picosecond (ps) UV-UV' pump-probe and nanosecond (ns) UV-DUV pump-probe measurements were carried out. The similar measurements have already been carried out for *p*-MMC.³ Thus, in later part of this section, the results for *p*-MMC are briefly described.

Figure 5 (a) shows the energy level diagram in unit of cm^{-1} and NRD process from the $^1\pi\pi^*$ state of *p*-HMC. Figure 5 (b) shows the time profile of the $^1\pi\pi^*$ state at the 0-0 band obtained by ps UV-UV' pump-probe measurement. Here, the ν_1 and ν_2 was fixed to 32710 cm^{-1} (0-0 band) and 41670 cm^{-1} (240 nm), respectively. This ν_2 is the highest frequency can be generated with our ps laser system. The red plots are the observed ion signal, and the black curve is the convoluted decay curve fitted by assuming a single exponential decay of $\tau = 9 \text{ ps}$ with a laser pulse width (12 ps). The lifetime is upper limit that can be determined our ps laser system, thus the true lifetime will be shorter than 9 ps. The similar measurements were carried out with the several ν_1 and ν_2 as shown in Figure 6 (a)-(e), however only a fast decay component with a lifetime of 9 ps, corresponding to the $^1\pi\pi^*$ lifetime,⁴ was observed. Therefore, only a decay of the $^1\pi\pi^*$ state can be obtained by our ps laser system. The results in Figure 6 (a)-(e) also indicate either that the lifetime of the transient $^1n\pi^*$ state is too short to be detected or that the highest ν_2 is still not high enough to ionize the $^1n\pi^*$ state.

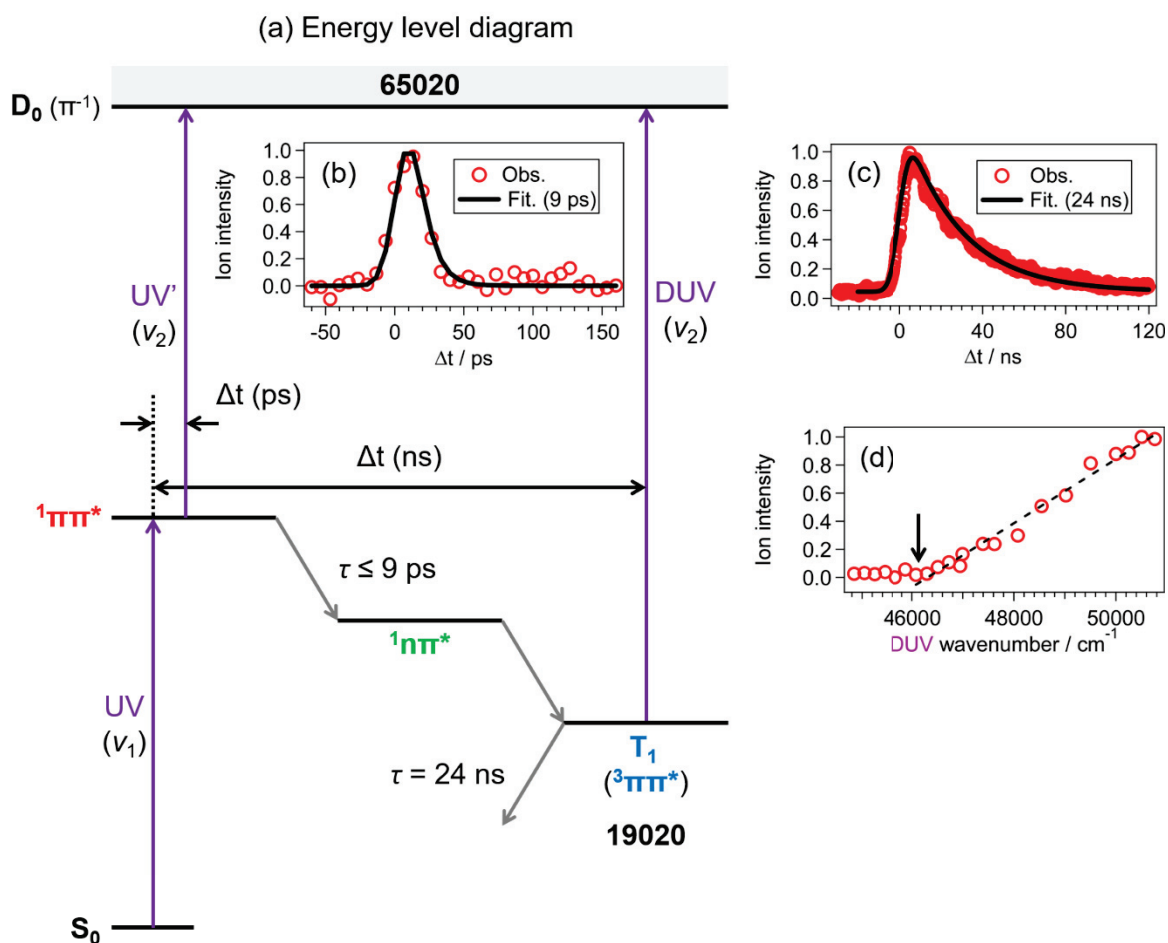


Figure 5 (a) Energy level diagram in unit of cm^{-1} and NRD process from the ${}^1\pi\pi^*$ state. (b) Time profile of the ${}^1\pi\pi^*$ state obtained by ps UV-UV' pump-probe measurement. The black curve is deconvoluted curve with laser pulse width (12 ps). (c) Time profile and (d) ionization efficiency curve of the T_1 (${}^3\pi\pi^*$) obtained by ns UV-DUV pump-probe measurement. The black curve in (c) is deconvoluted curve with laser pulse width (5 ns). The arrow in (d) indicates the ionization threshold.

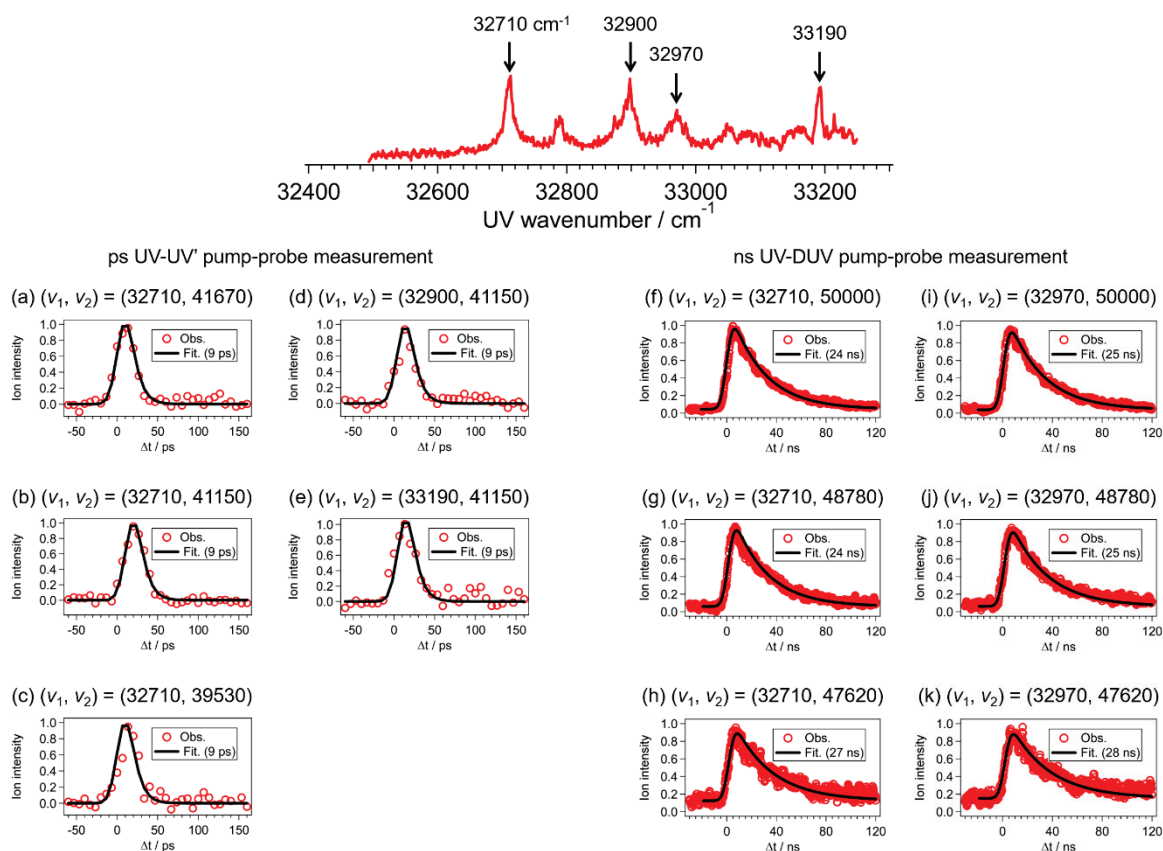


Figure 6 (Upper) 1C-R2PI spectrum of jet-cooled *p*-HMC. The arrows and values indicate the pumped bands and their frequencies in pump-probe measurement. (Lower) Time profiles obtained by (a-e) ps UV-UV' and (f-k) ns UV-DUV pump-probe measurement. The black curves correspond to deconvoluted curves. The values of the ν_1 and ν_2 used in the measurements are also shown in parenthesis.

Figure 5 (c) shows the time profile observed by ns UV-DUV pump-probe measurement, where the ν_1 and ν_2 was fixed to 32710 cm^{-1} and 50000 cm^{-1} (200 nm), respectively. The ns laser is not able to observe the fast decay (9 ps) of the

$^1\pi\pi^*$ state, but can observe slow decay with a lifetime of 24 ns. Buma and co-workers found a similar long-lived state by using ns pump-probe measurement with probe laser of 193 nm.⁵ They tentatively assigned this transient state to the $^1n\pi^*$ state, however they did not determine the energy of this state relative to the S_0 state. The slow decay component, corresponding to the transient state was also observed at the different ν_1 and ν_2 as shown in Figure 6 (f)-(k). They show almost the same decay with an average lifetime of 26 ns, indicating the generation step of transient state from the $^1\pi\pi^*$ state is timescale of sub ns.

Figure 5 (d) shows the ionization efficiency curve of this transient state. Here, the ν_1 was set to 32710 cm^{-1} and the ν_2 was scanned. The ionization threshold is seen at 46000 cm^{-1} . The calculated ionization energy (D_0) for the HMC series at the $\omega\text{B97XD/6-311G(d,p)}$ level are listed in Tale 1. It is found that the calculated value of p -HMC shows excellent agreement with the observed one (65020 cm^{-1}) reported in previous study.⁴ The ionization threshold and the lifetime of the transient state is very similar to that of the T_1 ($^3\pi\pi^*$) in MC (47300 cm^{-1} , 20 ns), thus it is strongly suggested that the transient state observed in p -HMC can be assigned to the T_1 state. Actually, the energy level of the transient (T_1) state is estimated to be 19020 cm^{-1} , assuming the ionization occurs to the D_0 state. From these results, it is concluded that upon excitation to the $^1\pi\pi^*$ state, p -HMC decays to the T_1 state in a timescale of less than a few ns. Finally, p -HMC decays to the S_0 state with a lifetime of 24 ns from the T_1 state

Table 1 Ionization energies of *p*-, *m*- and *o*-HMC calculated at the ω B97XD/6-311G(d,p) level. The observed values are also listed.

Molecule	Obs. / cm^{-1}	Calc. / cm^{-1} (ω B97XD/6-311G(d,p))
<i>p</i> -HMC	65020 ^a	65007
<i>m</i> -HMC	67613	67229
<i>o</i> -HMC	66173	65912

a) ref. 4

The similar ps UV-UV' and ns UV-DUV pump-probe measurements to *p*-HMC have already been carried out in previous study on *p*-MMC.^{2,3,5} Briefly, the $^1\pi\pi^*$ lifetime of *p*-MMC was measured as 280 ps at 0-0 band (32328 cm^{-1}). The lifetime becomes shorter with excess energy and to be 13 ps at vibronic band located at 837 cm^{-1} above the 0-0 band. The $^1\pi\pi^*$ lifetime of *p*-HMC (≤ 9 ps) is shorter than that of *p*-MMC, therefore the $^1\pi\pi^*$ potential energy curve of *p*-HMC is thought to cross nearly at the bottom of that of the $^1\pi\pi^*$ state, leading to barrierless internal conversion (IC). By ns UV-DUV measurement, the transient state (T_1) generated during the NRD process from the $^1\pi\pi^*$ state was detected. The energy and lifetime of the T_1 state was measured as 16577 cm^{-1} and ~ 20 ns, respectively. Therefore, the NRD process of *p*-MMC is thought to be essentially similar to those of MC and *p*-HMC.

4-2-2 *m*-HMC and *o*-HMC

The $^1\pi\pi^*$ lifetime at 0-0 band and vibronic bands of *m*-HMC and *o*-HMC were measured by ns UV-DUV and ps UV-UV' pump-probe measurements. In addition, dependency of the lifetime on excitation energy was also investigated.

At first, the D_0 value was measured for *m*-HMC and *o*-HMC. Figure 7 (a) and (b) shows the ionization efficiency curve of *m*-HMC and *o*-HMC from the 0-0 band of the $^1\pi\pi^*$ state, respectively, measured by ns pump-probe measurement. For *m*-HMC, the ν_1 was fixed to 31383 cm^{-1} . By scanning the ν_2 , the ionization threshold was found at $\nu_2 = 36230\text{ cm}^{-1}$, giving $D_0 = 67613\text{ cm}^{-1}$. For *o*-HMC, ν_1 was fixed to 31203 cm^{-1} . The ionization threshold was found at $\nu_2 = 34970\text{ cm}^{-1}$, giving $D_0 = 66173\text{ cm}^{-1}$. It is found that the zero-point energy (ZPE) of the $^1\pi\pi^*$ state for *m*-, *o*-HMC are less than half of their D_0 values. Thus, to carry out the pump-probe experiment, the value of the ν_2 must be higher than the ν_1 . The observed and calculated D_0 values are listed in Table 1. It is found that the calculated values show excellent agreement with the observed ones in both of *m*- and *o*-HMC.

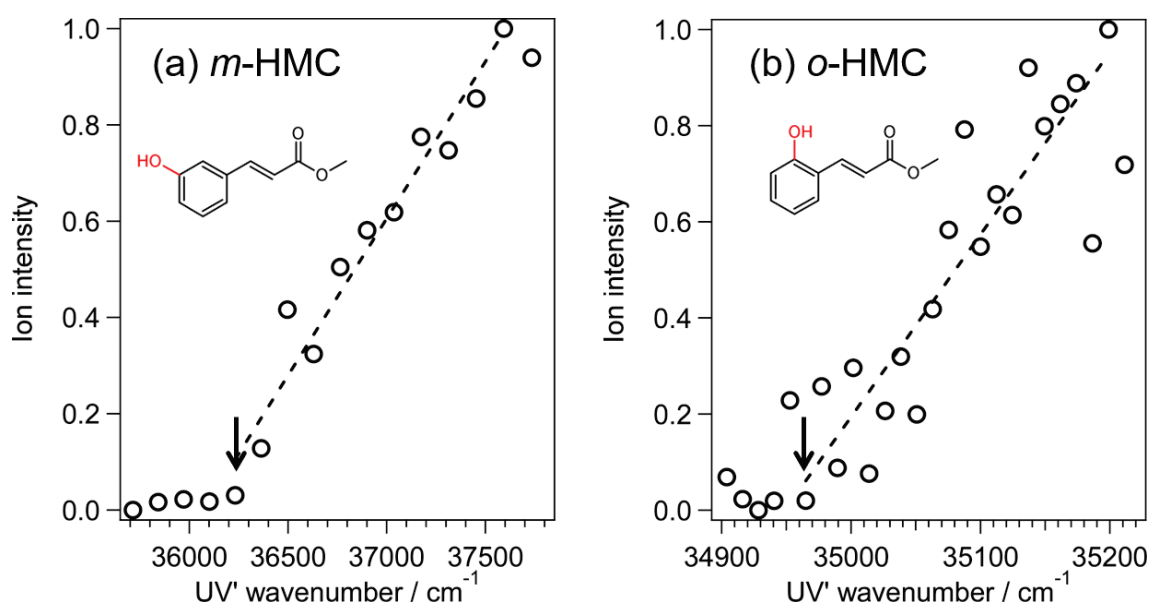


Figure 7 Ionization efficiency curve of (a) *m*-HMC from the 0-0 band of the ${}^1\pi\pi^*$ state (31383 cm^{-1}) and (b) *o*-HMC from the 0-0 band of the ${}^1\pi\pi^*$ state (31203 cm^{-1}). The arrows indicate the ionization threshold.

The ${}^1\pi\pi^*$ lifetime for *m*- and *o*-HMC was obtained by the pump-probe measurement. The lower left part in Figure 8 shows the time profiles of the vibronic bands for *m*-HMC in the region of $31380\text{--}32420\text{ cm}^{-1}$ (a-g) and at 33480 cm^{-1} (h) obtained by ns UV-DUV pump-probe measurement. The ν_2 was fixed to 49500 cm^{-1} (202 nm). All of the profiles are fitted by deconvoluted curve with laser pulse width (5 ns). The lower right part in Figure 8 shows the time profile of the vibronic bands higher than 33700 cm^{-1} (i-p) obtained by the ps UV-UV' pump-probe measurement, fixing the ν_2 to 41150 cm^{-1} (243 nm). All of the profiles are fitted by deconvoluted curves with laser pulse width (12 ps). It is found that the

lifetime at 0-0 band (10 ns, Figure 8 (a)) is much longer than those of MC and other *para*-substituted MCs, and the lifetime gradually decreases with the excitation energy. It should be found that different from MC and *para*-substituted MCs, a long lifetime component attributed to the T₁ state was not observed, although DUV light was used as a ionization laser. The ion signal in the time profile of the band h (33480 cm⁻¹) located at 2097 cm⁻¹ above the 0-0 band is mainly attributed to the ¹ππ* state ionized by DUV light. The lifetime is too fast to be determined by the ns laser system. This suggests that in *m*-HMC, the T₁ state is not generated during the NRD process.

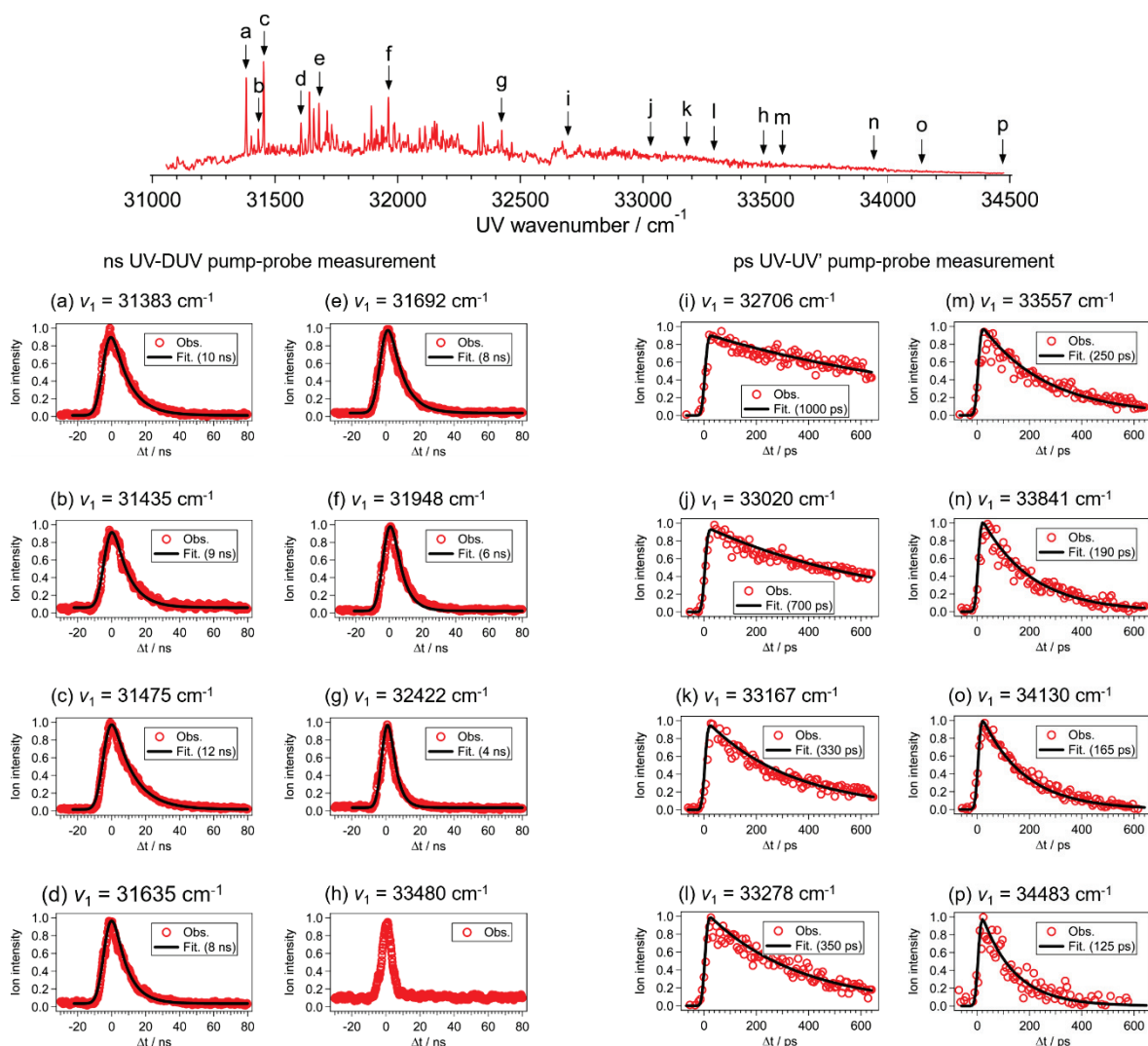


Figure 8 (Upper) 2C-R2PI spectrum of jet-cooled *m*-HMC. (Lower) Time profiles of the vibronic bands measured by (a-h) ns UV-DUV and (i-p) ps UV-UV' pump-probe measurement. The letters of (a)-(p) correspond to the frequency of the pump laser (ν_1). The black curves correspond to deconvoluted curves.

Similar measurements to *m*-HMC were carried out for *o*-HMC. Figure 9 (a) and (b) are the time profiles obtained by ns UV-DUV pump-probe measurement, fixing the ν_2 to 49500 cm^{-1} (202 nm). The $^1\pi\pi^*$ lifetimes of the vibronic bands are shorter than those of *m*-HMC, thus only the lifetime of the 0-0 band (6 ns) was obtained with the ns laser experiment. Similar to the case of *m*-HMC, a long lifetime transient state attributed to the T_1 state was not found even at the band b (33430 cm^{-1}) located at 2217 cm^{-1} above the 0-0 band, as seen in Figure 9 (b). Figure 9 (c)-(j) show the time profiles of the vibronic bands obtained by ps UV-UV' pump-probe measurement, fixing the ν_2 to 41150 cm^{-1} (243 nm). Similar to *m*-HMC, all the decay profiles are fitted by single exponential decay curves.

The effect of IVR on the decay profiles of the $^1\pi\pi^*$ state is discussed. Although, the ionization energy is high enough to detect the pumped level as well as the redistributed level in the $^1\pi\pi^*$ state by IVR, all the time profiles are fitted by single exponential decay. When IVR competes with the NRD process, the decay curve of the $^1\pi\pi^*$ state at high vibronic levels exhibit double exponential decay, because the NRD rate between the initially pumped level and the redistributed levels is thought to be different. However, all the decay curves can be fitted by single curves in both *m*-HMC and *o*-HMC, suggesting either that the two types of NRD rates mentioned above is not so different or the IVR process is too fast to observe.

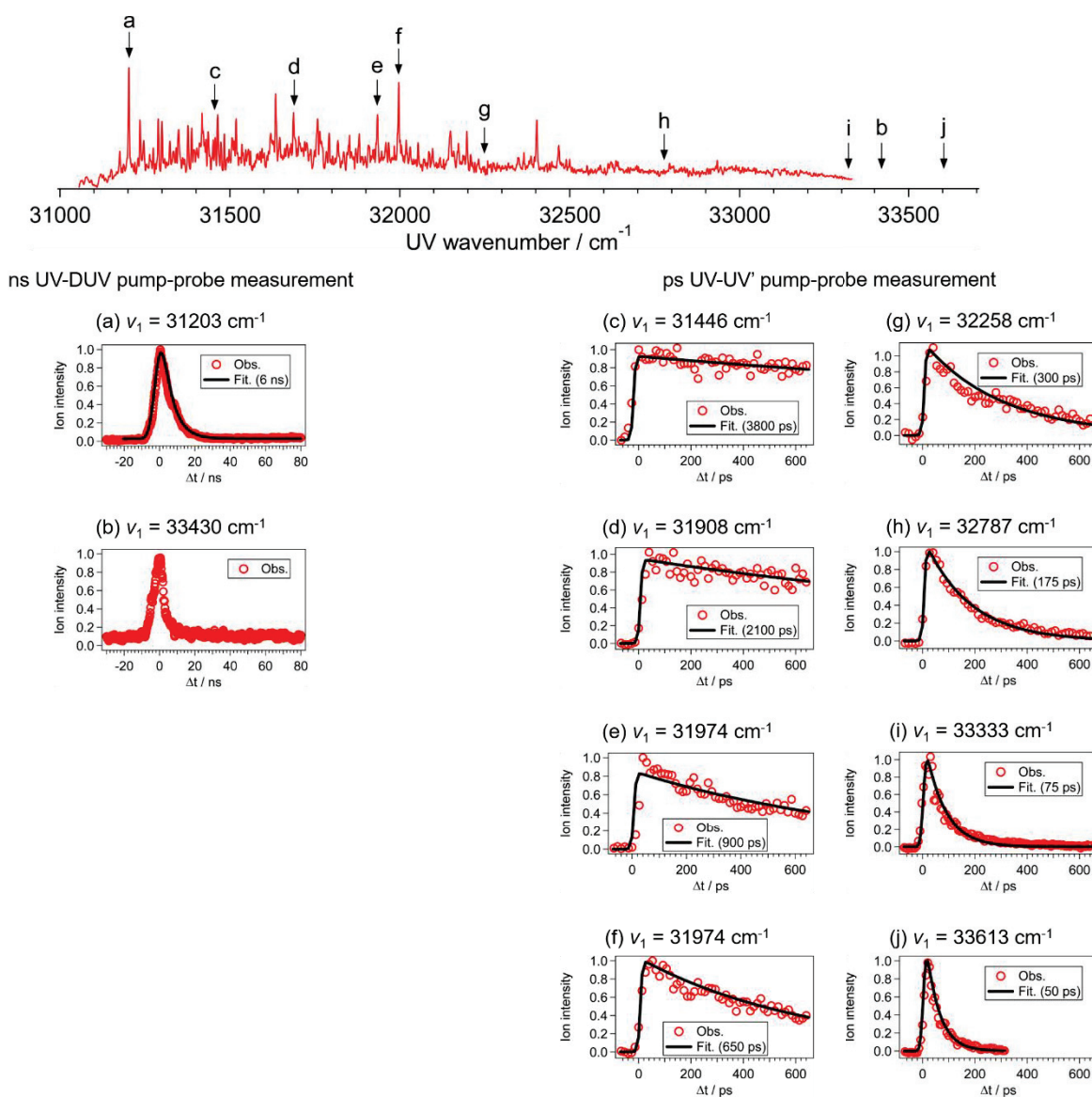


Figure 9 (Upper) 2C-R2PI spectrum of jet-cooled *o*-HMC. (Lower) Time profiles of the vibronic bands measured by (a-b) ns UV-DUV and (c-j) ps UV-UV' pump-probe measurement. The letters of (a)-(j) correspond to the frequency of pump laser (ν_1). The black curves correspond to deconvoluted curves.

Figure 10 (a) and (b) shows the plots of the decay rate constant (k), which is inverse of the $^1\pi\pi^*$ lifetime, versus the excess energy (E_{ex}), assuming E_{ex} at the 0-0 band is 0 cm^{-1} for m -HMC and o -HMC, respectively. It should be noted that even in an excess energy of 2500-3000 cm^{-1} energy region, the $^1\pi\pi^*$ decay rate constants of m -HMC and o -HMC are much smaller than that of p -HMC at the 0-0 band ($1.1 \times 10^{11} \text{ s}^{-1}$). In m -HMC, the constant, k shows a remarkable increase at $E_{\text{ex}} = \sim 1000 \text{ cm}^{-1}$, indicating an opening of the NRD channel. In o -HMC, a similar onset is seen at $E_{\text{ex}} = \sim 600 \text{ cm}^{-1}$.

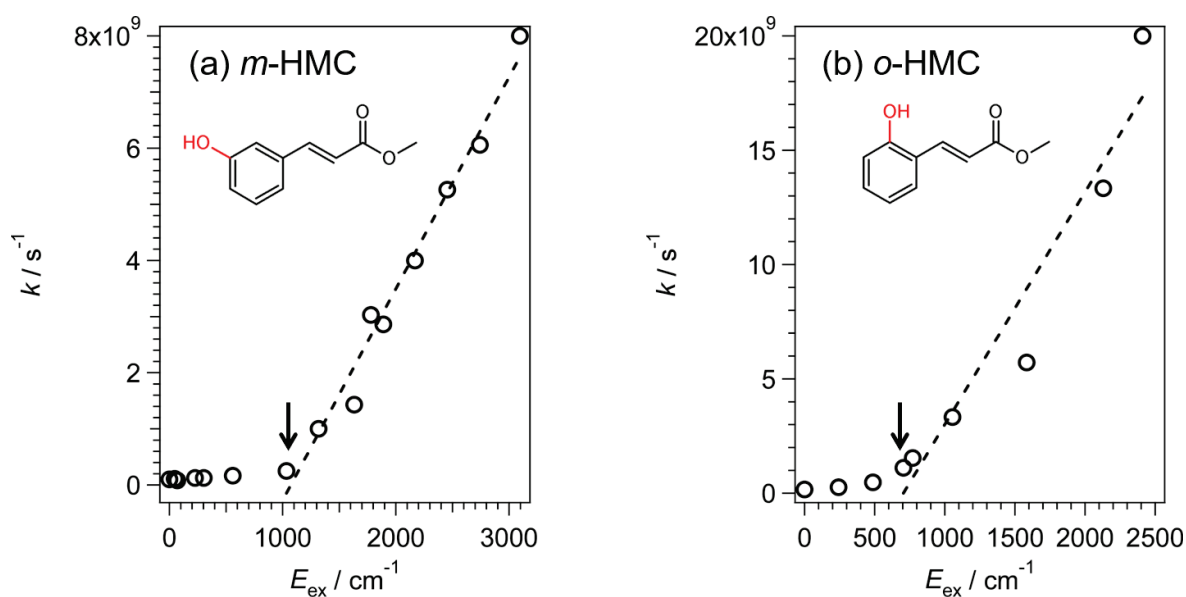


Figure 10 Plots of the rate constant, k for (a) m -HMC and (b) o -HMC as a function of E_{ex} . The arrows indicate an increase of the rate constant, k .

4-3 Photoproduct analysis upon UV irradiation

For identifying the photoproduct upon UV irradiation, cold matrix-isolation FTIR spectroscopy was performed for all of the structural isomers of HMC (*p*-, *m*-, *o*-HMC). The obtained difference IR spectra before and after UV irradiation were compared with the calculated ones between *trans* (*E*) and *cis* (*Z*) isomer at the B3LYP/6-311++G(d,p) level.

Figure 11 (a) shows the FTIR spectrum of matrix-isolated *p*-HMC before UV irradiation. The IR spectrum exhibits a strong peak at 1174 cm^{-1} and other relatively weak peaks. To reproduce the observed spectrum, the conformational stabilities and IR intensities were analyzed by comparison with DFT calculations. The optimized structures and their relative energies at the B3LYP/6-311++G(d,p), PBE0/cc-pVDZ, and M05-2X/6-31+G(d) levels are summarized in Figure 2. Figure 11 (b) and (c) is the calculated IR spectra of the TC and TT conformers, respectively. The red and blue curve indicates *anti* and *syn*, respectively, giving nearly identical IR spectra. In addition, their stability is not distinguishable. Therefore, the differences in the TC and TC conformers will not be discussed. The vibrational frequencies were scaled by a factor of 0.9941 to fit the observed IR band can be assigned to the C-O stretch of the ester group at 1171 cm^{-1} . The absorption intensity implies that the TC conformer is more populated than the TT conformer. In fact, the sum of the calculated spectra of the conformers is best reproduced by the Boltzmann distribution of the vaporized temperature and the conformational stability, as shown in Figure 11 (d).

Figure 11 (e) shows the difference FTIR spectrum of *p*-HMC before and after UV irradiation at $\lambda_{UV} \geq 300$ nm. The positive absorption indicates the photoproduct and the negative one is the depleted population of the initial reactant. For simplicity, the most stable aTC conformer is considered to be the initial reactant. Figure 11 (f)-(h) display the comparison of the IR spectra assuming that the *trans* \rightarrow *cis* isomerization occurs from the aTC reactant to the sCC, aCC and aCT products, respectively. The structures and relative energies of the optimized *cis*-isomers obtained at the B3LYP/6-311G(d,p) level of theory are shown in the Figure 12. Some typical vibrations indicating the production of the *cis*-isomer, such as propenyl C=C stretching at ~ 1630 cm^{-1} and C=O stretching at ~ 1740 cm^{-1} highlighted by yellow line were observed in the difference IR spectrum. In addition, the ring C-C stretching vibration at ~ 1610 cm^{-1} shows a typical shift in the *cis*-isomer. The possibility of a *s-cis* \rightarrow *s-trans* conformational change within the *trans*-configuration, such as aTC or sTC, can be ruled out due to poor agreement with the observed difference spectrum. Therefore, it is found that the *trans* \rightarrow *cis* isomerization occurs in *p*-HMC upon UV irradiation, which is essentially the same results as that reported previously for *p*-MMC.⁶

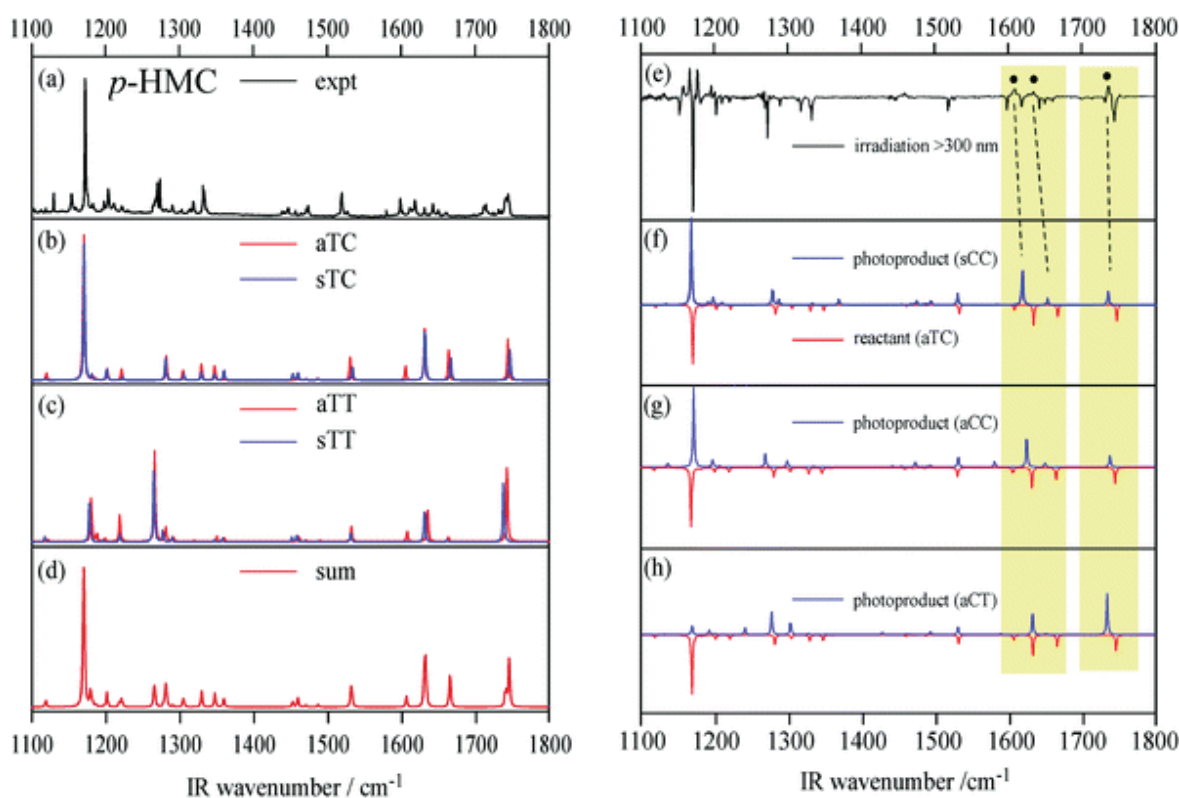


Figure 11 (a) FTIR spectrum of matrix-isolated *p*-HMC. (b and c) Calculated IR spectra of four conformers at the B3LYP/6-311++G(d,p) level. (d) Calculated IR spectrum obtained by combining the four conformers assuming a Boltzmann distribution at the vaporized temperature (302 K). The calculated vibrational frequencies were scaled by a factor of 0.9941. (e) Different FTIR spectra of the matrix-isolated *p*-HMC before and after UV irradiation at $\lambda_{UV} \geq 300$ nm. Positive peaks correspond to the product and negatives ones are depletion of the reactant. (f-h) Comparison of the IR spectra of the *cis*-products (blue) and the *trans*-reactants (red). The dotted bands are typical bands of the *cis*-products.

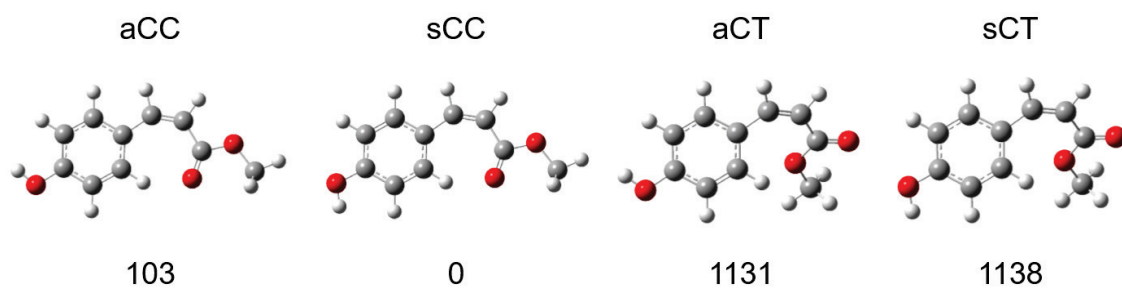


Figure 12 Optimized structures of *cis-p*-HMC in the S_0 state calculated at the B3LYP/6-311G(d,p) level of theory. Their relative energies corrected with ZPE are also shown in unit of cm^{-1} . aCT and sCT are the non-planar structures where the ester sp^3 orbital is interacted with aromatic C-H.

Figure 13 (a) shows the matrix-isolated FTIR spectrum of *m*-HMC. Figure 13 (b)-(e) are the IR spectra of the possible abundant conformers obtained by B3LYP/6-311++G (d,p) calculations (see Figure 3). The vibrational frequencies were scaled by a factor of 0.9927 to fit the observed IR band of the C-O stretch of the ester group at 1176 cm⁻¹. The experimental spectrum is reproduced by adding the calculated spectra of the conformers and considering the Boltzmann distribution of the vaporized temperature (302 K), as shown in Figure 13 (f). The calculated spectra show reasonable agreement with the observed one. At first, UV light at $\lambda_{UV} \geq 320$ nm, near the 0-0 band, was irradiated to observe the product. However, since vibration due to the photoproduct was not observed, the photochemical reaction does not occur at this wavelength.

Figure 13 (g) shows the difference IR spectrum of *m*-HMC before and after UV irradiation at $\lambda_{UV} \geq 300$ nm, where several new bands due to the photoproduct appear. The calculated result for the optimization of the *cis*-*m*-HMC in Figure 14 indicates that the CCCC conformer is most stable among the others. Thus, CCCC was selected as the major photoproduct and its calculated IR spectrum was compared with those of the *trans*-*m*-HMC, as seen in Figure 13 (h)-(k). Although the assumption of the production of one conformer (CCCC) is very simple, it is found that the bands at 1635 cm⁻¹ (propenyl C=C stretching band) and 1740 cm⁻¹ (C=O stretching) of the *cis*-*m*-HMC (CCCC) can be assigned to the newly appearing (product) peaks. Thus, it is concluded that the *trans* → *cis* isomerization occurs by UV irradiation of *trans*-*m*-HMC.

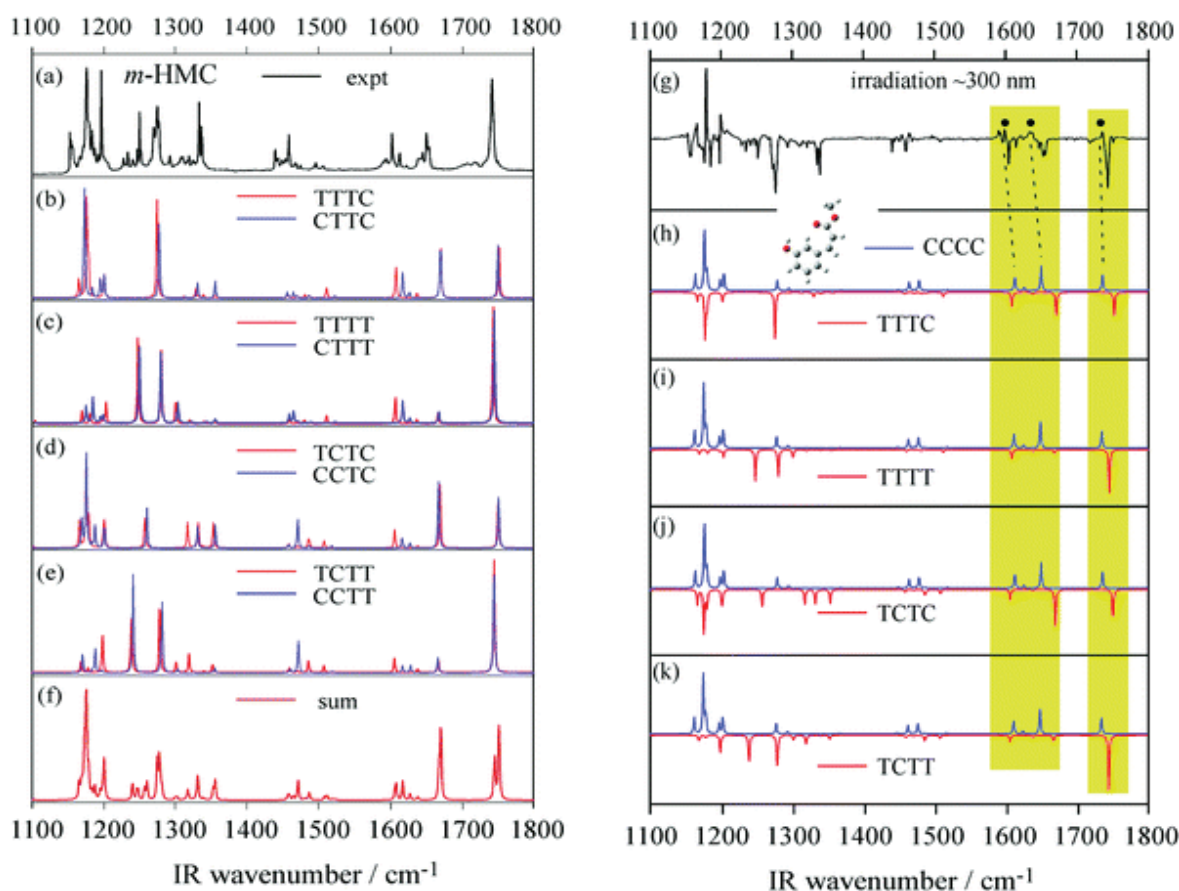


Figure 13 (a) FTIR spectrum of matrix-isolated *m*-HMC before UV irradiation. (b-e) Calculated IR spectra of *trans*-*m*-HMC at the B3LYP/6-311++G(d,p) level. The red and blue spectra indicate OH-*trans* and OH-*cis*, respectively. (f) The sum of the calculated spectra using the Boltzmann distribution at the vaporizing temperature and relative energies. The vibrational frequencies were scaled by a factor of 0.9927. (g) Difference IR spectrum of matrix-isolated *m*-HMC before and after UV irradiation at $\lambda_{UV} \geq 300$ nm. (h-k) Comparison of the difference IR spectra of the *cis*-product (CCCC conformer) and various conformers of *trans*-*m*-HMC. The dotted bands are typical bands of the *cis*-products.

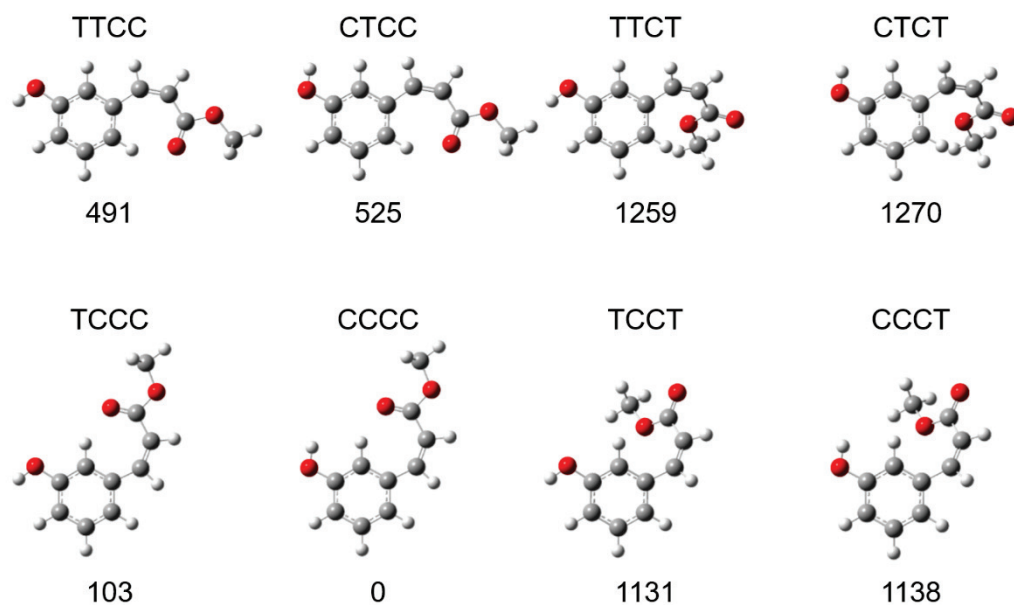


Figure 14 Optimized structures of *cis-m*-HMC in the S_0 state calculated at the B3LYP/6-311G(d,p) level of theory. Their relative energies corrected with ZPE are also shown in unit of cm^{-1} .

Figure 15 (a) shows the matrix-isolated FTIR spectrum of *o*-HMC. Figure 15 (b)-(e) are the calculated IR spectra of the possible abundant conformers (see Figure 4). The experimental spectrum is reproduced by the sum of the calculated spectra of the Figure 15 (b) and (c) by considering the Boltzmann distribution of the vaporized temperature and relative energies of the conformers. The vibrational frequencies were scaled by a factor of 0.9926 to fit the observed IR band of the C-O stretch of the ester group at 1171 cm⁻¹. The resultant spectrum in Figure 15 (f) reasonably reproduces the observed one in Figure 15 (a).

Figure 15 (g) shows the difference IR spectrum of *o*-HMC before and after UV irradiation at $\lambda_{UV} \geq 300$ nm. Similar to the case of *m*-HMC, the product was not observed by $\lambda_{UV} \geq 320$ nm excitation. In Figure 15 (g), several new bands (marked by dots) were observed as the photoproduct, which may be *cis*-*o*-HMC. The optimized structures in the S₀ state and the relative energies of *cis*-*o*-HMC are shown in Figure 16. Among them, the CCCC conformer will be a major product, because the conformer is most stable due to hydrogen bonding between the OH group at the *ortho*-position and the C=O of the ester group. Thus, the calculated IR spectrum of the CCCC conformer was compared with those of several conformers of *trans*-*o*-HMC, as seen in Figure 15 (h)-(k). The observed peak at 1633 cm⁻¹ can be assigned to the propenyl C=C stretching mode. In addition, the C=O stretching band at 1710 cm⁻¹ is well reproduced in the calculated spectrum of the CCCC conformer. Therefore, it is also concluded that *trans* → *cis* isomerization occurs in *trans*-*o*-HMC upon UV irradiation.

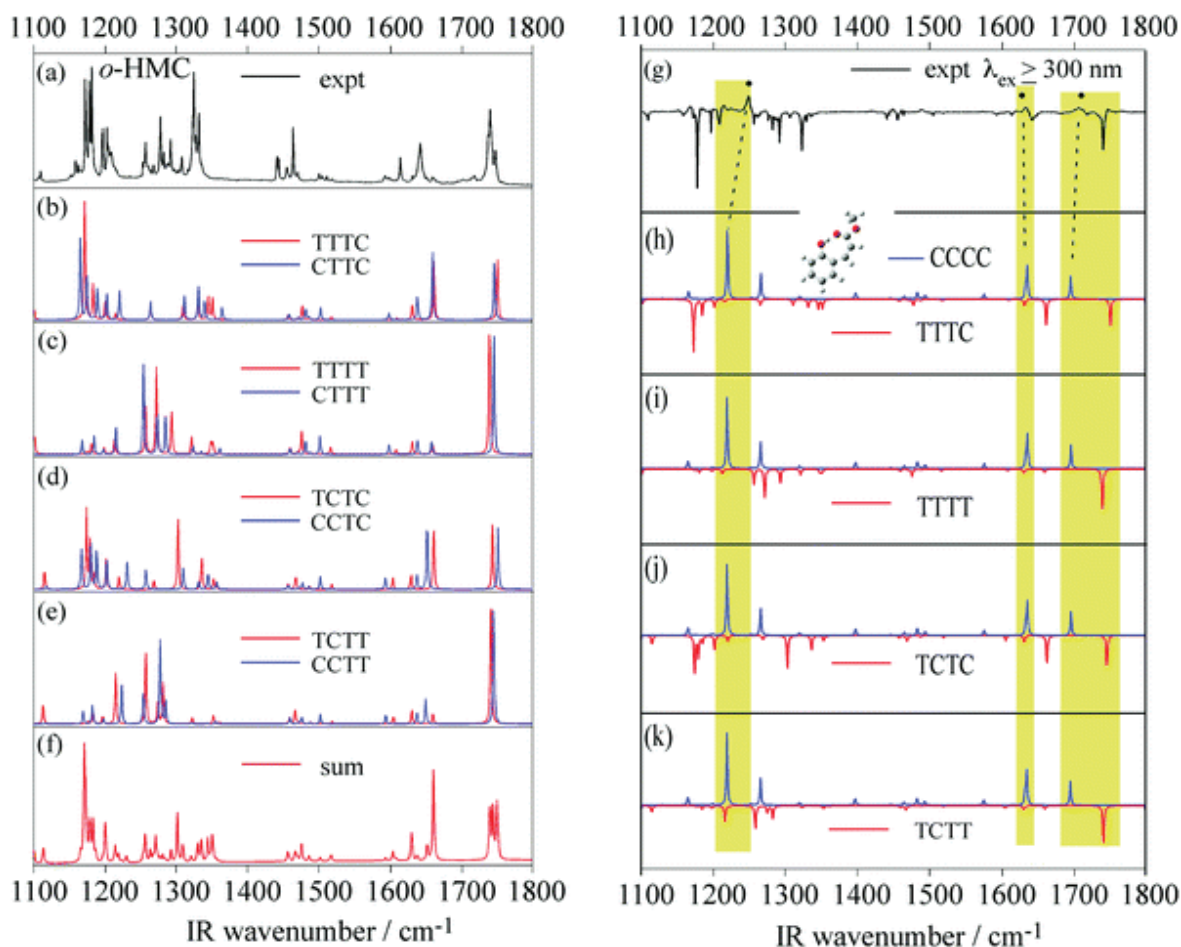


Figure 15 (a) FTIR spectrum of matrix-isolated *o*-HMC before UV irradiation. (b-e) Calculated IR spectra of *trans*-*o*-HMC at the B3LYP/6-311++G(d,p) level. The red and blue spectra indicate OH-*trans* and OH-*cis*, respectively. (f) The sum of the calculated spectra using the Boltzmann distribution at the vaporizing temperature (302 K) and relative energies for conformers. The vibrational frequencies were scaled by a factor of 0.9926. (g) Difference IR spectrum of matrix-isolated *o*-HMC after UV irradiation at $\lambda_{UV} \geq 300$ nm. (h-k) Comparison of the IR spectra of the *cis*-product (CCCC conformer) and various conformers of *trans*-*o*-HMC. The dotted bands are typical bands of the *cis*-products.

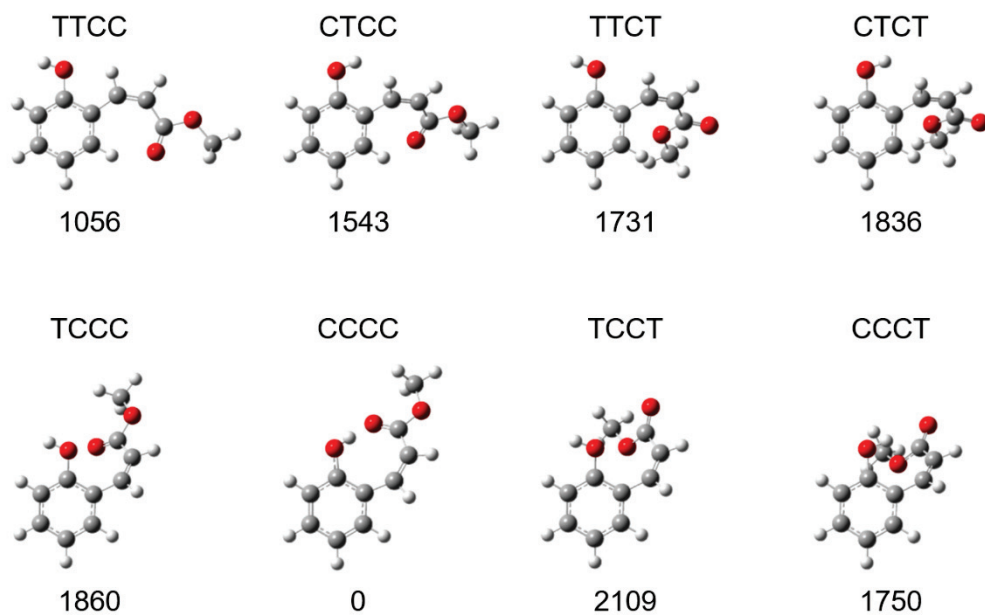


Figure 16 Optimized structures of *cis-o*-HMC in the S_0 state calculated at the B3LYP/6-311G(d,p) level of theory. Their relative energies corrected with ZPE are also shown in unit of cm^{-1} .

4-4 Systematic search for the NRD/photoisomerization route

4-4-1 *p*-HMC and *p*-MMC

From the results of pump-probe measurement in Section 4-2-1, it is found that for *p*-HMC, the $^1\pi\pi^*$ lifetime at 0-0 band is too short to be measured (≤ 9 ps). For *p*-MMC, the $^1\pi\pi^*$ lifetime (280 ps) is relatively longer than that of *p*-HMC. In addition, the transient T_1 ($^3\pi\pi^*$) was detected in these cinnamates by DUV ionization laser, suggesting that the generation of the transient T_1 during the NRD/photoisomerization route from the $^1\pi\pi^*$ state is common process among MC, *p*-HMC and *p*-MMC. Thus, the stable conformers of the T_1 state were explored using U ω B97XD/6-311G(d,p) calculations.

Two C=C twisted T_1 minima (EQ), *p*-EQ 1 and *p*-EQ 2, were found as shown in Figure 17. The C=C torsional angle is 91° in *p*-EQ 1 and 89° in *p*-EQ 2. The calculated transition energy from the *trans* conformer of the S_0 state is 17900 cm^{-1} for *p*-EQ 1 and 17804 cm^{-1} for *p*-EQ 2, both of which agree with the experimental value of 19020 cm^{-1} (Section 4-2-1). The calculated energy difference between *p*-EQ 1 and *p*-EQ 2 is only 96 cm^{-1} . Hence, there is an equilibrium between the two conformers and they co-exist with a ratio of *p*-EQ 1 : *p*-EQ 2 $\approx 4 : 5$, assuming a Boltzmann distribution at 580 K, which corresponds to the excess energy in the T_1 state.

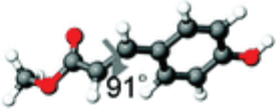
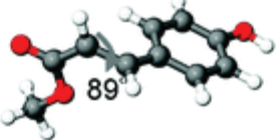
EQ	Structure	Energy / cm^{-1}
<i>p</i> -EQ 1		17900
<i>p</i> -EQ 2		17804
Exp.	-----	19020

Figure 17 Optimized structures and 0-0 transition energies of *p*-HMC in the T_1 state calculated at the U ω B97XD/6-311G(d,p) leve.

The similar feature of *p*-MMC to that of *p*-HMC discussed above was reported in ref. 3. In ref. 3, two C=C twisted structures, called EQ 6 and 7, were found in the T_1 state. The torsional angle is -96° in EQ 6 and 95° in EQ 7. The calculated energy of these T_1 structure is 18034 cm^{-1} for EQ 6 and 17983 cm^{-1} for EQ 7, both of which agrees with the experimental value of 16577 cm^{-1} (Section 4-2-1). They coexist with the ratio of EQ 6 : EQ 7 \approx 4 :5 assuming the Boltzmann distribution at 600 K, which corresponds to the excess energy in the T_1 state.

Different from the case of MC, the doorway $^1n\pi^*$ state during the NRD route was not directly observed in electronic spectra of *p*-HMC and *p*-MMC (see Section 4-1). Thus, the whole NRD route from the $^1\pi\pi^*$ state to the T_1 state for *para*-substituted MCs will be theoretically discussed in Section 4-5.

4-4-2 *m*-HMC and *o*-HMC

In contrast to *p*-HMC, the $^1\pi\pi^*$ lifetimes of *m*-HMC and *o*-HMC are 1000 times longer at the 0-0 band. This can be understood by considering that the potential crossing between the $^1\pi\pi^*$ state and the excited electronic state leading to the NRD channel, such as the $^1n\pi^*$ state, occurs at higher energies in *m*-HMC and *o*-HMC than in *p*-HMC. The plots of the decay rate constants vs. the excess energy in Figure 10 indicate that the opening of the NRD channel occurs at excess energy of $\sim 1000\text{ cm}^{-1}$ in *m*-HMC and $\sim 600\text{ cm}^{-1}$ in *o*-HMC. As discussed above, this is in accordance with the cold matrix-isolation experiment, in which excitation by $\lambda_{\text{UV}} \geq 320\text{ nm}$ (near the 0-0 band) does not produce the *cis*-product in *m*-HMC and *o*-HMC, and an excess energy of 2000 cm^{-1} (300 nm) at the maximum is necessary to promote effective photoisomerization. Another important difference between *m*-, *o*-HMC and *p*-HMC is that the transient T_1 state was not observed in *m*-HMC and *o*-HMC even at an excess energy of $\sim 2200\text{ cm}^{-1}$ in the $^1\pi\pi^*$ state. This suggests that in *m*-HMC and *o*-HMC, the T_1 state is not a precursor of the *cis*-product and the photoisomerization proceeds *via* a different route from that of *p*-HMC.

The observed excess energy dependence of the decay rate constant of *m*-HMC and *o*-HMC is discussed based on the theoretical results of the NRD pathways. It is experimentally found that the major decay route of the $^1\pi\pi^*$ state turns from radiative into nonradiative at a threshold energy of $\sim 1000\text{ cm}^{-1}$ for *m*-HMC and $\sim 600\text{ cm}^{-1}$ for *o*-HMC, and above these energies, the decay rate constant of the $^1\pi\pi^*$ state linearly increases with the excess energy. The calculated

radiative lifetime, $\tau_{\text{rad}} = 1/k_{\text{rad}}$ at the TD- ω B97XD/6-311G(d,p) and Symmetry Adapted Cluster/Configuration Interaction calculation (SAC-CI)/D95(d) levels of theory⁷ is summarized in Table 2. These calculated values agree with the experimental ones both for *m*-HMC and *o*-HMC. Thus, it is concluded that below the threshold, the $^1\pi\pi^*$ state undergoes radiative decay.

Above this threshold, the NRD pathway becomes accessible. Several NRD routes were examined: (1) NRD to the $^1n\pi^*$ state *via* the $^1\pi\pi^*/^1n\pi^*$ minimum energy conical intersection (MECI) followed by $^1n\pi^* \rightarrow T_n$ intersystem crossing (ISC), (2) ISC from the $^1\pi\pi^*$ to $^3n\pi^*$ or $^3\pi\pi^*$ state, and (3) structural change along the C=C twisted coordinate on the $^1\pi\pi^*$ surface followed by IC to the S_0 state *via* $^1\pi\pi^*/S_0$ MECI, which triggers *trans* \rightarrow *cis* isomerization. It is concluded that route (3) is the most likely, as shown in Figure 18. In Figure 18 (a), the activation barrier of transition state (TS 1) is located at $\varphi \sim 135^\circ$, connecting the energy minimum of the *trans* isomer in the $^1\pi\pi^*$ states and MECI 1 ($^1\pi\pi^*/S_0$), the barrier height of which was calculated to be 1257 cm^{-1} for *m*-HMC. For *o*-HMC in Figure 18 (b), the barrier was calculated to be 649 cm^{-1} . In both cases, a ZPE correction is included. These values are close to the experimentally obtained threshold energies of the lifetime shortening: $\sim 1000 \text{ cm}^{-1}$ for *m*-HMC and $\sim 600 \text{ cm}^{-1}$ for *o*-HMC. Some of photoexcited *m*-HMC and *o*-HMC can return to the *trans* isomers after the IC at the MECI 1. The MECI 1 locates on the more *trans*-side ($\varphi = 98^\circ$ for *m*-HMC and 102° for *o*-HMC) than TS 2 of *trans* \rightarrow *cis* isomerization in the S_0 state ($\varphi = 90^\circ$). The calculated *meta*-IRC from the MECI 1 to the S_0 state reaches the

trans-isomer both for *m*-HMC and *o*-HMC. After the *trans* → *cis* isomerization in the S₀ state, further conformational change to the most stable CCCC conformer (see Figure 18 (a) and (b)) will occur due to the large excess energy and trivial activation barriers.

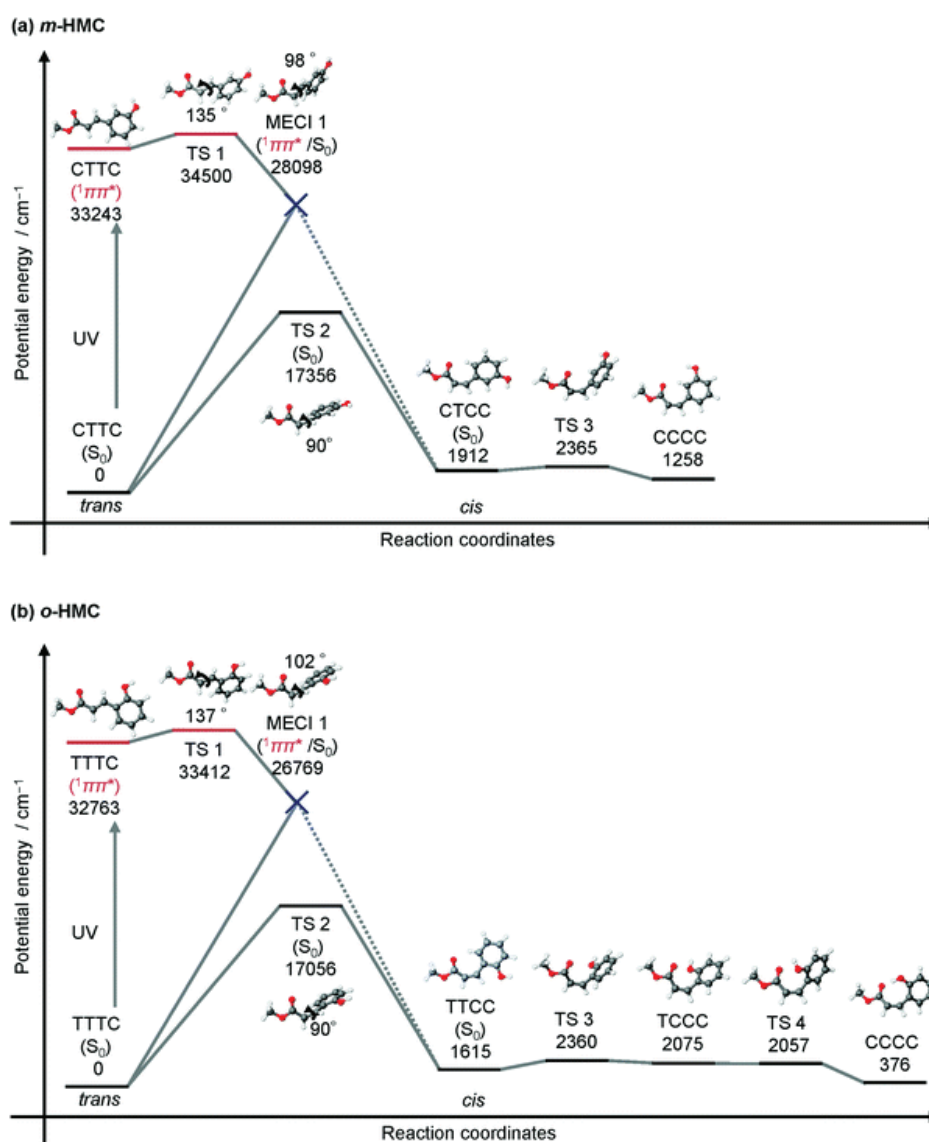


Figure 18 Potential energy profiles from the photoexcited *trans*-HMC to the *cis*-product and the subsequent conformational change in (a) *m*-HMC and (b) *o*-HMC. The EQs and TSs were optimized at the (TD-)(U)ωB97XD/6-311G(d,p) level of theory. ZPE corrections are included to calculate the relative potential energies. MECI 1 was optimized at the spin-flip TD-BHandHLYP/6-311G(d,p) levels of theory. ZPE corrections are not included to calculate the relative potential energies of MECI 1.

Table 2 Comparison between the observed and calculated radiative lifetime, τ_{rad} of the $^1\pi\pi^*$ state of *m*-HMC and *o*-HMC in time scale of ns.

	Obs. / ns	Calc. / ns	
Molecule		TD- ω B97XD/6-311G(<i>d,p</i>)	Calc. (SAC-CI/D95(<i>d</i>))
<i>m</i> -HMC	10	4.5	6.2
<i>o</i> -HMC	6	2.7	4.4

a) ref. 7

It was also theoretically investigated the other two NRD routes: (route 1) IC to the $^1n\pi^*$ state followed by ISC to triplet states and (route 2) direct ISC to triplet states, and is concluded that neither of them contributes significantly to the NRD process. Figure 19 summarizes the relative energies of the MECI and minimum energy seam of crossing (MESX) near the $^1\pi\pi^*$ EQ of the *trans* isomers of *m*-HMC and *o*-HMC. The IC to the $^1n\pi^*$ state is energetically unfavorable. The energy of EQ 3 ($^1n\pi^*$) is 935 and 1517 cm^{-1} higher than the $^1\pi\pi^*$ EQ in *m*-HMC and *o*-HMC, respectively. Accordingly, $^1\pi\pi^*/^1n\pi^*$ MECI 2 is located at 1695 cm^{-1} in *m*-HMC and 1988 cm^{-1} in *o*-HMC. Both are energetically higher than the C=C rotation energy barrier. The energies of the several low-lying electronic states that will be involved in NRD calculated by the TD- ω B97XD/6-311G(*d,p*) level of theory are listed in Table 3.

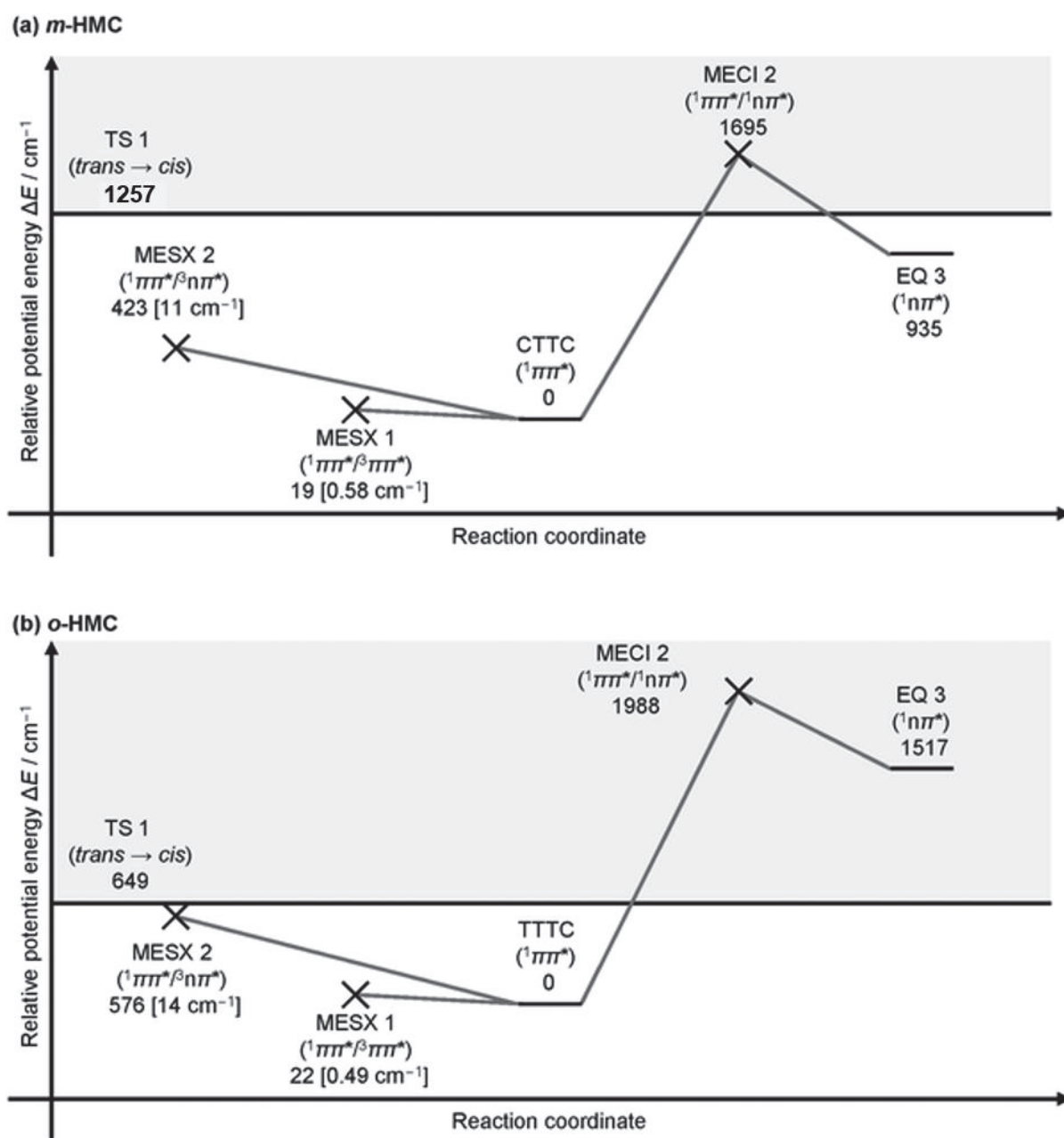


Figure 19 Potential energy profile of IC to the $^1n\pi^*$ state, and ISC to triplet states from the $^1\pi\pi^*$ state; (a) *m*-HMC and (b) *o*-HMC. All the structures were optimized at the TD- ω B97XD/6-311G(d,p) level of theory. ZPE corrections are included to calculate the relative potential energies of EQs and TS but not MECI and MESX. The calculated values of $|\text{SOC}|$ at the TD- ω B97XD/6-311G(d,p) level of theory are displayed in square brackets.

Table 3 Potential energy, E of (a) *trans-m*-HMC and (b) *trans-o*-HMC at the $^1\pi\pi^*$ EQ calculated at the TD- ω B97XD/6-311G(d,p) level of theory. The origin of the energy is the S_0 EQ of each molecule.

(a) <i>trans-m</i> - HMC			(b) <i>trans-o</i> - HMC		
State	Character	E / cm^{-1}	State	Character	E / cm^{-1}
T ₁	$^3\pi\pi^*$	16779	T ₁	$^3\pi\pi^*$	16095
T ₂	$^3\pi\pi^*$	28111	T ₂	$^3\pi\pi^*$	30060
T ₃	$^3\pi\pi^*$	33273	T ₃	$^3\pi\pi^*$	32674
T ₄	$^3n\pi^*$	35424	T ₄	$^3n\pi^*$	35321
S ₁	$^1\pi\pi^*$	32671	S ₁	$^1\pi\pi^*$	32149
S ₂	$^1\pi\pi^*$	37904	S ₂	$^1n\pi^*$	38024
S ₃	$^1n\pi^*$	38184	S ₃	$^1\pi\pi^*$	38245

The ISC routes from the $^1\pi\pi^*$ state (route 2) was also examined. It is concluded that the routes are kinetically unfavorable. In large polyatomic molecules with a high density of the vibrational levels (the statistical limit), the ISC rate constant, k_{ISC} , is given by,⁸

$$k_{\text{ISC}} = \frac{2\pi}{\hbar} |\langle T_n | H_{\text{SO}} | S_1 \rangle|^2 \rho(E_{\text{ex}}) \quad (2)$$

where $\langle T_n | H_{\text{SO}} | S_1 \rangle$ is the norm of the spin-orbit coupling constants (SOCs) between the S_1 and triplet (T_n) states at MESXs, and $\rho(E_{\text{ex}})$ is the vibrational density of states at excess energy E_{ex} from T_n . In Figure 19, both MESX 1

(${}^1\pi\pi^*/{}^3\pi\pi^*$, S_1/T_3) and MESX 2 (${}^1\pi\pi^*/{}^3\pi\pi^*$, S_1/T_4) are energetically lower than TS 1. The value of SOC at the MESX 1 is 0.58 cm^{-1} for *m*-HMC and 0.49 cm^{-1} for *o*-HMC. These small values are reasonable from the viewpoint of El-Sayed's rule,⁹ that is, that ${}^1\pi\pi^* \rightarrow {}^3\pi\pi^*$ ISC is forbidden. The value at the MESX 2 was obtained as 11 cm^{-1} for *m*-HMC and 14 cm^{-1} for *o*-HMC, which are larger than MESX 1. However, MESX 2 is located at a much higher energy than MESX 1 (423 and 576 cm^{-1} higher than the ${}^1\pi\pi^*$ EQ of *m*-HMC and *o*-HMC, respectively). The meta-IRC calculation from MESX 2 does not reach the T_4 EQ but a T_4/T_3 MECI. This means that the T_4 state does not have a stable structure along the NRD route but crosses with the T_3 state as the T_4/T_3 MECI at the bottom of the T_4 PES. The MECI is located at 897 and 332 cm^{-1} below the ${}^1\pi\pi^*$ EQ of *m*-HMC and *o*-HMC, respectively. Such a small energy gap means that the density of states, $\rho(E_{\text{ex}})$ of the T_4 state at MESX 2 is not high enough to compete with the route of twisting along the C=C double bond. It should be noted that in both *m*-HMC and *o*-HMC, the equilibrium structure of the T_1 (${}^3\pi\pi^*$) is twisted by 90° with respect to the C=C double bond as seen in Figure 20, similar to *p*-HMC. Thus, it is expected that a similar lifetime to that of *p*-HMC if the T_1 state is produced during the NRD process. Experimentally, the transient state with a lifetime of a few tens of ns was not found, meaning that the T_1 state is not generated in the NRD process of either *m*-HMC or *o*-HMC.

Therefore, it is concluded that the most likely NRD route from the ${}^1\pi\pi^*$ state in *m*- and *o*-HMC is twisting along the propenyl C=C double bond by $\sim 90^\circ$

on the $^1\pi\pi^*$ PES, which is followed by IC to the S_0 state *via* $^1\pi\pi^*/S_0$ CI, leading to either the *cis*-product or a return to the *trans*-form. The onset of the NRD observed in the $^1\pi\pi^*$ lifetime measurement in *m*- and *o*-HMC corresponds to the barrier along the isomerization coordinate in the $^1\pi\pi^*$ state.

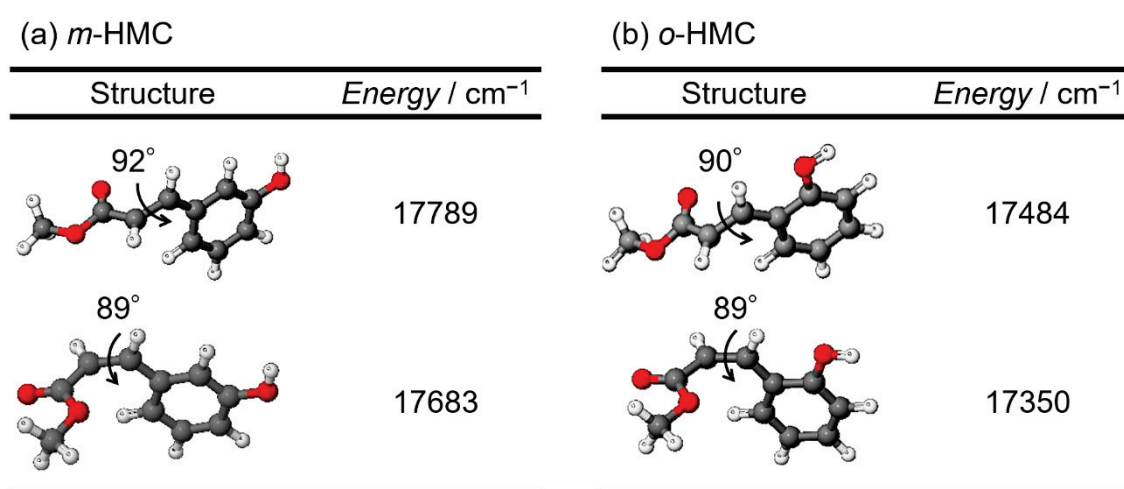


Figure 20 Optimized structures and 0-0 transition energies of (a) *m*-HMC and (b) *o*-HMC in the T_1 state at the $U\omega B97XD/6-311G(d,p)$ level of theory.

4-5 Mechanism of the NRD/photoisomerization route modulation for substituted cinnamates

4-5-1 *p*-HMC and *p*-MMC

In this section, the substitution effect at *para* position on the NRD for cinnamate is described based on the energy of the $^1n\pi^*$ and $^1\pi\pi^*$ state, the molecular orbitals (MOs) related with the $^1n\pi^*$ and $^1\pi\pi^*$ transitions. Finally, the rate constant of $^1\pi\pi^* \rightarrow ^1n\pi^*$ IC is evaluated by Marcus theory.

Table 4 lists the 0-0 transition energies of the $^1\pi\pi^*$ and $^1n\pi^*$ states (E_{0-0} ($^1\pi\pi^*$) and E_{0-0} ($^1n\pi^*$)) calculated at the ω B97XD/6-311G(d,p) level of theory, which are compared to the observed values. Although the calculated energies are roughly 1000 cm^{-1} higher than the observed ones, they show a good agreement for the relative energies of the two states. The calculated results show that the substitution at the *para* position lowers E_{0-0} ($^1\pi\pi^*$) but has less of an effect on E_{0-0} ($^1n\pi^*$). The calculated E_{0-0} ($^1n\pi^*$) values of MC, *p*-HMC and *p*-MMC are located within the range of 420 cm^{-1} , while the energy of the $^1\pi\pi^*$ state is lowered by 1459 cm^{-1} from MC to *p*-MMC, in good agreement with the experimental value of 1632 cm^{-1} . Especially, the order of the two states is reversed between MC and *para*-substituted MCs.

Table 4 Adiabatic energies of the ${}^1\pi\pi^*$ and ${}^1n\pi^*$ states, the ${}^1\pi\pi^*$ lifetimes (τ_1) and major initial NRD routes of MC and substituted MCs.

Molecule	Calc. (ω B97XD/6-311G(d,p))		Obs.			
	$E_{0-0}({}^1\pi\pi^*)$ / cm^{-1}	$E_{0-0}({}^1n\pi^*)$ / cm^{-1}	$E_{0-0}({}^1\pi\pi^*)$ / cm^{-1}	τ_1 / ps	$E_{0-0}({}^1n\pi^*)$ / cm^{-1}	Initial NRD process
MC	34827	34323	33960	4.5 ^a	33300	${}^1\pi\pi^* \rightarrow {}^1n\pi^*$ IC
<i>p</i> -HMC	33697	34692	32710	≤ 10	-	${}^1\pi\pi^* \rightarrow {}^3n\pi^*$ ISC
<i>p</i> -MMC	33368	34743	32328	280	-	${}^1\pi\pi^* \rightarrow {}^3n\pi^*$ ISC
<i>m</i> -HMC	33243	34178	31390	10000	-	C=C bond twisting
<i>o</i> -HMC	32763	34280	31200	6000	-	C=C bond twisting

a) ref. 10

Since the ${}^1\pi\pi^* \rightarrow {}^1n\pi^*$ IC involves the hole transfer from the nonbonding (n) (HOMO–1 or HOMO–2) orbital on carbonyl group to the π (HOMO) orbital as shown in Figure 21, the rate constant of the IC (k_{IC}) can be described approximately by Marcus theory,¹¹

$$k_{\text{IC}} = \frac{2\pi}{\hbar} |H_{1\pi\pi^* - 1n\pi^*}|^2 \frac{1}{\sqrt{4\lambda k_B T}} \exp \left[-\frac{(\lambda + \Delta G_{1\pi\pi^* - 1n\pi^*})^2}{\sqrt{4\lambda k_B T}} \right] \quad (3)$$

where $H_{1\pi\pi^* - 1n\pi^*}$, λ , and $\Delta G_{1\pi\pi^* - 1n\pi^*}$ is the nonadiabatic coupling between the ${}^1\pi\pi^*$ to ${}^1n\pi^*$ states, reorganization energy of the ${}^1n\pi^*$ state, and free energy difference between the ${}^1\pi\pi^*$ and ${}^1n\pi^*$ state, respectively. Under the low

temperature ($T \sim 10$ K) with low-excess energy experimental condition in gas-phase as our previous studies,^{2,4,12-14} the entropy contributions to λ , and $\Delta G_{1\pi\pi^* \rightarrow 1n\pi^*}$ in eq. (3) becomes negligible and is rewritten as the difference of the potential energies,

$$k_{\text{IC}} = \frac{2\pi}{\hbar} |H_{1\pi\pi^* \rightarrow 1n\pi^*}|^2 \frac{1}{\sqrt{4\lambda k_B T}} \exp \left[-\frac{(\lambda + E_{0-0}(1n\pi^*) - E_{0-0}(1\pi\pi^*))^2}{\sqrt{4\lambda k_B T}} \right] \quad (4)$$

Here, λ is approximated by the sum of $|E_{0-0}(1n\pi^*) - E_{0-0}(1\pi\pi^*)|$ and energy difference between $1n\pi^*$ and $1\pi\pi^*$ states $U(1n\pi^* - 1\pi\pi^*)$ at $1\pi\pi^*$ EQ as shown in Figure 22. The effective activation energy E^* for the IC process can be written as

$$\begin{aligned} E^* &\equiv \lambda + E_{0-0}(1n\pi^*) - E_{0-0}(1\pi\pi^*) \\ &\approx U(1n\pi^* - 1\pi\pi^*) + |E_{0-0}(1n\pi^*) - E_{0-0}(1\pi\pi^*)| \\ &\quad + E_{0-0}(1n\pi^*) - E_{0-0}(1\pi\pi^*) \end{aligned} \quad (5)$$

Eq. (5) is further simplified by considering the sign of $E_{0-0}(1n\pi^*) - E_{0-0}(1\pi\pi^*)$. For $E_{0-0}(1n\pi^*) - E_{0-0}(1\pi\pi^*) > 0$,

$$E^* = U(1n\pi^* - 1\pi\pi^*) + 2(E_{0-0}(1n\pi^*) - E_{0-0}(1\pi\pi^*)). \quad (6a)$$

And for $E_{0-0}(1n\pi^*) - E_{0-0}(1\pi\pi^*) \leq 0$,

$$E^* = U(^1n\pi^* - ^1\pi\pi^*). \quad (6b)$$

Eqs. (6a) and (6b) indicate that minimizing $U(^1n\pi^* - ^1\pi\pi^*)$ at $^1\pi\pi^*$ EQ and satisfying $E_{0-0}(^1n\pi^*) - E_{0-0}(^1\pi\pi^*) \leq 0$ is a promising strategy to maximize k_{IC} since λ is almost identical for MC, p -HMC and p -MMC as shown in Table 5. The minimization of $U(^1n\pi^* - ^1\pi\pi^*)$ at $^1\pi\pi^*$ EQ can be achieved by (i) destabilizing $^1\pi\pi^*$ and/or (ii) stabilizing $^1n\pi^*$ state (Figure 22).

Table 5 Parameters for Marcus eqn (4) evaluated at the TD- ω B97XD/6-311G(d,p) level.

Molecule	$U(^1n\pi^* - ^1\pi\pi^*) / \text{cm}^{-1}$	$E_{0-0}(^1n\pi^*) - E_{0-0}(^1\pi\pi^*) / \text{cm}^{-1}$	λ / cm^{-1}
MC	3690	-594	4284
p -HMC	5457	995	4462
p -MMC	5734	1375	4359

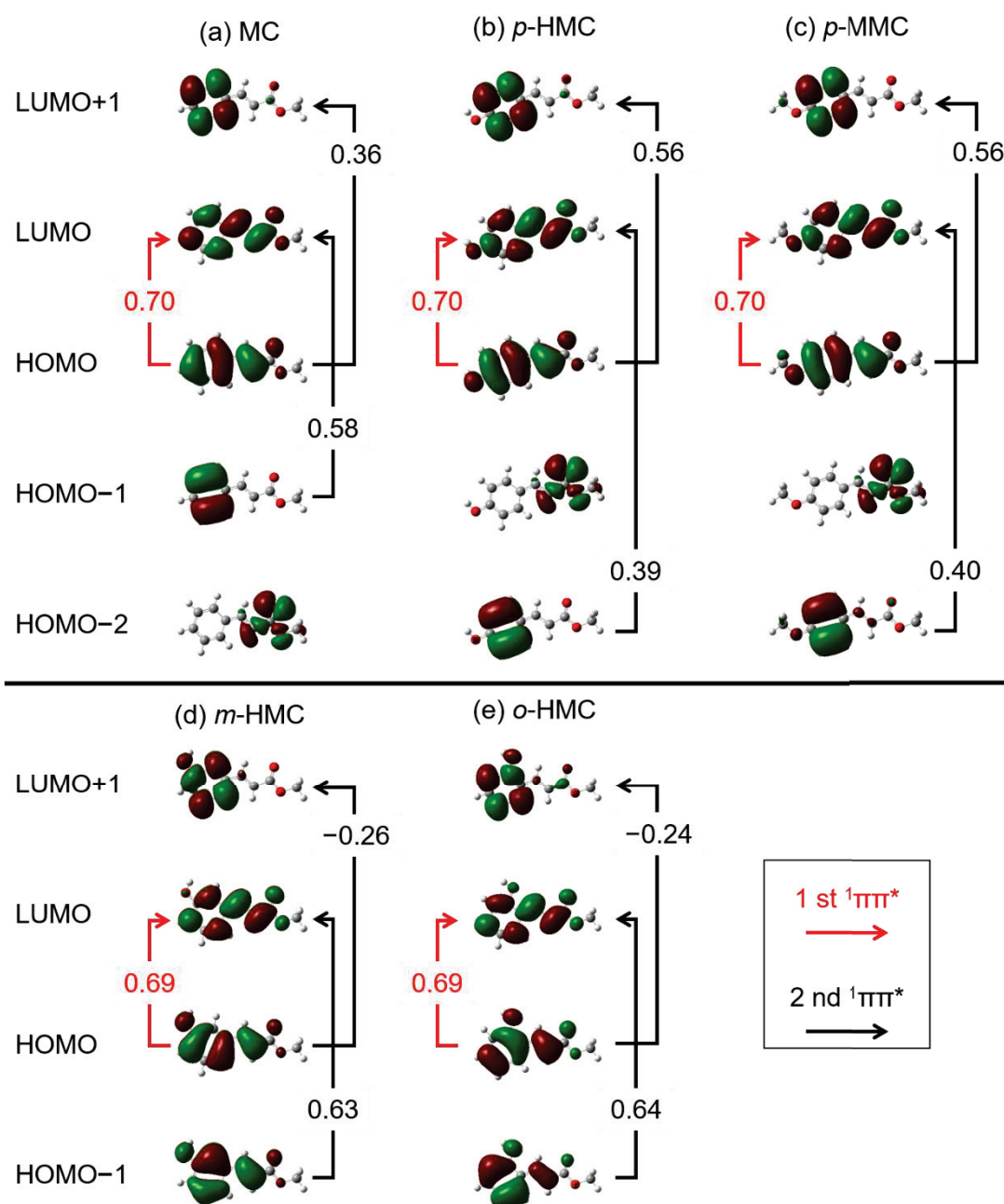


Figure 21 MOs representing ${}^1n\pi^*$ and ${}^1\pi\pi^*$ transitions of (a) MC, (b) *p*-HMC and (c) *p*-MMC. MOs representing two types of ${}^1\pi\pi^*$ transition of (d) *m*- and (e) *o*-HMC. The configuration interaction coefficients obtained by TD- ω B97XD/6-311G(d,p) level of single point calculations at the first ${}^1\pi\pi^*$ EQ for each molecule are also shown.

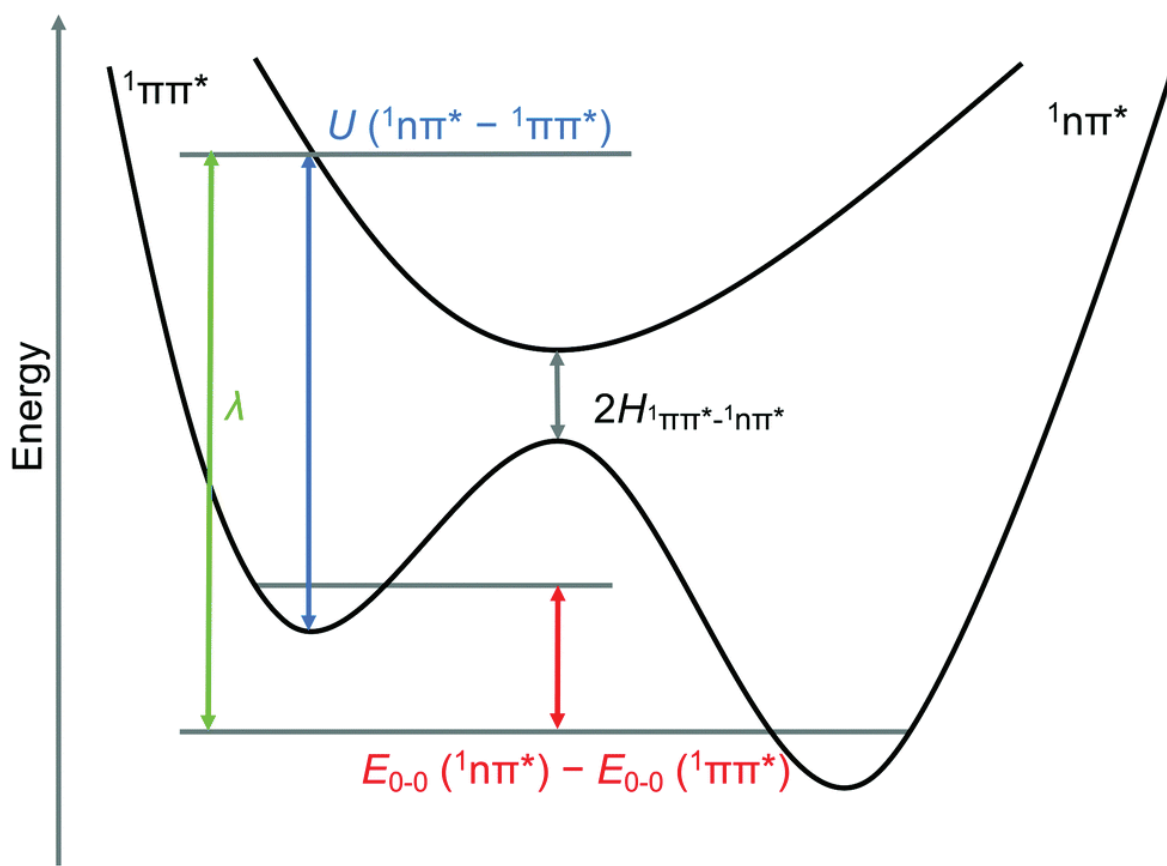


Figure 22 A schematic description of the potential energy curves of MC along the ${}^1\pi\pi^* \rightarrow {}^1n\pi^*$ IC reaction coordinates and the definitions of the parameters appearing in eqn (4).

In order to examine whether (i) or (ii) is the more feasible, the shapes and energies of MOs associated with the ${}^1\pi\pi^*$ and ${}^1n\pi^*$ transitions are carefully looked at. Figure 21 (a)-(c) shows four MOs for MC, *p*-HMC and *p*-MMC, respectively. Table 6 lists the energies of LUMO, HOMO and HOMO-2 or HOMO-1 calculated at the ω B97XD/6-311G(d,p) level of theory at the first ${}^1\pi\pi^*$ EQ by the Gaussian 09 quantum chemistry package.¹⁵ In these cinnamates, the first ${}^1\pi\pi^*$ and

$^1n\pi^*$ transition corresponds to HOMO \rightarrow LUMO and HOMO-2 (or HOMO-1) \rightarrow LUMO transition, respectively. In HOMO of the three molecules, the MO is delocalized on the phenyl ring and vinyl group. It should be noted that the substitution with the OH or OCH₃ group at the *para* position of MC drastically increases the energy of HOMO by 0.5 eV, thus the HOMO-LUMO energy gap of *p*-HMC and *p*-MMC becomes smaller than that of MC. On the other hand, the $^1n\pi^*$ transition energy is less affected by the substitution (within 0.2 eV), since the n orbital on the C=O group is far from the substitution point. These changes result in (i) increasing $U(^1n\pi^*-^1\pi\pi^*)$ at the $^1\pi\pi^*$ EQ and (ii) making the 0-0 energy level of $^1\pi\pi^*$ lower than that of the $^1n\pi^*$ state. As a result, the $^1\pi\pi^* \rightarrow ^1n\pi^*$ IC rate is reduced in *para*-substituted MCs as shown in Table 5 according to Marcus theory, especially in *p*-MMC.

Table 6 Orbital energies of MC, *p*-HMC and *p*-MMC calculated at the ω B97XD/6-311G(d,p) level at the first EQ $^1\pi\pi^*$

Molecule	LUMO (π^*) / eV	HOMO (π) / eV	HOMO-1 or HOMO-2 (n) / eV	ΔE (HOMO- LUMO) / eV	ΔE (HOMO- LUMO) / cm ⁻¹
MC	-0.645	-8.15	-9.68	7.51	60549
<i>p</i> -HMC	-0.350	-7.71	-9.54	7.36	59331
<i>p</i> -MMC	-0.299	-7.62	-9.50	7.32	59024

The modulation of the HOMO (π) energy by introducing the substituent is explained by applying Hammett's rule.¹⁶ The correlation between the HOMO energy of the substituted benzene and Hammett's parameter was already estimated.^{17,18} The plots of the HOMO energy against the σ parameters for various substitution groups showed a good correlation. According to those plots, the HOMO of benzene is destabilized by π -donor substitution such as the OH and OCH₃ groups. In addition, the HOMO–LUMO transition energy is described by three types of Hammett parameter: σ_I , σ_{π}^+ and σ_{π}^- .¹⁹ Here, σ_I is the inductive substituent constant, while σ_{π}^+ and σ_{π}^- are the π -electronic substituent constants for π -donor and π -accepter substituent, respectively. These values for H, OH and OCH₃ groups are listed in Table 7. For example, the transition energy from the S₀ state to the ¹ $\pi\pi^*$ state, E^{UV} (eV) for monosubstituted benzene is described as:²⁰

$$E^{UV} = -0.021\sigma_I + 1.194\sigma_{\pi}^+ - 1.029\sigma_{\pi}^- + 4.846 . \quad (7)$$

The calculated and observed E^{UV} of non-substituted benzene, phenol and anisole are also listed in Table 7.¹⁹⁻²³ This calculated E^{UV} trend is consistent with experimental values, thus it can also be applied to cinnamates.

Table 7 Values of σ_I , σ_{π}^+ and σ_{π}^- for H, OH, OCH₃ groups and calculated and observed E^{UV} (cm⁻¹) of the S₀ → ¹ππ* transition of benzene derivatives. Here, the 0-0 transition of benzene is forbidden, thus the experimentally predicted value is listed.

Substitution					Calc.	Obs..
	σ_I	σ_{π}^+	σ_{π}^-	E^{UV} / eV	E^{UV} / cm ⁻¹	E^{UV} / cm ⁻¹
H (benzene) ^{a,b,c}	0	0	0	4.85	39086	38086
OH (phenol) ^{a,b,d}	0.190	-0.340	0	4.44	35779	36348
OCH ₃ (anisole) ^{a,b,e}	0.185	-0.281	0	4.51	36348	36384

a) ref. 19, b) ref. 20, c) ref. 21, d) ref. 22, e) ref. 23

The experimental results reported in previous studies support the calculated results. The observed E_{0-0} (¹ππ*) and E_{0-0} (¹nπ*) and the ¹ππ* lifetime (τ_1) are also listed in Table 4. In the case of MC, the 0-0 transitions of the ¹nπ* and ¹ππ* states is observed at 33300 cm⁻¹ and 33960 cm⁻¹, respectively. The observed E_{0-0} (¹nπ*) is located 660 cm⁻¹ lower than that of the ¹ππ* state. On the other hand, in neither *p*-HMC nor *p*-MMC, the ¹nπ* state was observed. This is because E_{0-0} (¹nπ*) of *p*-HMC and *p*-MMC is higher than E_{0-0} (¹ππ*) in those species. As indicated by the calculated values, the transition to this state is overlapped with the vibronic bands of the bright ¹ππ* state, thus it is hard to discriminate it. The measured ¹ππ* lifetime at the 0-0 band (τ_1) of *p*-MMC is much longer than that of both MC and *p*-HMC. The longer ¹ππ* lifetime of *p*-MMC is explained by its

larger ${}^1\pi\pi^* - {}^1n\pi^*$ energy gap.²

The energy difference between the ${}^1\pi\pi^*$ and ${}^1n\pi^*$ states changes the rate of the IC and activates another multistep ISC pathway such as “ ${}^1\pi\pi^*$ (*trans*) \rightarrow T₂ (${}^3n\pi^*$) \rightarrow T₁ (${}^3\pi\pi^*$) \rightarrow S₀ (*trans* or *cis*)” as suggested by previous study on *p*-MMC.^{3,24} Different from MC, the ${}^3n\pi^*$ state of *p*-HMC and *p*-MMC is located at much higher energy (~ 3000 cm⁻¹) above the ${}^1\pi\pi^*$ EQ and below the ${}^1n\pi^*$ EQ as shown in Table 8. For MC, it satisfies $E_{0-0}({}^1\pi\pi^*) > E_{0-0}({}^1n\pi^*)$ as shown in Table 4 and fast ${}^1\pi\pi^* \rightarrow {}^1n\pi^*$ IC within 10 ps is the major initial process of the multistep ISC. Population of the ${}^1n\pi^*$ state is large enough for direct detection by our ps UV-UV’ pump probe measurement.

Table 8 Vertical transition energies in cm^{-1} of (a) MC, (b) *p*-HMC and (c) *p*-MMC) at the $^1\pi\pi^*$ EQ calculated at $\omega\text{B97XD}/6\text{-}311\text{G(d,p)}$ level. Characters of their transitions are also listed.

(a) MC			(b) <i>p</i> -HMC		
State	Character	<i>Energy</i> / cm^{-1}	State	Character	<i>Energy</i> / cm^{-1}
T ₁	$\pi\pi^*$	14026	T ₁	$\pi\pi^*$	14673
T ₂	$\pi\pi^*$	31259	T ₂	$\pi\pi^*$	31494
T ₃	$\pi\pi^*$	33183	T ₃	$\pi\pi^*$	33021
T ₄	$n\pi^*$	33632	T ₄	$n\pi^*$	34650
T ₅	$\pi\pi^*$	38174	T ₅	$\pi\pi^*$	36002
S ₁	$\pi\pi^*$	32605	S ₁	$\pi\pi^*$	31879
S ₂	$n\pi^*$	36295	S ₂	$n\pi^*$	37336
S ₃	$\pi\pi^*$	38322	S ₃	$\pi\pi^*$	38289

(c) <i>p</i> -MMC		
State	Character	<i>Energy</i> / cm^{-1}
T ₁	$\pi\pi^*$	14819
T ₂	$\pi\pi^*$	31609
T ₃	$\pi\pi^*$	33108
T ₄	$n\pi^*$	34729
T ₅	$\pi\pi^*$	35864
S ₁	$\pi\pi^*$	31691
S ₂	$n\pi^*$	37425
S ₃	$\pi\pi^*$	38242

However, E_{0-0} ($^1\pi\pi^*$) of p -HMC and p -MMC is lower than E_{0-0} ($^1n\pi^*$). This switches the major NRD route to $^1\pi\pi^* \rightarrow ^3n\pi^*$ ISC on the time scale of ps, and only the $^3\pi\pi^*$ (T_1) state becomes experimentally observable in p -HMC and p -MMC. The $^1\pi\pi^*$ lifetime of p -HMC and p -MMC should be also affected by the height of $^1\pi\pi^*/^3n\pi^*$ MESX, the SOC between the $^1\pi\pi^*$ and $^3n\pi^*$ states, and the vibrational density of states of the $^3n\pi^*$ state. The strategy derived from Marcus theory discussed for $^1\pi\pi^* \rightarrow ^1n\pi^*$ IC can also be helpful for improving efficiency of $^1\pi\pi^* \rightarrow ^3n\pi^*$ ISC, which also involves hole transfer from carbonyl group to phenyl ring.²⁵

For further investigation on the substitution effects on the initial step of multistep ISC and subsequent isomerization dynamics, the interplay between pump-probe spectroscopies, such as time-resolved photoelectron spectroscopy^{10,26} and transient absorption spectroscopy,¹⁰ and nonadiabatic reaction dynamics and spectroscopic studies based on highly accurate wave function-based electronic structure methods²⁷ (e.g. MS-CASPT2 using large active space,²⁴ EOM-CCSD, or ADC(3) combined with aug-cc-pVTZ or larger basis set) are desirable.²⁸ Especially, the $T_1 \rightarrow T_n$ transient absorption combined with UV-DUV pump-probe spectroscopy with the aid of *ab initio* calculations for the $T_1 \rightarrow T_n$ absorption will give us complementary information for the T_1 state. Another method is the observation of the vibrational spectrum of the T_1 state combined with UV-DUV pump-probe spectroscopy, which was demonstrated for the study of the NRD for thymine by Boldissar *et al.*²⁹

The effect at *para*-substitution on the NRD for cinnamates is summarized in this paragraph. The substitution with OH or OCH₃ group at the *para* position of MC slightly lowers the ¹ππ* transition energy and prolongs the ¹ππ* lifetime, however triplet mediated isomerization process is still dominant. The ¹ππ* lifetime of *para*-substituted cinnamates is also very short meaning an efficient initial NRD (¹ππ* → ¹nπ* and/or ¹ππ* → ³nπ*). This suggests that *para*-substituted cinnamates can be good UV filters if they effectively go back to the S₀ state or isomerize to the *cis* (*Z*) isomer with high yields. Figure 23 shows the schematic potential curves of the electronic states along the photoisomerization coordinate for (a) MC and for (b) *p*-HMC and *p*-MMC.

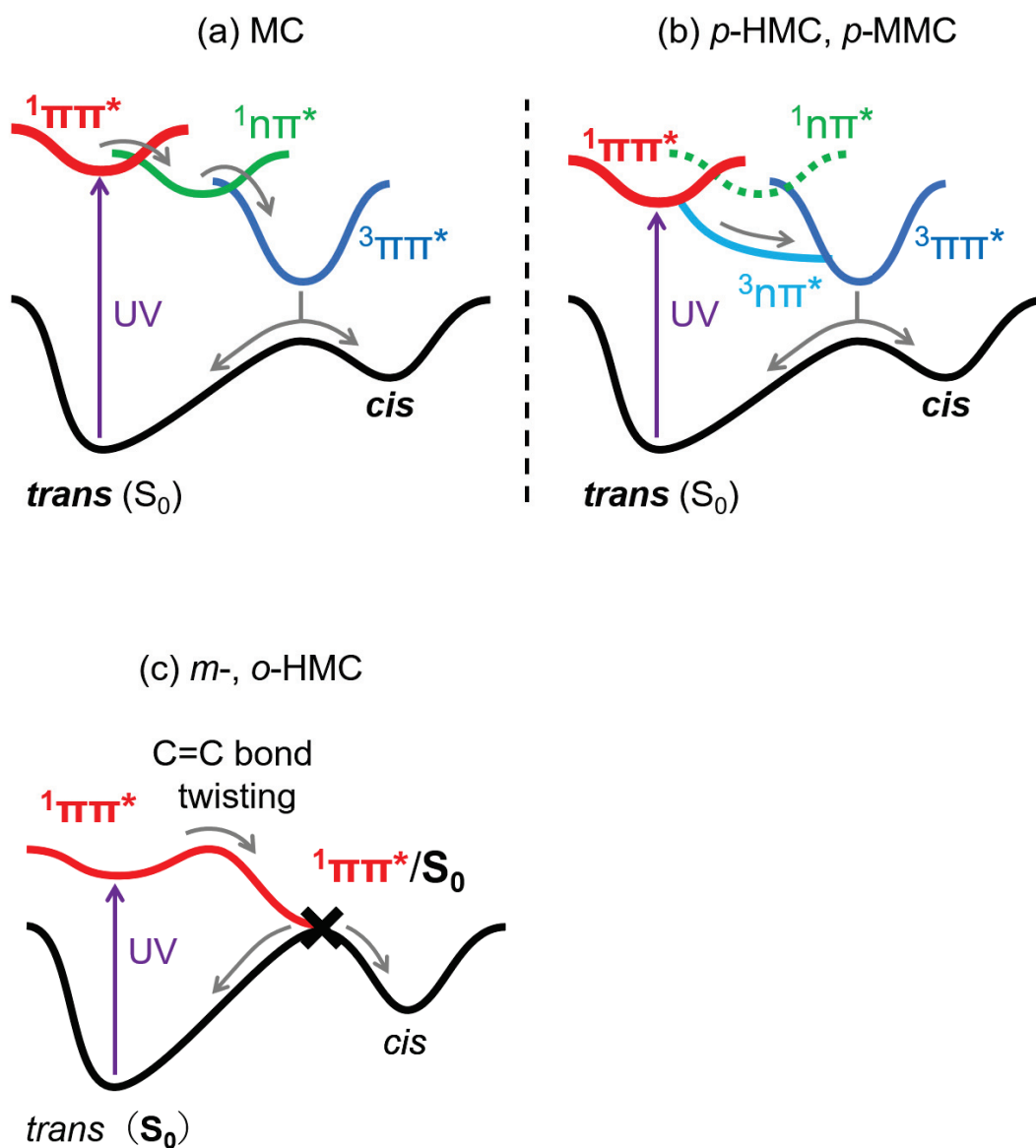


Figure 23 Schematic potential curves of the electronic states along the photoisomerization coordinate for (a) MC, (b) *p*-HMC and *p*-MMC and (c) *m*-HMC and *o*-HMC. In the routes of (a) and (b), the transient T_1 ($^3\pi\pi^*$) is mediated. On the other hand, in the (c) route, the isomerization occurs on the $^1\pi\pi^*$ state.

4-5-2 *m*-HMC and *o*-HMC

The previous pump-probe measurement and the systematic exploration of the NRD/photoisomerization route revealed that the substitution of the OH group at *meta* or *ortho* position of the phenyl ring in MC changes the dominant NRD/photoisomerization route to the C=C bond twisting on the ${}^1\pi\pi^*$ PES described as " ${}^1\pi\pi^*$ (*trans*) \rightarrow C=C bond twisting on ${}^1\pi\pi^*$ PES \rightarrow S_0 (*trans* or *cis*)". In this section, the mechanism of the modulation for the NRD/photoisomerization route is investigated based on the molecular symmetry and the energy of the ${}^1n\pi^*$ and ${}^1\pi\pi^*$ state. Finally, in later part, a guideline for a development cinnamate-based sunscreen is provided.

As discussed in Section 3-6 for MC, the first and second ${}^1\pi\pi^*$ states of cinnamates originate from several $\pi \rightarrow \pi^*$ configurations such as HOMO (π) \rightarrow LUMO (π^*), HOMO-1 (π) \rightarrow LUMO (π^*) and HOMO (π) \rightarrow LUMO+1 (π^*) where the weight of these configuration is different in the first and second ${}^1\pi\pi^*$ states as shown in Table 9. The shape of MOs is summarized in Figure 21. The energies of the first and second ${}^1\pi\pi^*$ states depend on the substitution position due to the different strength of configuration interaction between them.⁷ As a result, although splitting of the first and second ${}^1\pi\pi^*$ states is small in MC and *p*-HMC, the energy level of first ${}^1\pi\pi^*$ state of *m*- and *o*-HMC becomes significantly lower than that of MC. As seen in Table 4, the calculated E_{0-0} (${}^1\pi\pi^*$) of *m*- and *o*-HMC is lower than that of MC and *para*-substituted MCs. This is in accordance with the observed E_{0-0} (${}^1\pi\pi^*$) of *m*- and *o*-HMC to be 2570 and 2760 cm^{-1} lower than that of MC, respectively, and more than 1000 cm^{-1} lower than that of *para*-

substituted MCs. The magnitude of the lowering of the calculated ${}^1\pi\pi^*$ transition energy seems to be underestimated for *m*- and *o*-HMC. The calculated E_{0-0} (${}^1\pi\pi^*$) of *m*- and *o*-HMC is not drastically changed compared to E_{0-0} (${}^1\pi\pi^*$), being almost the same as those of MC and *para*-substituted MCs (Table 4).

Table 9 Major electron configurations of the first and second ${}^1\pi\pi^*$ states for MC, *p*-HMC, *p*-MMC, *m*-HMC and *o*-HMC calculated at the ω B97XD/6-311G(d,p) level at the ${}^1\pi\pi^*$ EQ of each molecule.

Molecule	Electron configuration	
	first ${}^1\pi\pi^*$	second ${}^1\pi\pi^*$
MC	0.70 HOMO→LUMO	0.58 HOMO-1→LUMO 0.36 HOMO→LUMO+1
<i>p</i> -HMC	0.70 HOMO→LUMO	0.39 HOMO-2→LUMO 0.56 HOMO→LUMO+1
<i>p</i> -MMC	0.70 HOMO→LUMO	0.40 HOMO-2→LUMO 0.56 HOMO→LUMO+1
<i>m</i> -HMC	0.69 HOMO→LUMO	0.63 HOMO-1→LUMO -0.26 HOMO→LUMO+1
<i>o</i> -HMC	0.69 HOMO→LUMO	0.64 HOMO-1→LUMO -0.24 HOMO→LUMO+1

The mixture of HOMO (π) \rightarrow LUMO (π^*), HOMO-1 (π) \rightarrow LUMO (π^*) and HOMO (π) \rightarrow LUMO+1 (π^*) transitions is characteristic of the electronic states in *meta*- or *ortho*-disubstituted benzene. The reduction of symmetry causes extensive configuration interaction between pure transitions. The interaction results in the larger splitting of the energy level of the first $^1\pi\pi^*$ and second $^1\pi\pi^*$ state, where the splitting for *ortho* is slightly larger than that for *meta*. Same patterns of the two $^1\pi\pi^*$ transitions and MOs were also reported for the structural isomers of HMC and other cinnamates by using SAC-CI method, and two distinct $^1\pi\pi^*$ transitions were observed in the absorption spectra of *meta*- and *ortho*-cinnamate derivatives and aminostilbene.^{7,30-32} As another example, it was reported that the 0-0 transitions of jet-cooled *meta*- and *ortho*-diethynylbenzene appear at lower energy than that of the *para* isomer.³³

The substitution effect at *meta* or *ortho* position on the NRD/photoisomerization route is summarized in this paragraph. The substitution of the OH group at *meta* or *ortho* position of the phenyl ring in MC further lowers the $^1\pi\pi^*$ transition energy and drastically prolongs the $^1\pi\pi^*$ lifetime, indicating the inhibition of the $^1\pi\pi^* \rightarrow ^1n\pi^*$ IC and $^1\pi\pi^* \rightarrow ^3n\pi^*$ ISC routes due to their larger energy barrier than that of MC and *para*-substituted MCs. As a result, the dominant NRD/photoisomerization route is changed to the C=C bond twisting on the $^1\pi\pi^*$ PES described as " $^1\pi\pi^*$ (*trans*) \rightarrow C=C bond twisting on $^1\pi\pi^*$ PES \rightarrow S₀ (*trans* or *cis*)" shown in Figure 23 (c).

From view point of a guideline for designing an effective sunscreen, it is

found that for efficient IC from the ${}^1\pi\pi^*$ state, the cinnamate should have an appropriate substituent at the phenyl ring to stabilize the highest occupied π orbital. The stabilized π orbital (i) minimizes the energy gap between ${}^1\pi\pi^*$ and ${}^1n\pi^*$ at the ${}^1\pi\pi^*$ EQ and (ii) makes the 0-0 energy level of the ${}^1\pi\pi^*$ state higher than that of the ${}^1n\pi^*$ state as observed in MC. These MC-like energetic relationships between the ${}^1\pi\pi^*$ and ${}^1n\pi^*$ states should be ideal to maximize the ${}^1\pi\pi^* \rightarrow {}^1n\pi^*$ IC rate constant according to the Marcus theory.

4-6 Conclusion

The substitution and its position effect on the electronic states and the NRD/photoisomerization of cinnamates was examined focusing on the relationship between the experimentally observed lifetime, energy of the $^1\pi\pi^*$ and $^1n\pi^*$ state and the MOs related to the $^1\pi\pi^*$ and $^1n\pi^*$ transitions.

The cold matrix-isolation FTIR spectroscopy showed that all of the structural isomers of HMC and *p*-MMC exhibit *trans* \rightarrow *cis* photoisomerization upon the UV irradiation. However, the isomerization requires some excess energy ($\sim 2000\text{ cm}^{-1}$) to occur in *o*-HMC and *m*-HMC.

The $^1\pi\pi^*$ lifetime at 0-0 band of *p*-HMC and *p*-MMC was measured to be equal to or shorter than 9 ps and 280 ps, respectively. The similar T_1 state to MC was also detected in *p*-HMC and *p*-MMC. The substitution at *para* position destabilizes HOMO (π) and lowers the energy of the $^1\pi\pi^*$ state of MC, therefore the order of $^1\pi\pi^*$ and $^1n\pi^*$ states is reversed between MC and *para*-substituted MCs. This energy inversion increases the contribution of another sub ns NRD route involving the T_1 state: $^1\pi\pi^*$ (*trans*) \rightarrow $^3n\pi^*$ \rightarrow $^3\pi\pi^*$ \rightarrow S_0 (*trans* or *cis*).

On the other hand, the $^1\pi\pi^*$ lifetime of *m*- and *o*-HMC was measured to be 10 ns and 6 ns, respectively. These lifetimes are much longer than those of MC and its *para*-substituted MCs. The $^1\pi\pi^*$ decay rate constant of *m*- and *o*-HMC clearly shows an onset of the fast NRD channel at $\sim 1000\text{ cm}^{-1}$ and $\sim 600\text{ cm}^{-1}$ above the 0-0 band. Different from MC and *para*-substituted MCs, the T_1 state was not detected in *m*- and *o*-HMC. For these cinnamates, the energy level of the $^1\pi\pi^*$ state is more significantly lowered, and the energy barrier of $^1\pi\pi^* \rightarrow ^1n\pi^*$

IC becomes very high. Thus, the direct isomerization process of the C=C bond twisting on the $^1\pi\pi^*$ PES is thought to be the dominant route, described as “ $^1\pi\pi^*$ (*trans*) \rightarrow C=C bond twisting on the $^1\pi\pi^*$ PES \rightarrow S₀ (*trans* or *cis*)”. Actually, the AFIR/TD-DFT calculation showed that the energy barrier on the direct isomerization route agrees with the experimental value in both of *m*- and *o*-HMC.

This study systematically analyzed the substitution effect on the electronic states and the NRD/photoisomerization route of cinnamate derivatives with a substituent at the phenyl ring, and revealed that *para*-substituted cinnamates can be the most effective sunscreen reagents because the multistep NRD process can rapidly convert harmful absorbed UV energy to safer thermal energy.

References

1. E. M. M. Tan, S. Amirjalayer, S. Smolarek, A. Vdovin, A. M. Rijs and W. J. Buma, *J. Phys. Chem. B*, 2013, **117**, 4798-4805.
2. Y. Miyazaki, K. Yamamoto, J. Aoki, T. Ikeda, Y. Inokuchi, M. Ehara and T. Ebata, *J. Chem. Phys.*, 2014, **141**, 244313.
3. K. Yamazaki, Y. Miyazaki, Y. Harabuchi, T. Taketsugu, S. Maeda, Y. Inokuchi, S. Kinoshita, M. Sumida, Y. Onitsuka, H. Kohguchi, M. Ehara and T. Ebata, *J. Phys. Chem. Lett.*, 2016, **7**, 4001-4007.
4. D. Shimada, R. Kusaka, Y. Inokuchi, M. Ehara and T. Ebata, *Phys. Chem. Chem. Phys.*, 2012, **14**, 8999-9005.
5. E. M. M. Tan, S. Amirjalayer, B. H. Bakker and W. J. Buma, *Faraday Discuss.*, 2013, **163**, 321-340.
6. Y. Miyazaki, Y. Inokuchi, N. Akai and T. Ebata, *J. Phys. Chem. Lett.*, 2015, **6**, 1134-1139.
7. M. Promkatkaew, S. Suramitr, T. Karpkird, S. Wanichwecharungruang, M. Ehara and S. Hannongbua, *Photochem. Photobiol. Sci.*, 2014, **13**, 583-594.
8. C. M. Marian, *Comput. Mol. Sci.*, 2012, **2**, 187-203.
9. M. A. El-Sayed, *J. Chem. Phys.*, 1963, **38**, 2834.
10. K. M. Krokidi, M. A. P. Turner, P. A. J. Percy and V. G. Stavros, *Mol. Phys.*, 2020, DOI: 10.1080/00268976.2020.1811910.
11. R. A. Marcus, *Angew. Chem. Int. Ed. Engl.*, 1993, **32**, 1111-1121.
12. S. Kenjo, Y. Iida, N. Chaki, S. Kinoshita, Y. Inokuchi, K. Yamazaki and T. Ebata, *Chem. Phys.*, 2018, **515**, 381-386.
13. S. Muramatsu, S. Nakayama, S. Kinoshita, Y. Onitsuka, H. Kohguchi, Y. Inokuchi, C. Zhu and T. Ebata, *J. Phys. Chem. A*, 2020, **124**, 1272-1278.
14. Y. Iida, S. Kinoshita, S. Kenjo, S. Muramatsu, Y. Inokuchi, C. Zhu and T. Ebata, *J. Phys. Chem. A*, 2020, **124**, 5580-5589.
15. M. J. Frisch, G. W. Trucks, H. B. Schlegel, G. E. Scuseria, M. A. Robb, J. R. Cheeseman, G. Scalmani, V. Barone, B. Mennucci, G. A. Petersson, H. Nakatsuji, M. Caricato, X. Li, H. P. Hratchian, A. F. Izmaylov, J. Bloino, G. Zheng, J. L. Sonnenberg, M. Hada, M. Ehara, K. Toyota, R. Fukuda, J. Hasegawa, M. Ishida, T. Nakajima, Y. Honda, O. Kitao, H. Nakai, T. Vreven, J. A. Montgomery, J. E. Peralta, F. Ogliaro, M. Bearpark, J. J. Heyd, E. Brothers, K. N. Kudin, V. N. Staroverov, T. Keith, R. Kobayashi, J. Normand, K. Raghavachari, A. Rendell, J. C. Burant, S. S.

- Iyengar, J. Tomasi, M. Cossi, N. Rega, J. M. Millam, M. Klene, J. E. Knox, J. B. Cross, V. Bakken, C. Adamo, J. Jaramillo, R. Gomperts, R. E. Stratmann, O. Yazyev, A. J. Austin, R. Cammi, C. Pomelli, J. W. Ochterski, R. L. Martin, K. Morokuma, V. G. Zakrzewski, G. A. Voth, P. Salvador, J. J. Dannenberg, S. Dapprich, A. D. Daniels, O. Farkas, J. B. Foresman, J. V. Ortiz, J. Cioslowski and D. J. Fox, Gaussian 09, Revision D.01, Gaussian, Inc., Wallingford CT, 2013.
16. C. Hansch, A. Leo and R. W. Taft *Chem. Rev.*, 1991, **91**, 165-195.
 17. H. Fujimoto, K. Sakata and K. Fukui, *Int. J. Quantum Chem.*, 1996, **60**, 401-408.
 18. O. Henri-Rousseau and F. Texier, *J. Chem. Educ.*, 1978, **55**, 437-441.
 19. M. Sawada, M. Ichimura, Y. Yukawa, T. Nakachi and Y. Tsuno, *Bull. Chem. Soc. Jpn.*, 1980, **53**, 2055-2060.
 20. B. Uno and T. Kubota, *J. Chem. Soc. Jpn.*, 1991, **2**, 101-109.
 21. R. H. Page, Y. R. Shen and Y. T. Lee, *J. Chem. Phys.*, 1988, **88**, 5362.
 22. T. Ebata, N. Mizuochi, T. Watanabe and N. Mikami *J. Phys. Chem.*, 1996, **100**, 546-550.
 23. R. Matsumoto, K. Sakeda, Y. Matsushita, T. Suzuki and T. Ichimura, *J. Mol. Struct.*, 2005, **153**, 735-736.
 24. J. Moon, H. Baek, J. S. Lim and J. Kim, *Bull. Korean Chem. Soc.*, 2018, **39**, 427-434.
 25. N. Aizawa, Y. Harabuchi, S. Maeda and Y.-J. Pu, *Nat. Commun.*, 2020, **11**, 3909.
 26. T. Horio, Y. Suzuki and T. Suzuki, *J. Chem. Phys.*, 2016, **145**, 044307.
 27. S. Mai and L. Gonzalez, *Angew. Chem., Int. Ed.*, 2020, **59**, 16832-16846.
 28. S. Pathak et al., *Nat. Chem.*, 2020, **12**, 795-800.
 29. S. Boldissar and M. S. de Vires, *Phys. Chem. Chem. Phys.*, 2018, **20**, 9701-9716.
 30. M. Promkatkaew, S. Suramitr, T. M. Karpkird, S. Namuangruk, M. Ehara and S. Hannongbua, *J. Chem. Phys.*, 2009, **131**, 224306.
 31. T. M. Karpkird, S. Wanichweacharungruang and B. Lbinsson, *Photochem. Photobiol. Sci.*, 2009, **8**, 1455-1460.
 32. F. D. Lewis, R. S. Kalgutkar and J.-S. Yang, *J. Am. Chem. Soc.*, 1999, **121**, 12045-12053.
 33. J. A. Stearns and T. S. Zwier, *J. Phys. Chem. A*, 2003, **107**, 10717-10724.

Chapter 5

Hydrogen-bonding effect on electronic states and nonradiative decay process of cinnamates

5-1 Electronic spectra and assignment of the electronic states

The effect of Hydrogen (H)-bonding on the electronic states and nonradiative decay (NRD) process of methylcinnamate (MC) was investigated. Under the jet-cooled condition, the electronic spectrum for the 1:1 cluster of MC with a methanol molecule (MC-MeOH) was measured by laser induced fluorescence (LIF) and two-color resonance two photon ionization (2C-R2PI) method. The micro solvated cluster was generated by mixing a methanol vapor with a carrier gas.

Figure 1 (a) and (b) represents electronic spectrum measured by LIF method for bare MC and MC-MeOH, respectively. Figure (c) and (d) represents electronic spectrum measured by 2C-R2PI method for bare MC and MC-MeOH, respectively. Here, the frequency of the ionization laser (ν_2) was fixed to 48600 cm^{-1} (205.75 nm) in both measurements. Under the high ν_2 condition, an extensive fragmentation will occur after the ionization of MC-MeOH, thus in Figure 1 (d), the ion signal of MC^+ due to both of bare MC and fragment from MC-MeOH was

monitored. In Figure 1 (b), the new vibronic bands with the origin of band A' (33220 cm^{-1}), which is red-shifted by 70 cm^{-1} from band A, appear. In both of Figure 1 (b) and (d), a new band C' (33720 cm^{-1}), which is red-shifted by 230 cm^{-1} from band C ($^1\pi\pi^*$), strongly appears.

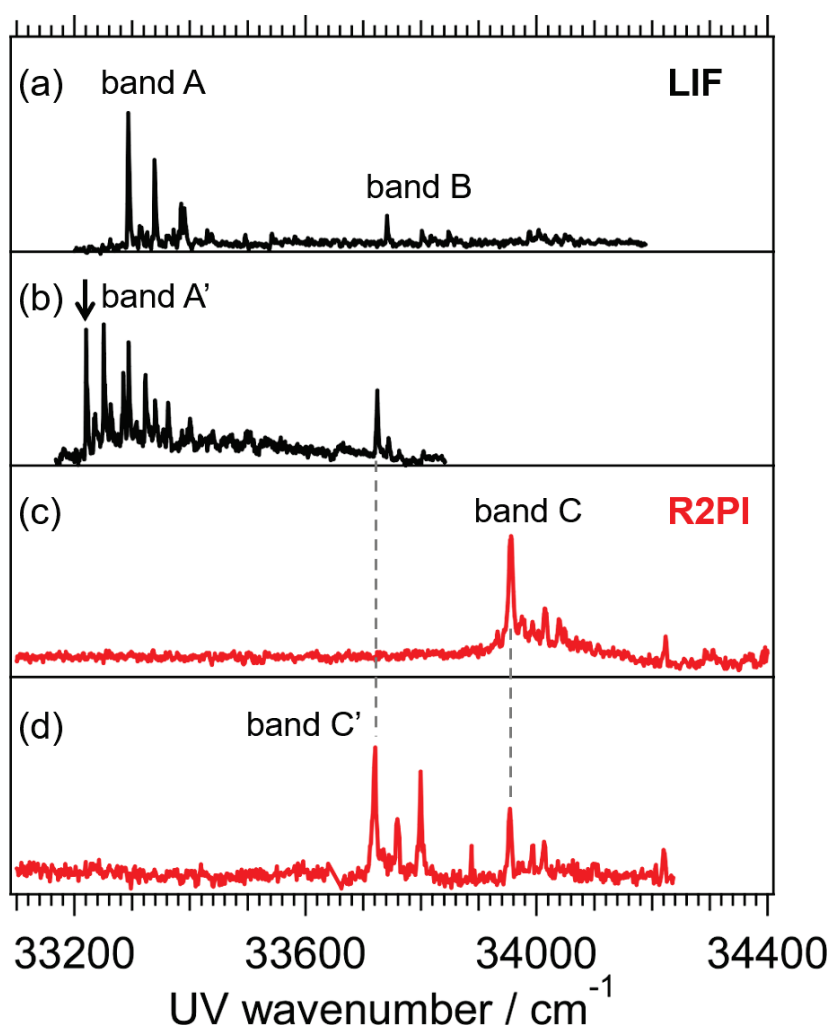


Figure 1 Electronic spectra of jet-cooled (a) bare MC and (b) MC-MeOH measured by LIF method. Electronic spectra of jet-cooled (c) bare MC and (d) MC-MeOH measured by 2C-R2PI method, fixing the ν_2 to 48600 cm^{-1} (205.75 nm).

band A' was not observed in the Figure 1 (d), indicating an ionization energy of band A' is thought to be very high. Thus, as the case of MC (see Section 3-2), the band can be assigned to the origin of the ${}^1n\pi^*$ transition. Figure 2 shows the optimized structures of the *trans/cis* (TC) and *trans/trans* (TT) conformer (see Figure 2 in Chapter 3) for MC-MeOH and their relative energies in the S_0 state calculated at the ω B97XD/6-311G(d,p) level. The length of the H-bond between OH group in methanol and C=O group in MC are also shown in unit of Å. It is found that the TC conformer is more stable by 491 cm^{-1} than the TT conformer in the S_0 state.

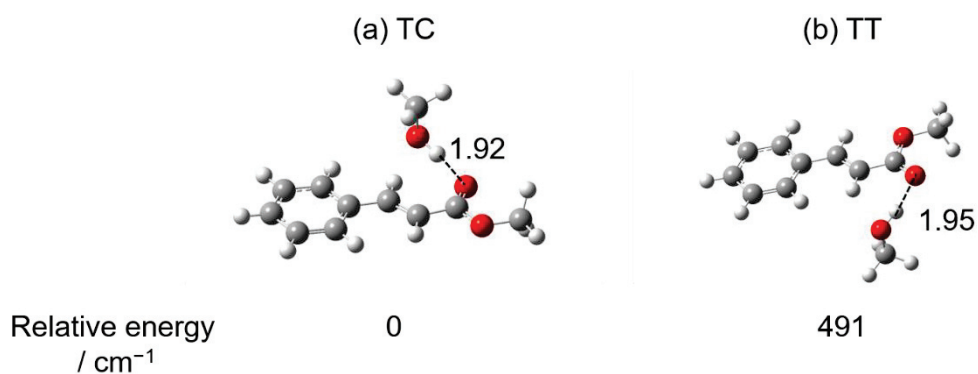


Figure 2 Optimized structures of the (a) TC and (b) TT conformers for MC-MeOH and their relative energies in the S_0 state calculated at the ω B97XD/6-311G(d,p) level. The length of the H-bond between OH group in methanol and C=O group in MC are also shown in unit of Å.

For the assignment of band C', the ionization energy was estimated. Figure 3 (a) shows the ionization efficiency curve from band C'. Here, the frequency of the pump laser (ν_1) was fixed to 33720 cm^{-1} (band C') and the ν_2 was scanned. An ionization threshold is seen at $\nu_2 = 35200 \text{ cm}^{-1}$, estimating the ionization potential (D_0) becomes to be 68920 cm^{-1} . The calculated D_0 energy is 66230 cm^{-1} and reasonably agrees with the observed one (68920 cm^{-1}). In addition that, the value of red-shift is similar to that of the 1:1 cluster of *para*-methoxy MC with a water molecule (*p*-MMC- H_2O). In ref. 1, it was reported that the H-bonding to C=O group red-shifts the $^1\pi\pi^*$ transition of bare *p*-MMC by $\sim 200 \text{ cm}^{-1}$. Thus, band C' can be assigned to origin of the $^1\pi\pi^*$ transition. The energy diagram of the $^1n\pi^*$ and $^1\pi\pi^*$ states is shown in Figure 3 (b). The reason for the appearance of band C' ($^1\pi\pi^*$) in the Figure 1 (b) will be discussed in Section 5-2.

The observed D_0 value is lower than that of MC (69090 cm^{-1}) by 170 cm^{-1} . A rather small difference of the D_0 values between them can be explained as follows. It is expected that as shown in Figure 2, OH group in methanol is bonded to the lone-pair electron of the C=O group in MC as a proton donor, while the ionization is the removal of the π -electron of the phenyl group, thus the H-bonding to C=O group will less affect the ionization process.

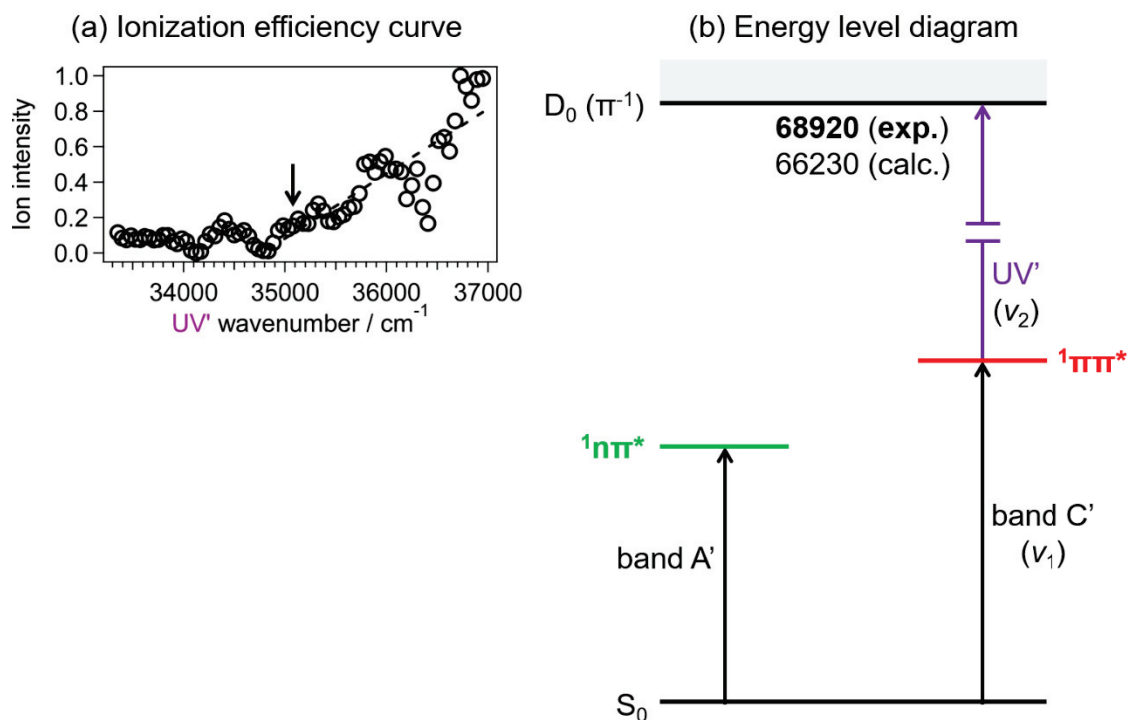


Figure 3 (a) Ionization efficiency curve from band C'. The arrow indicates the ionization threshold. (b) Energy level diagram of bands A' and C' in unit of cm⁻¹.

5-2 H-bonding effect on the NRD process

In order to investigate the H-bonding effect on the NRD process, the lifetime of the $^1n\pi^*$ and $^1\pi\pi^*$ state was measured by various spectroscopic techniques.

At first, the NRD process from the $^1n\pi^*$ state was investigated. Figure 4 shows the fluorescence decay curves of the $^1n\pi^*$ state at (a) band A' (0-0), (b) band A' + 30 cm^{-1} , (c) band A' + 64 cm^{-1} , (d) band A' + 103 cm^{-1} , (e) band A' + 141 cm^{-1} and (f) band C'(0-0). The $^1n\pi^*$ lifetime at the 0-0 band (band A') was measured as 7.0 ns and is almost same with that of the bare (band A) however, the lifetimes show little excess energy dependence. In fact, the lifetime of vibronic band at $\sim 140 \text{ cm}^{-1}$ above the 0-0 band is still long enough to be measured. This result suggests that the H-bonding to the C=O group suppresses the $^1n\pi^* \rightarrow$ triplet intersystem crossing.

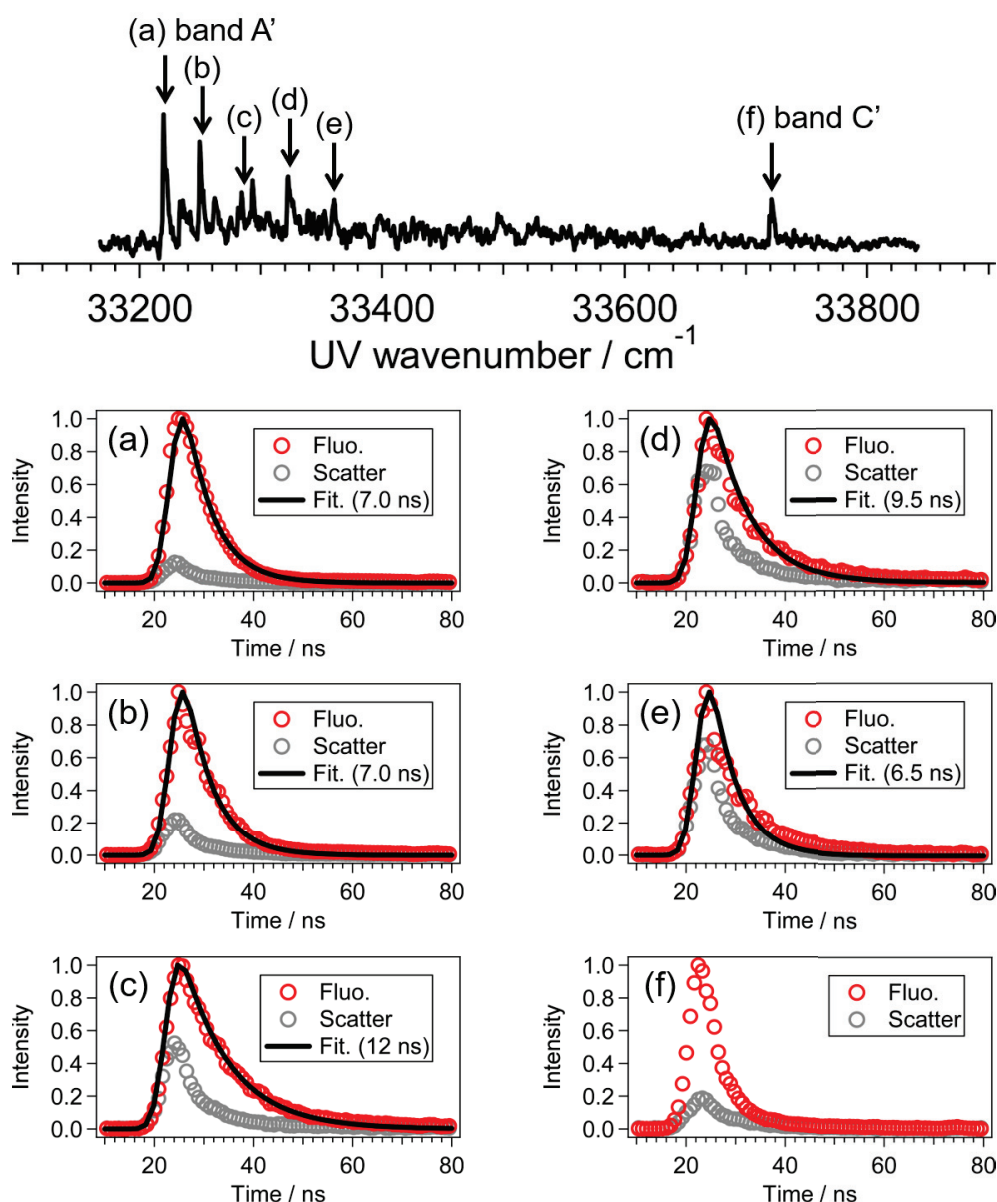


Figure 4 (Upper) LIF excitation spectrum of je-cooled MC-MeOH. Fluorescence decay curves of (a) band A' (0-0), (b) band A' + 30 cm^{-1} , (c) band A' + 64 cm^{-1} , (d) band A' + 103 cm^{-1} , (e) band A' + 141 cm^{-1} and (f) band C'(0-0). The red and gray plots represent the signal due to fluorescent and scatter of UV light, respectively. The black curves correspond to deconvoluted curve with laser pulse width (5 ns).

Next, the NRD process from the $^1\pi\pi^*$ state was investigated. Figure 5 (a) shows the time profile of the 0-0 band for the $^1\pi\pi^*$ state (band C') obtained by ps pump-probe measurement. Here, the ν_1 and ν_2 was fixed to 33720 cm^{-1} (band C') and 41140 cm^{-1} (243.1 nm), respectively. The deconvolution of the decay profile fitted by a single exponential decay gives a lifetime of $\tau = 180\text{ ps}$, which is 40 times longer than that of the bare one (4.5 ps),² indicating that the H-bonding to the C=O group suppresses the $^1\pi\pi^* \rightarrow ^1n\pi^*$ internal conversion (IC). This $^1\pi\pi^*$ lifetime elongation is the reason why band C' appears in the Figure 1 (b).

The NRD process was further investigated. Figure 4 (b) shows the time profile of band C' obtained by ns UV-DUV pump-probe measurement. Here, the ν_1 and ν_2 was fixed to 33720 cm^{-1} (band C') and 49260 cm^{-1} (203 nm), respectively. It is found that different from the bare MC, the component of long-lived state assigned to the T_1 ($^3\pi\pi^*$) is not/less detected in MC-MeOH. This phenomenon is similar to those of micro solvated *para*-hydroxy MC (*p*-HMC), *p*-MMC and 2-ethylhexyl 4-mthoxycinnamate.^{3,4} It was reported that the H-bonding of H₂O to the C=O group in these cinnamates suppresses the generation of the long-lived transient state.

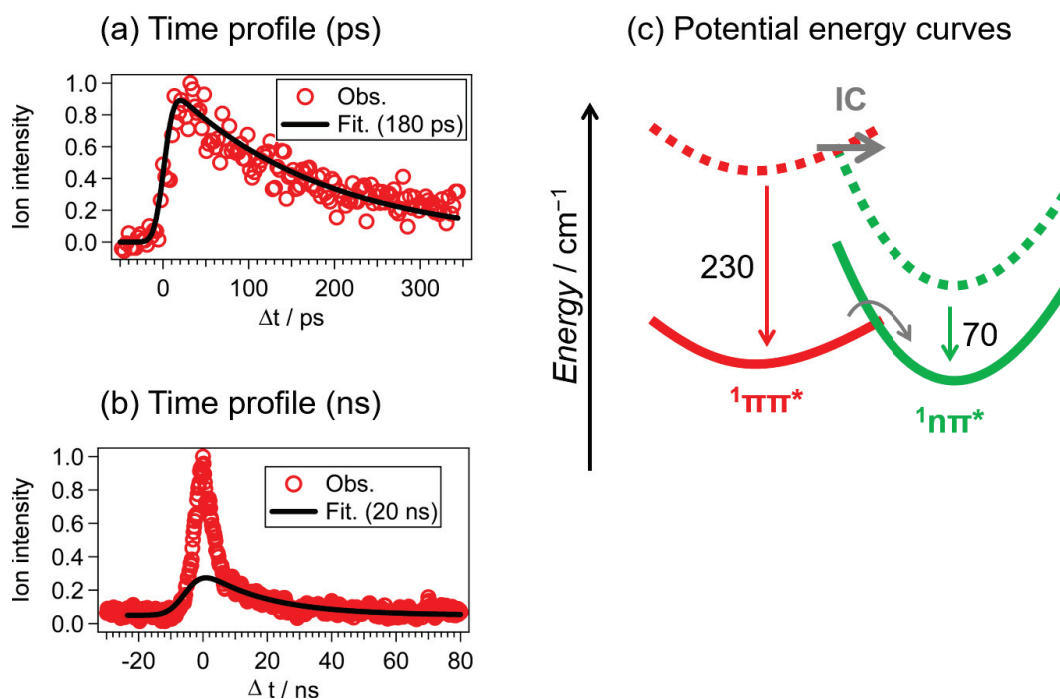


Figure 5 Time profile obtained by (a) ps UV-UV' and (b) ns UV-DUV pump-probe measurement. The black curves is convoluted curve with laser pulse width of (a) 12 ps and of (b) 5 ns, respectively. (c) Schematic potential energy curves of the $^1n\pi^*$ (green) and $^1\pi\pi^*$ (red) states in unit of cm^{-1} .

The suppression of the IC and generation of the T_1 ($^3\pi\pi^*$) can be explained by two reasons as follow. One is that the stabilization of the $^1\pi\pi^*$ energy by the H-bonding (230 cm^{-1}) is larger than that of the $^1n\pi^*$ (70 cm^{-1}). Thus, the barrier height of the $^1\pi\pi^* \rightarrow ^1n\pi^*$ IC becomes higher than that of the bare, as shown schematically in Figure 5 (c). Another is that the elongation of the $C_2=C_3$ (see Figure 2 in Chapter 3) bond length by the H-bonding. In ref. 4, it was mentioned that in case of micro solvated *p*-HMC with a H_2O (*p*-HMC- H_2O), the $C_2=C_3$ bond length in the optimized structure of the $^1\pi\pi^*$ state is increased by the H-bonding of H_2O to the C=O group in *p*-HMC, suggesting that the $C_2=C_3$ bond becomes easy to twist on the potential energy surface of the $^1\pi\pi^*$ state. Therefore, the C=C twisting process will be energetically favorable in MC-MeOH.

5-3 Absorption and fluorescence spectra

The finding of the above gas-phase experiment suggests that the fluorescence of MC in methanol solution will be stronger than that in nonpolar solvent. Therefore, in this section, the absorption and fluorescence spectra for MC, *p*-HMC and *p*-MMC were measured in methanol or cyclohexane.

Figure 6 (a) and (b) shows the absorption spectra of MC and *p*-MMC in cyclohexane and methanol at room temperature, respectively. The absorption spectrum of *p*-HMC in cyclohexane could not be obtained due to the low solubility under experimental conditions with a concentration of 10^{-4} M. The absorption in the 250–350 nm region is attributed to the S_0 - $^1\pi\pi^*$ transition. As can be seen in the spectra, the absorption intensity is almost the same for the three molecules, irrespective of the solvent. Figure 6 (c) shows the fluorescence spectra of MC and *p*-MMC. As can be seen in the spectra, the fluorescence intensity of MC in cyclohexane solution is four times weaker than that of *p*-MMC. This situation differs in methanol. The fluorescence intensity of MC in Figure 6 (d) is half that of *p*-MMC or *p*-HMC. That is, the fluorescence intensity of MC in methanol solution is two times stronger than that in cyclohexane. However, such a solvent dependence is not seen in *p*-MMC. The weakness of the fluorescence of MC in cyclohexane is due to the fact that cyclohexane is a non-polar solvent, thus the $^1n\pi^*$ state is thought to be lower than that of the $^1\pi\pi^*$ state. In this case, MC excited to the optically bright $^1\pi\pi^*$ state will relax immediately to $^1n\pi^*$ by IC and become less-fluorescent. On the other hand, the gas-phase experiment revealed

that the H-bonding of methanol to the C=O group of MC suppresses the ${}^1\pi\pi^* \rightarrow {}^1\pi\pi^*$ IC. Thus, the ${}^1\pi\pi^*$ state of MC becomes more fluorescent in methanol. Such a solvent effect does not occur in *p*-MMC or *p*-HMC. This is because the adiabatic energy of the ${}^1\pi\pi^*$ state is lower than the ${}^1n\pi^*$ state in these molecules, as can be seen in the Table 1 in Chapter 3 or the Table 4 in Chapter 4, and the H-bonding does not change this order. Thus, the situation of IC in *p*-MMC and *p*-HMC may be similar in the two solutions.

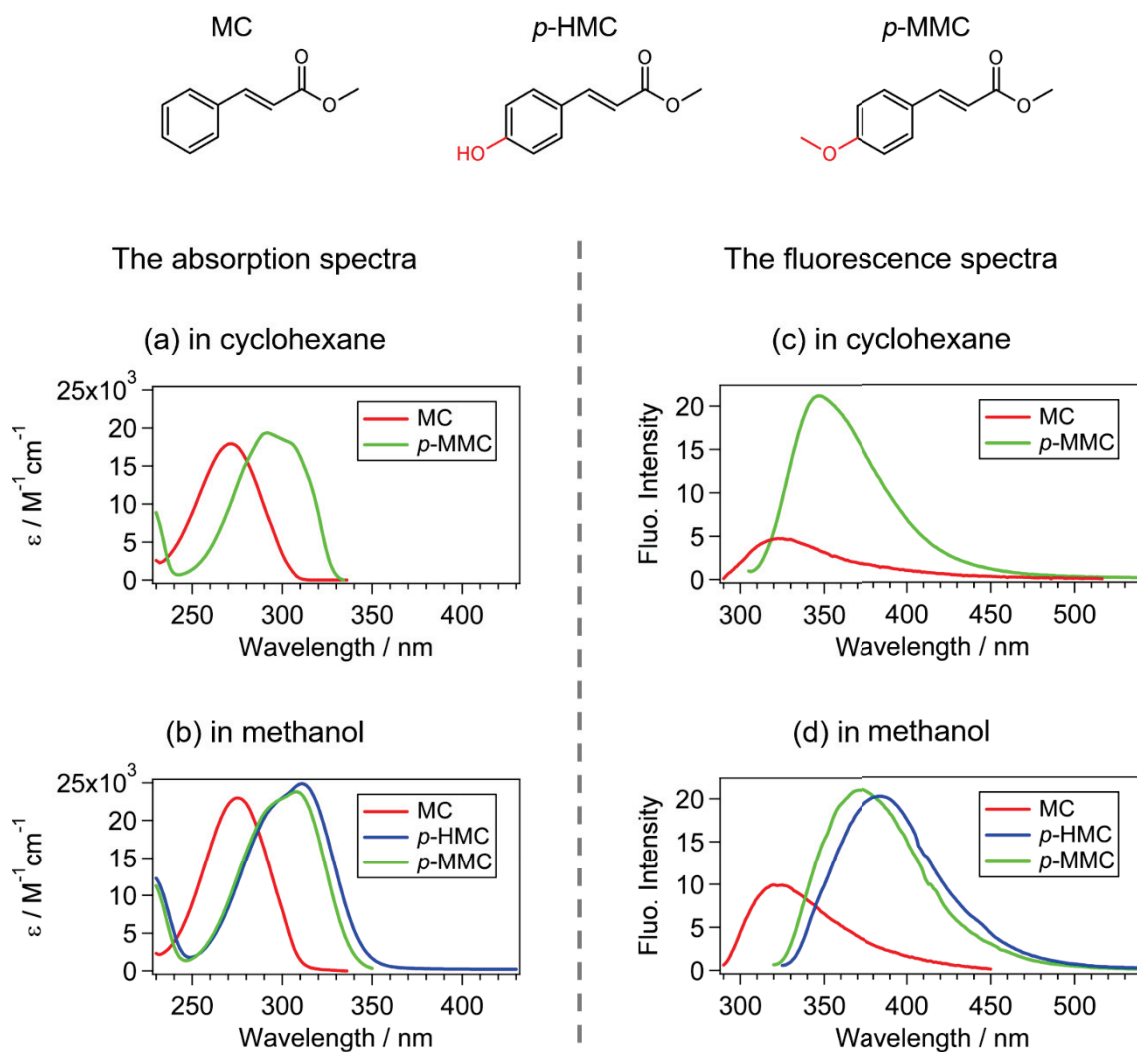


Figure 6 Absorption spectra of (a) MC and *p*-MMC in cyclohexane, (b) MC, *p*-HMC and *p*-MMC in methanol at room temperature. Fluorescence spectra of (c) MC and *p*-MMC, (d) MC, *p*-HMC and *p*-MMC measured by exciting their absorption maxima. The concentration is 10^{-4} M for all the measurements.

5-4 Conclusion

The H-bonding effect on the electronic states and the NRD process of MC was investigated by various spectroscopic techniques in the jet-cooled gas-phase and in solution.

The 0-0 band of the ${}^1n\pi^*$ and ${}^1\pi\pi^*$ state of jet-cooled MC-MeOH were observed in the electronic spectra. The value of red-shift for the ${}^1\pi\pi^*$ state is three times larger than that of the ${}^1n\pi^*$ state. The results of pump-probe measurements show that the H-bonding to the C=O group elongates the ${}^1\pi\pi^*$ lifetime, indicating that the H-bonding suppresses the ${}^1\pi\pi^* \rightarrow {}^1n\pi^*$ IC and generation of the transient T_1 (${}^3\pi\pi^*$). This lifetime elongation in MC-MeOH also describes well a higher fluorescence quantum yield of MC in methanol than in cyclohexane, while such a solvent dependence is not observed in *para*-substituted MCs.

References

1. Y. Miyazaki, K. Yamamoto, J. Aoki, T. Ikeda, Y. Inokuchi, M. Ehara and T. Ebata, *J. Chem. Phys.*, 2014, **141**, 244313.
2. K. M. Krokidi, M. A. P. Turner, P. A. J. Pearcy and V. G. Stavros, *Mol. Phys.*, 2020, DOI: 10.1080/00268976.2020.1811910.
3. E. M. M. Tan, M. Hilbers and W. J. Buma, *J. Phys. Chem. Lett.*, 2014, **5**, 2464-2468.
4. E. M. M. Tan, S. Amirjalayer, B. H. Bakker and W. J. Buma, *Faraday Discuss.*, 2013, **163**, 321-340.

Chapter 6

Conclusion of this thesis

In this thesis, the substitution and hydrogen (H)-bonding effects on the electronic states and the nonradiative decay (NRD) route involving *trans* (*E*) \rightarrow *cis* (*Z*) photoisomerization of methylcinnamate (MC) were investigated by supersonic jet/laser spectroscopy and quantum chemical calculation. Finally, this thesis aims to provide a molecular design for a development of cinnamate-based sunscreen.

In Chapter 3, the photoisomerization of non-substituted cinnamate, MC, was investigated. In the electronic spectra of jet-cooled MC, the optically “dark” $^1n\pi^*$ state was observed in the energy region lower than the optically “bright” $^1\pi\pi^*$ state. Upon photoexcitation to the $^1\pi\pi^*$ state, *trans*-MC rapidly decays to the $^1n\pi^*$ state *via* internal conversion (IC). After the IC, MC decays to the T_1 ($^3\pi\pi^*$) *via* consecutive intersystem crossing and ICs. Finally, MC either returns to *trans*-isomer or isomerizes to *cis*-isomer in the ground state (S_0). Therefore, it is concluded that the dominant photoisomerization route of MC is described as “ $^1\pi\pi^*$ (*trans*) \rightarrow $^1n\pi^*$ \rightarrow T_1 ($^3\pi\pi^*$) \rightarrow S_0 (*trans* or *cis*)”.

In Chapter 4, the substitution and its position effect on the photoisomerization of MC was investigated. The substitution at *para* position slightly lowers the energy of the $^1\pi\pi^*$ state, therefore order of the $^1\pi\pi^*$ and $^1n\pi^*$ states is reversed between MC and *para*-substituted MCs. This energy inversion

increases the contribution of another sub ns NRD route involving the T_1 state that is described as “ ${}^1\pi\pi^*$ (*trans*) \rightarrow ${}^3n\pi^*$ \rightarrow ${}^3\pi\pi^*$ \rightarrow S_0 (*trans* or *cis*)”. On the other hand, the substitution at *meta* or *ortho* position drastically lowers the energy of the ${}^1\pi\pi^*$ state and increases the energy barrier of ${}^1\pi\pi^* \rightarrow {}^1n\pi^*$ IC. Thus, the direct isomerization process, twisting of the C=C bond on the ${}^1\pi\pi^*$ potential energy surface (PES), is thought to be the dominant photoisomerization route, described as “ ${}^1\pi\pi^*$ (*trans*) \rightarrow C=C bond twisting on the ${}^1\pi\pi^*$ PES \rightarrow S_0 (*trans* or *cis*)”. The electronic state and NRD/photoisomerization of cinnamates are affected by the substitution at its phenyl ring. *para*-substituted cinnamates can be the most effective sunscreen reagents because the multistep NRD process can rapidly convert harmful absorbed UV energy to safer thermal energy.

In Chapter 5, the H-bonding effect on the NRD process of MC was investigated. The H-bonding of a methanol molecule to the C=O group in MC suppresses the ${}^1\pi\pi^* \rightarrow {}^1n\pi^*$ IC and generation of the T_1 (${}^3\pi\pi^*$). This result consists with that in solution, that the fluorescence intensity of MC in methanol is two times larger than that in cyclohexane.

Finally, the newly developed nanosecond UV-tunable DUV pump-probe spectroscopy is versatile, therefore this spectroscopy can be applied to other systems. Thus, I strongly believe that this new spectroscopy reveals the NRD process of other sunscreen reagents shown in Chapter 1 and helps us to design more effective chemical filter in the future.

公表論文

(1) Substitution effect on the nonradiative decay and *trans* → *cis* photoisomerization route: a guideline to develop efficient cinnamate based sunscreens

Shin-nosuke Kinoshita, Yu Harabuchi, Yoshiya Inokuchi, Satoshi Maeda, Masahiro Ehara, Kaoru Yamazaki and Takayuki Ebata

Phys. Chem. Chem. Phys., 2021, **23**, 834-845.

Front cover picture, 2021 PCCP HOT Articles

(2) The direct observation of the doorway $^1n\pi^*$ state of methylcinnamate and hydrogen-bonding effects on the photochemistry of cinnamate-based sunscreens

Shin-nosuke Kinoshita, Yoshiya Inokuchi, Yuuki Onitsuka, Hiroshi Kohguchi, Nobuyuki Akai, Takafumi Shiraogawa, Masahiro Ehara, Kaoru Yamazaki, Yu Harabuchi, Satoshi Maeda and Takayuki Ebata

Phys. Chem. Chem. Phys., 2019, **21**, 19755-19763.

Back cover picture, 2019 PCCP HOT Articles

(3) Different photoisomerization routes found in the structural isomers of hydroxy methylcinnamate

Shin-nosuke Kinoshita, Yasunori Miyazaki, Masataka Sumida, Yuuki Onitsuka, Hiroshi Kohguchi, Yoshiya Inokuchi, Nobuyuki Akai, Takafumi Shiraogawa, Masahiro Ehara, Kaoru Yamazaki, Yu Harabuchi, Satoshi Maeda, Tetsuya Taketsugu and Takayuki Ebata

Phys. Chem. Chem. Phys., 2018, **20**, 17583-17598.

Back cover picture

参考論文

(1) Electronic States and Nonradiative Decay of Cold Gas-Phase Cinnamic Acid Derivatives Studied by Laser Spectroscopy with Laser Ablation Technique

Yuji Iida, Shin-nosuke Kinoshita, Seiya Kenjo, Satoru Muramatsu, Yoshiya Inokuchi, Chaoyuan Zhu, and Takayuki Ebata

J. Phys. Chem. A **2020**, *124*, 5580-5589.

(2) Electronic State and Photophysics of 2-Ethylhexyl-4-methoxy cinnamate as UV-B Sunscreen under Jet-Cooled Condition

Satoru Muramatsu, Shingo Nakayama, Shin-nosuke Kinoshita, Yuuki Onitsuka, Hiroshi Kohguchi, Yoshiya Inokuchi, Chaoyuan Zhu, and Takayuki Ebata

J. Phys. Chem. A **2020**, *124*, 1272-1278.

(3) Laser spectroscopic study on sinapic acid and its hydrated complex in a cold gas phase molecular beam

Seiya Kenjo, Yuji Iida, Nobumasa Chaki, Shin-nosuke Kinoshita, Yoshiya Inokuchi, Kaoru Yamazaki, Takayuki Ebata

Chemical Physics **515** (2018) 381-386.

(4) Multistep Intersystem Crossing Pathways in Cinnamate-Based UV-B Sunscreens

Kaoru Yamazaki, Yasunori Miyazaki, Yu Harabuchi, Tetsuya Taketsugu, Satoshi Maeda, Yoshiya Inokuchi, Shin-nosuke Kinoshita, Masataka Sumida, Yuuki Onitsuka, Hiroshi Kohguchi, Masahiro Ehara, and Takayuki Ebata

J. Phys. Chem. Lett. **2016**, *7*, 4001-4007.

